First International Conference on Geotechnique, Construction Materials and Environment, Mie, Japan, Nov.21-23, 2011, ISBN: 978-4-9905958-0-7 C3051

Geotechnical Investigation of Valleys using Lightweight Dynamic Cone Penetration Test for Landslide Risk Assessment

Takashi Hanaoka, Takashi Tsuchida, Shouichi Kawabata, Shouta Nakagawa, Hiroshima University

ABSTRACT: Counter-measures by using the regulations, information technology and the education to the residents are important because it take a tremendous time and cost for implementing physical disaster prevention measures to all potentially dangerous areas. The purpose of this study is to develop the site-investigation of natural valley using lightweight cone penetration test (LWDCPT), in order to implement the risk assessment of individual valleys with the slope stability analysis based on the models of valley obtained by the investigation. A series of investigation was carried out at four valleys in Higashi-Hiroshima city, which are put on the list of valleys potentially dangerous for mud and debris flows during heavy rain. LWDCPT was performed at both sides of valley with each descending to 20 meters with reference to head of valley until gradient of valleys become below 12.5 degrees, in which the necessary time for the site-investigation by two persons was about eight hours per one valley.

Keywords: Geotechnical investigation, Lightweight cone penetration test, Individual natural valley, Ground model

1. INTRODUCTION

In Hiroshima Prefecture, 31,987 valleys and slopes are listed as areas of dangerous for slope failure and debris flow, and this is the largest number in Japan. Counter-measures by using the regulations, information technology and the education to the residents are important because it take a tremendous time and cost for implementing physical disaster prevention measures to all potentially dangerous areas. In Hiroshima Prefecture, the prefectural land is divided into 350 unit areas of 5 kilometers square, and in each unit area, the criteria using the rainfall indexes, such as the soil water index and rainfall intensity, are determined on the basis of past records of landslide disasters due to heavy rain. In this system, a warning for an expected landslide or an evacuation order is made for each unit area, however, the risk of individual slopes in each area cannot be shown.

To assess the safety of an individual valley or slope, the geotechnical slope stability analysis is necessary. However, one major problem in natural slopes is that there has been little information on geotechnical conditions because of the extreme difficulty associated with ground investigation on the steep slopes covered with vegetation. The purpose of this study is to develop the site-investigation method of natural valley using lightweight cone penetration test (LWDCPT), in order to implement the risk assessment of individual valleys with the slope stability analysis based on the models of valley obtained by the investigation.

We focused on the large number of potentially dangerous valleys in Higashi-Hiroshima City, and selected four valleys in as same unit. The areas painted in yellow in Fig. 1 show the potentially dangerous valleys in Saijo Town of Higashi Hiroshima City. Fig. 2 shows the selected four valleys, which is in the red circle in Fig. 1, which are included in one 5km×5km regional mesh for the present risk assessment. Accordingly, the risks in these four valleys are same in the present method, and the purpose of this study is to evaluate the risks of the four valleys individually.

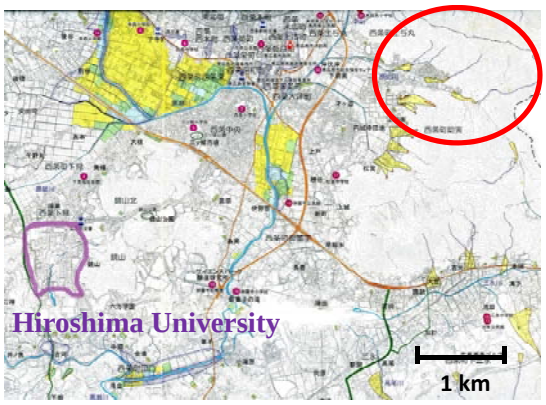

Fig. 1. Valleys at risk of landslide of in the town of Saijo.

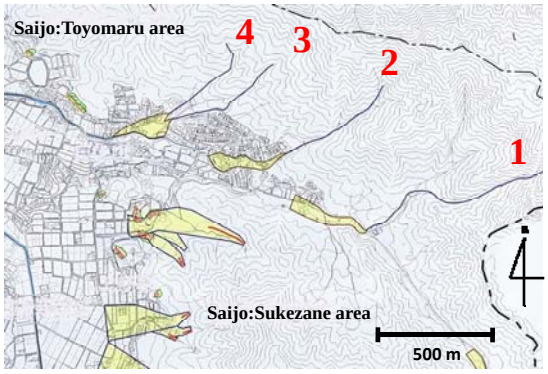

Fig. 2. Valleys where the survey were carried out.

2. GEOTECHNICAL INVESTIGATION

Geotechnical investigation was carried out in order to model the valleys for the seepage analysis and the slope stability analysis. The necessary items of modeling are slope gradient, thickness of surface soil and strength parameters. We explain how to determine of these items.

2.1 Light weight cone penetration test

LWDCPT has been designed and developed in France since 1991 (Langton, D.D., 1999). The schematic view of LWDCPT is shown in Figure 3. The mass is about 20 kg, and mainly consists of an anvil with a strain gauge bridge, central acquisition unit (CAU), and a dialogue terminal (DT). The below from the hammer to the anvil provides energy input, and a unique microprocessor records the speed of the hammer and the depth of penetration. The dynamic cone resistance (q_d) is calculated from the modified form of Dutch Formula as shown in Equation (1) (Cassan, M., 1988).

$$q_d = \frac{1}{A}\frac{\frac{1}{2}MV^2}{1+\frac{P}{M}}\frac{1}{x_{90^\circ}} \qquad (1)$$

Where, x_{90° = penetration due to one below of hammer by 90° cone,
A = area of the cone,
M = the mass of striking hammer,
P = the mass of the struck materials, and
V = speed of the impact of the hammer.

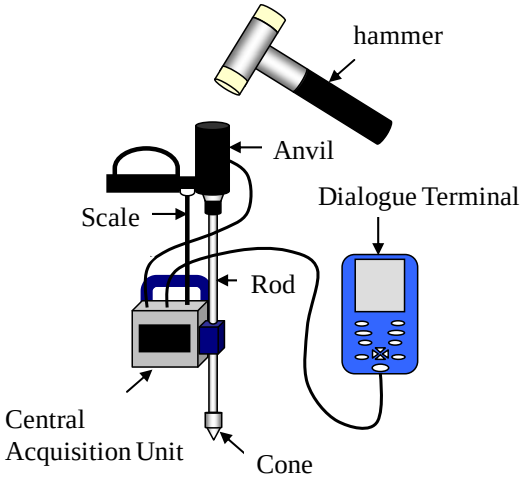

Figure 3. Outline of LWDCPT.

Photo 1. Appearance of LWDCPT (Valley 1).

Photo 1 shows appearance of LWDCPT. The advantages of LWDCPT are that the detail measurements are possible by getting a penetration resistance value with each hitting, and that in virtue of the lightweight and the simple, even for the non-specialist of geotechnical investigation, the operation is easy and safe.

2.2 Selection of the testing points in a valley

A geotechnical investigation of the valleys was carried out under the following policies.

(1)The headwater area was determined by using topographical data and a field trip. About six geotechnical investigation points were selected in the headwater area, and along the valley the geotechnical testing points were selected at intervals of 20 meters, downward.

(2) A test of the valley was carried out at both sides of the valley, which are 5 located meters away from the center of valley. The tests were carried out the headwater down to the valley, the gradient of which is larger than 12.5 degree.

(3) The sampling was carried out at both sides of four

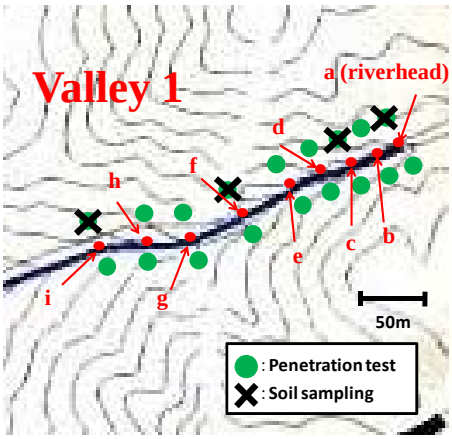

Fig.4. A example of selection of geotechnical investigation points (Valley 1).

Table 1. Number of geotechnical investigation points.

	Valley 1	Valley 2	Valley 3	Valley 4
Number of LWCPT	9	4	7	7
Number of soil sampling	4	4	4	4

Photo 2. Site of the geotechnical investigation. (Valley 4)

investigation points in each valley.

Fig. 4 shows a example of selected of testing points (Valley 1). Table 1 shows the number of geotechnical investigation points of the four valleys. Photo 2 shows the site of the geotechnical investigation in Valley 1. The testing points were nine and the soil sampling points were four in Valley 1.

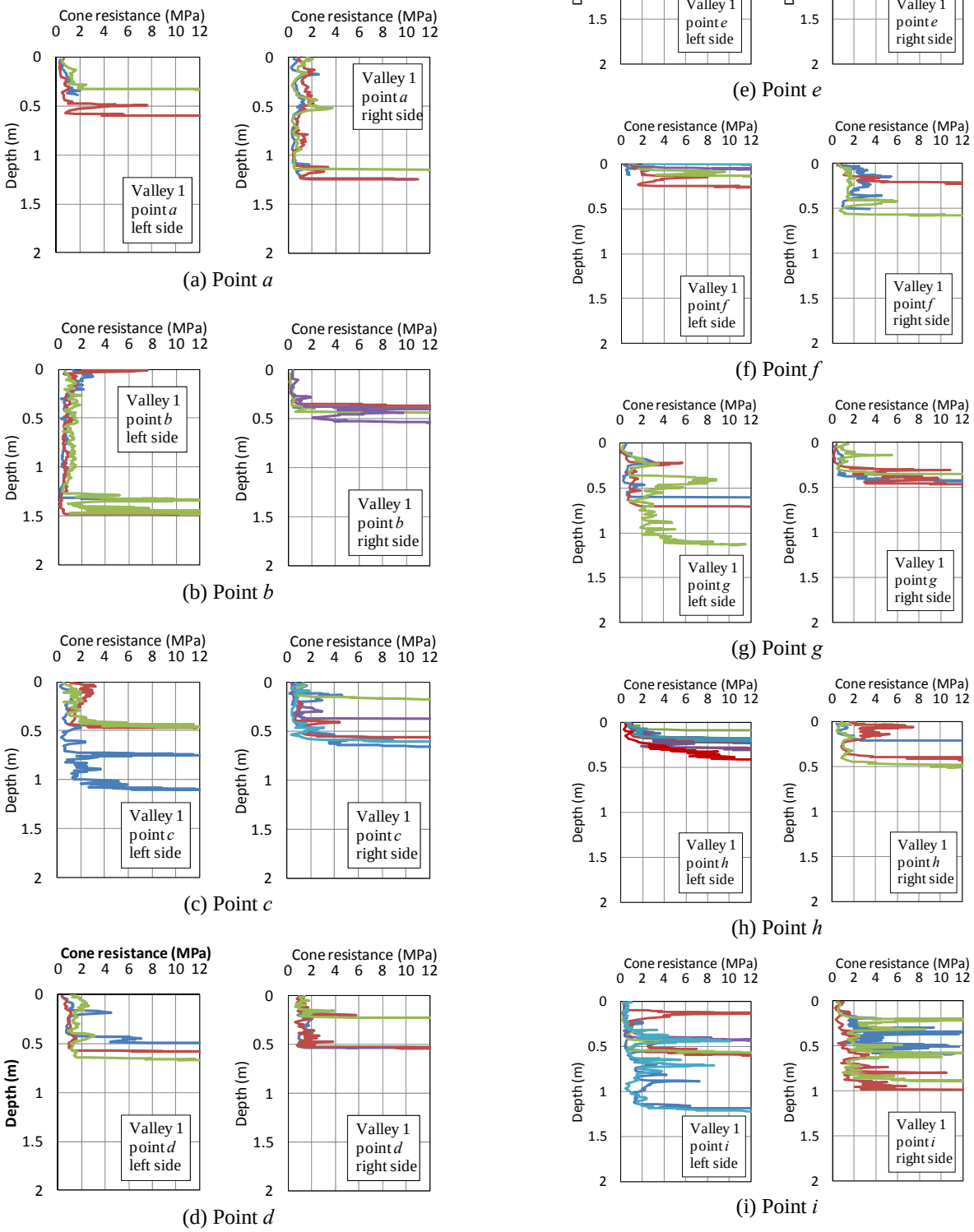

Fig. 5. Penetration resistance q_d with depth

Table 2. Thicknesses of surface soil each point (Valley 1)

	left side		right side		average	
a	0.60	m	1.24	m	0.92	m
b	1.48	m	0.53	m	1.01	m
c	1.10	m	0.65	m	0.88	m
d	0.66	m	0.53	m	0.60	m
e	0.97	m	0.65	m	0.81	m
f	0.26	m	0.58	m	0.42	m
g	1.13	m	0.46	m	0.80	m
h	0.42	m	0.48	m	0.45	m
i	1.22	m	0.99	m	1.11	m

2.3 Investigation of thickness of surface soil

LWDCPT was continued until over 10 MPa value through three hitting in a row. Because, the relationship between the penetration resistance q_d of LWDCPT and N_d value of the portable dynamic cone penetration test (PDCPT) was proposed by Tsuchida et al. (2011), as shown in Equation (2).

$$q_d = \frac{1}{4} N_d \tag{2}$$

That is, over 10 MPa of q_d is considered to be equal to over 40 of N_d value, which can be estimated as the basement rock.Fig.5 shows penetration resistance q_d with depth in Valley 1. The thickness of surface soil of each point in Valley 1 was estimated as the average value both sides. Table 2 shows thicknesses of surface soil each point in Valley 1.

2.4 Estimation of strength parameters

Using these results, the cohesion and the internal friction angle of the ground were estimated using the equations suggested by Tsuchida et al. (2011). In these equations, the degree of saturation S_r and the penetration resistance of LWDCPT q_d are necessary. In order to obtain degree of saturation S_r, the tube sampling was carried out at the point in Fig. 4 (Valley 1). The appearance of tube sampling is shown in Photo 3. The corrected penetration q_{d5} was calculated by using Equation (3), where q_{d5} is the penetration resistance under 5kPa effective overburden stress and the correction from q_d to q_{d5} are made as follows:

$$q_{d5} = q_d - 0.01 \times (\gamma_t \cdot z - 5) \tag{3}$$

Photo 3. Tube sampling

where, q_d = penetration resistance (MPa), γ_t = unit weight (kN/m^3), and z = depth(m).

The cohesion and internal friction angle of the ground were calculated by Equation (4) and (5), which were proposed by Tsuchida et al. (2011),

$$\phi_d = 29.9 + 1.61 \cdot \ln(q_{d5}) - 0.142 S_r \tag{4}$$

$$c_d = 10.6 + 1.19 \cdot \ln(q_{d5}) - 0.041 S_r \tag{5}$$

where, c_d = apparent cohesion of drained condition(kN/m^2), ϕ_d = apparent internal friction angle of drained condition (degree), and S_r = degree of saturation (%).

Table 3 shows the estimation of strength parameters in Valley 1.

3 MODELING OF VALLEYS BY INVESTIGATION

Fig. 6 shows modeling of four valleys by geotechnical investigation. The average values of the thickness of Valley 1, Valley 2, Valley 3 and Valley 4 were 0.79 m, 0.70 m, 0.57 m, and 1.31 m, respectively. The average values of the slope gradients of Valley 1, Valley 2, Valley 3, and Valley 4 were 14.4 degree, 16.3 degree, 16.1 degree, and 18.1 degree, respectively. In the present risk assessment method, these four valleys were included in a mesh for the assessment. By carrying out geotechnical investigation shown in this study, it is possible to model the valley and assess the risk by the

Table 3. Estimation of strength parameters (Valley 1).

	a	b	c	d	e	f	g	h	i
wet density ρ_t (g/cm^3)	1.35								
degree of saturation S_r (%)	33.61								
wet unit weight γ_t (kN/m^3)	13.21								
q_{d5} (MPa)	1.18	0.54	0.96	1.33	0.73	1.68	0.86	1.16	0.67
e	0.93	0.99	0.94	0.92	0.97	0.90	0.95	0.93	0.97
ϕ_d (degree)	34.9	33.7	34.6	35.1	34.2	35.5	34.4	34.9	34.0
c_d (kN/m^2)	9.4	8.5	9.2	9.6	8.8	9.8	9.0	9.4	8.7

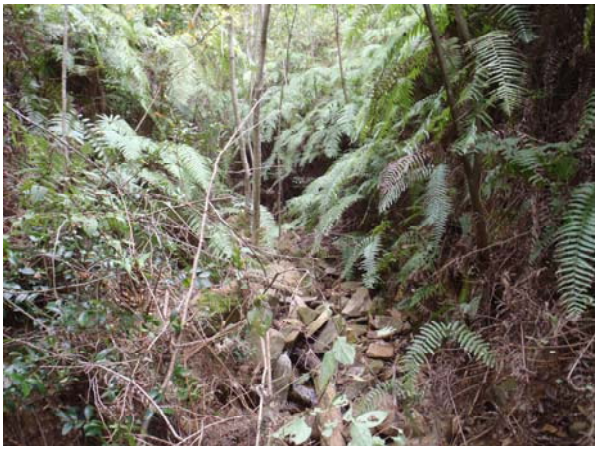

Photo 4. The steep slope.

Photo 5. The gravel under the ground.

stability analysis individually.

As already discussed, in Hiroshima Prefecture, 31,987 valleys and slopes are listed as areas of dangerous for slope failure and debris flow. Therefore, it is difficult to investigate all dangerous areas in a short period with the limited budget of local government. It is preferable in order to become a practical method that the investigation method is as simple and inexpensive as possible. As one way, it is considered that to request volunteers, who are not experts but members of autonomy disaster prevention organization in the area, to investigate the valleys. Thus, the investigation method which everyone can do and personal error not observed is preferable.

4 CONSIDERATION

The purpose of this study is to develop the procedure of site investigation of natural valley using lightweight cone penetration test (LWDCPT), in order to implement the risk assessment of individual valleys. From the investigations of four valleys, the following points were found;

1) The operation of investigation in this study is very easy, and it seems that even a non-experts can carry out the investigation based on a manual of this method. However, some investigation points, LWDCPT cannot work well, because of many tree roots or gravels under the ground and the much steepness of slope. In these cases, non-expert may not cope. And if the penetration resistance appears large value, sometimes, it is difficult to judge whether there is a gravel of a large diameter at this point, or it reaches bedrock as shown in Photo 5.
2) In this investigation, two LWDCPT were used by two persons (one person use one machine), and other two persons took undisturbed and disturbed samples at the site. It took eight hours to investigate all investigation points in Valley 1 which has largest investigation points (9 points) in the four valleys. Therefore, it is possible to investigate each valley in a day. However, in case of investigate points are over 10 points, it may be necessary to increase investigator or to take two days.

5 CONCLUSIONS

The geotechnical investigation using the LWDCPT was carried out in order to model natural valley or slope for the stability analysis. The advantages of LWDCPT are that the detail measurements are possible by getting a penetration resistance value with each hitting, and that in virtue of the lightweight and the simple, even for the non-specialist of geotechnical investigation, the operation is easy and safe. Thickness of surface soil and strength parameters were able to be estimated. Four valleys, which are same risk assessment in present method, were able to be modeled individually. It took eight hours to investigate all testing points in Valley 1 which has largest number testing points (9 points) in the four valleys. In case of investigate points under this, it is possible to investigate a valley in a day. However, in case that testing points over more than 10 points, it is necessary to increase investigator in order to improve efficiency or divide two days.

6 REFERENCES

[1] Higashi Hiroshima City: http://www.city.higashihiroshima.hiroshima.jp/site/bousai/hazard.html

[2] Hiroshima Prefecture, http://www.pref.hiroshima.lg.jp/page/1171592994610/index.html

[3] Langton, D.D., "The PANDA-lightweight penetrometer for soil investigation and monitoring material compaction," Ground Engineering, September 1999, pp. 33-37.

[4] Cassan, M., "Les essays in situ en mechanique des sols, realization et interpretation," Eyrolles, Paris, 2nd ed. Vol. 1, pp. 146-151.

[5] Tsuchida T, Athapaththu A.M.R.G., Kano S, Suga K, "Estimation of in-situ shear strength parameters of weathered granitic (Masado) slopes using lightweight dynamic cone penetrometer," Soils and Foundations, vol. 51, No. 3. (to be published), 2011.

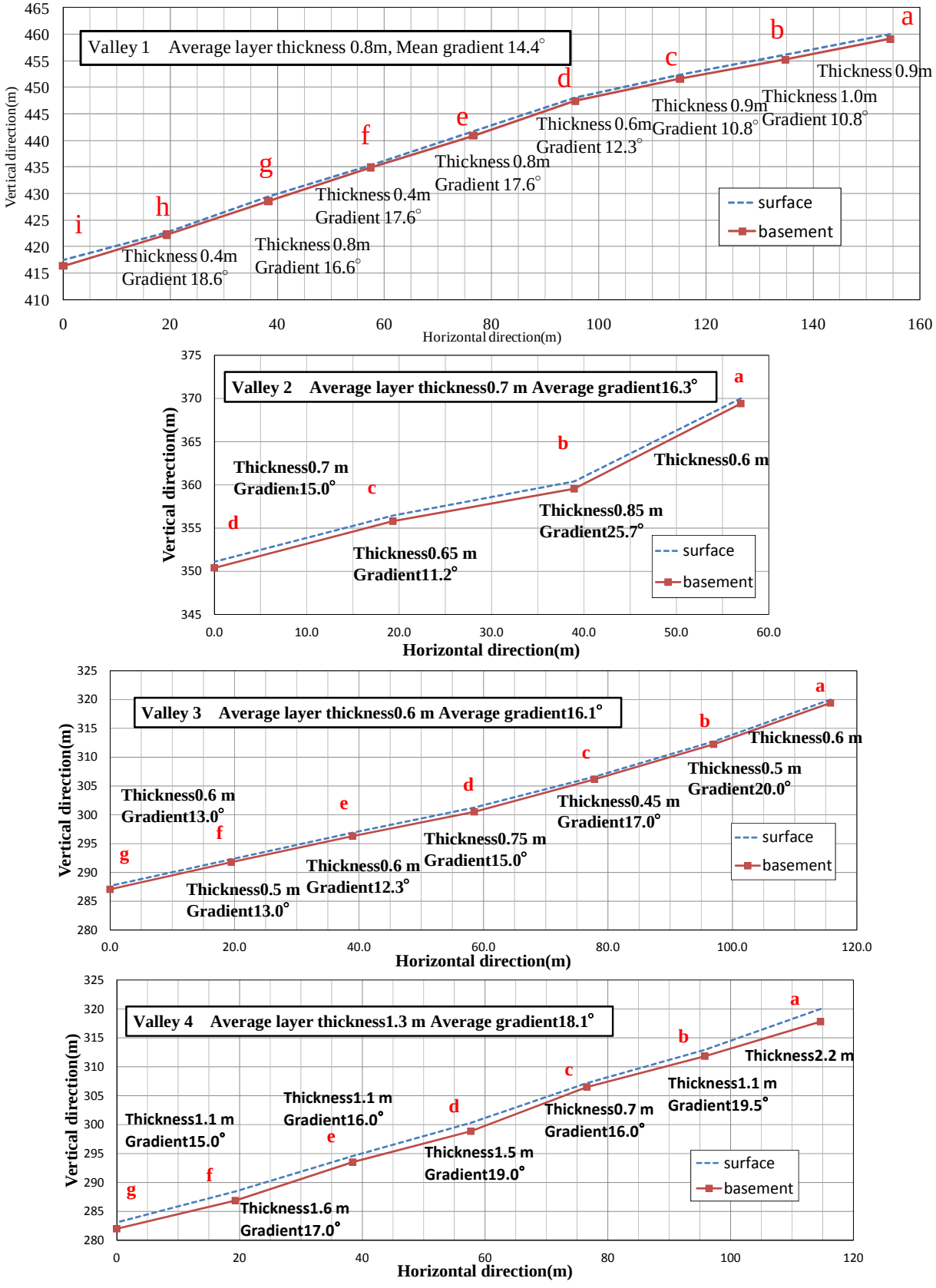

Fig. 6. Model cross-section of 4 valleys in Higashi-Hiroshima City.

First International Conference on Geotechnique, Construction Materials and Environment, Mie, Japan, Nov.21-23, 2011, ISBN: 978-4-9905958-0-7 C3051

Study on Individual Landslide Risk Assessment of Natural Valleys and Slopes during Heavy Rain Based on Geotechnical Investigation and Analysis

Shouichi Kawabata. Takashi Tsuchida. Takashi Hanaoka. Shouta Nakagawa., Hiroshima University

ABSTRACT: In Hiroshima Prefecture, the prefectural land is divided into 350 unit areas of 5 kilometers square, and in each unit area, the criteria using the rainfall indexes, such as the soil water index and rainfall intensity, are determined on the basis of past records of landslide disasters due to heavy rain. However, in this system, the risk of individual valleys or natural slopes in each area cannot be shown. In this study, a series of investigation was carried out at four valleys in Higashi-Hiroshima city, which are put on the list of valleys potentially dangerous for mud and debris flows during heavy rain. For the conditions continuous rain, the infiltration analysis during the rain, the ground water seepage analysis and the slope stability analysis were carried out based on the ground models obtained by the site investigation. The risk of slope failure for each of four valleys was given as the risk assessment point, and was compared and discussed.

Keywords: Risk Assessment, Landslide, Site Investigation, Ground Water

1. INTRODUCTION

Hiroshima Prefecture has 31,987 hazardous areas for landslide disasters, the largest number in Japan in [1]. In Hiroshima, a regional soil called Masado soil, a weathered granite, widely covers the surfaces of natural slopes. From a geotechnical point of view, the failures of natural slopes are mainly caused by rises in groundwater levels and the loss of inbound shear strength of Masado soil due to both continuous and intensive seasonal rains.

Fig. 1 shows present risk assessment method and purpose of this study. The present regional risk assessment method utilized by the Hiroshima Prefecture government is thoroughly based on the measured rainfall and the rainfall-failure relationship in each 5 km×5 km area obtained from the past records of the disasters. In this system, the risks of slope failure and evacuation orders are given for an area 5 km×5 km, and the risks to individual slops cannot be shown. Accordingly, it can be said that the present risk assessment method is an empirical one, and is not a theoretical or geotechnical one. In this study, Geotechnical investigations of four natural valleys in Higashi Hiroshima City were carried out using a lightweight dynamic cone penetration test and a soil sampling. In order to improve the present risk assessment method, landslide risk assessments of these valleys for some predicted rain conditions were made by using a seepage analysis, a ground water level analysis, and a slope stability analysis of each valley.

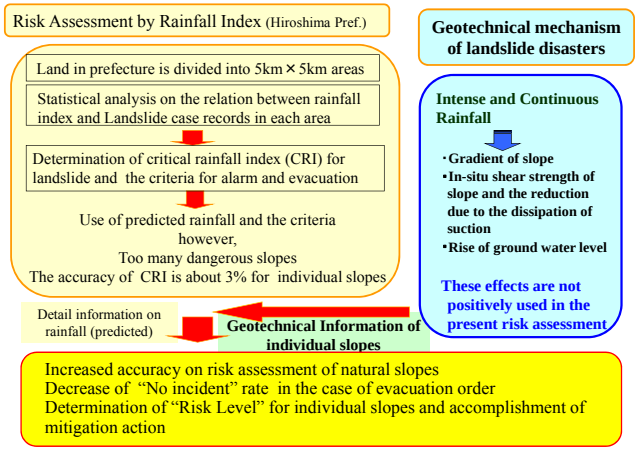

Fig. 1. Valleys at risk of landslide of in the town of Saijo.

2. SELECTION OF VALLEYS

In the selection of valleys for the study, we focused on the large number of potentially dangerous valleys in Higashi-Hiroshima City. Fig.2 shows the selected four valleys, which are included in one 5 km×5 km regional mesh for the present risk assessment based on the rainfall index. Accordingly, the risks in these four valleys are the same as in the traditional method, but the purpose of this study is to evaluate the risks to the four valleys individually.

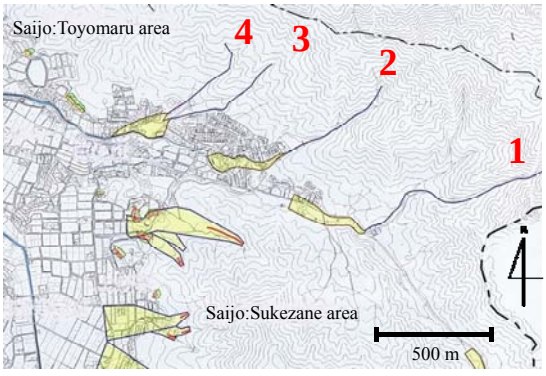

Fig. 2. Valleys where the survey were carried out in [2].

3. GEOTECHNICAL INVESTIGATION METHOD OF NATURAL VALLEYS

Table 1 shows geotechnical investigation points. A geotechnical investigation of the valleys was carried out under the following policies.

Table 1. Geotechnical investigation points.

	valley1	valley2	valley3	valley4
penetration test	9	4	7	7
soil sampling	4	4	4	4

(1) The headwater area was determined by using topographical data and a field trip. About six geotechnical investigation points were selected in the headwater area, and along the valley the geotechnical testing points were selected at intervals of 20 meters, downward.
(2) A test of the valley was carried out at both sides of the valley, which are 5 located meters away from the center of valley. The tests were carried out the headwater down to the valley, the gradient of which is larger than 12.5 degree.
(3) The sampling was carried out at both sides of four investigation points in each valley.

4. RESULTS OF THE GEOTECHNICAL INVESTIGATION

The thickness of the surface soil was estimated by analyzing the penetration resistance of each geotechnical investigation point. In Fig.3, the penetration resistance q_d of lightweight dynamic cone penetration test with depth, which was measured at point 9 in Valley 1, is shown in [3]. Slope models were made using the estimated thickness of the surface soil and the slope gradients. With these results, a model cross-section of each valley was made, as shown in Fig.4. The horizontal distance of the cross-section was determined by the geotechnical investigation point, and the thickness of the surface soil came out of the average from the estimated values of both sides, which were 5 meters away from the center of the valley. The average values of the thickness of Valley 1, Valley 2, Valley 3, and Valley 4 were 0.8 m, 0.7 m, 0.6 m, and 1.3 m, respectively. The average values of the slope gradients of Valley 1, Valley 2, Valley 3, and Valley 4 were 14.4 degree, 16.3 degree, 16.1 degree, and 18.1 degree, respectively. Furthermore, the void ratio, the density of soil particles, the degree of saturation, and the unit weight were obtained by the laboratory tests of soil samples taken in each valley.
Using these results, the cohesion and the internal friction angle of the ground were estimated using the equations suggested by Tsuchida *et al.* (2011).
With these results, cohesions were estimated to be between 8.2 kN/m^2 and 11.2 kN/m^2, and the internal friction angles were between 29.6 degree and 36.4 degree.

5. SEEPAGE ANALYSIS

Fig. 5 shows the model of the rainfall seepage in this study. When it rains continuously and the rainfall begins to infiltrate into the ground, the volumetric moisture content of the upper soil layer rises to a certain value θ_h from the surface layer. Afterwards, the unsaturated layer maintains the volumetric water content θ_h and descends toward the lower layer. This unsaturated layer is called the high moisture content belt (HMCB). The underground water level is formed in the soil layer when the HMCB reaches the impermeable layer, and the groundwater level starts to gradually rise from the impermeable layer upward, as shown in Fig. 5.
To figure out this process, a one-dimensional unsaturated seepage analysis was carried out at each point of the valleys. The primitive equation used for the unsaturated seepage analysis is that used in the expression of Richards in [6]. The expression of Richards is given by the following equation:

$$C(\psi)\frac{\partial \psi}{\partial t}+\frac{\partial}{\partial z}\left(-k(\psi)\frac{\partial(\psi+z)}{\partial z}\right)=0 \qquad (1)$$

where, ψ =pressure head(cmH_2O), $C(\psi)$= specific moisture capacity, $k(\psi)$= hydraulic conductivity (cm/s). The rainfall seepage boundary condition in the surface of the ground is

Photo 1. Site of the geotechnical investigation. (Valley 3)

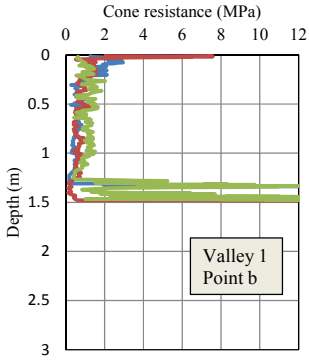

Fig. 3. Penetration resistance qd with depth (Valley 1).

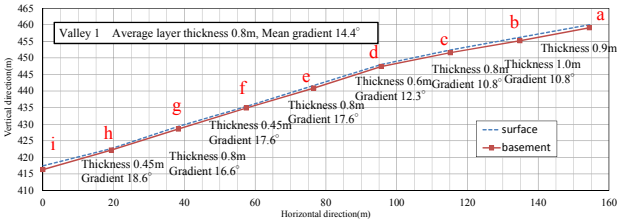

Fig. 4. Model cross-section of Valley 1 in Higashi-Hiroshima City.

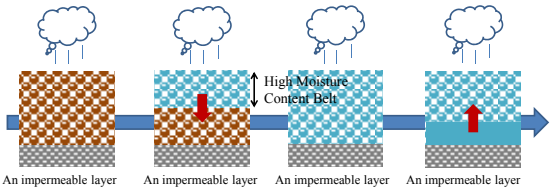

Fig. 5. Conceptual diagram of rainfall seepage.

given by the following equation:

$$R = q = K(\psi)\left(\frac{\partial \psi}{\partial z} + 1\right) \tag{2}$$

where, R= amount of rainfall, q= flow velocity in a surface. Suction was calculated by using the difference approximation expression of Richards' equations. The volumetric moisture content was calculated by applying the obtained suction value to the soil moisture characteristic curve, in which the initial pressure head and the total head are determined by the experiments on weathering granite (Masado) carried out by Yuri (2010); that is, the saturated volumetric moisture content was 0.433, the residual volumetric moisture content was 0.158, the saturated hydraulic conductivity was 0.006 cm/s and the initial volumetric moisture content was 0.300. Fig. 6 shows the soil moisture characteristic curve used in this study.

Fig. 7 shows an example of the one-dimensional seepage analysis at Point b in Valley 1 under a rain intensity of 5 mm/hour. As shown in Fig. 7, HMCB is formed from the surface, and goes downwards. After 14.1 hours, the HMCB reaches the bottom of the soil layer, and after the saturated layer is formed at the bottom after 21.15 hr, the groundwater level rises.

The volumetric moisture content in HMCB is closely related to the rainfall intensity, and the descending speed of HMCB is decided by the rainfall intensity regardless of the thickness of the surface. The seepage analysis also clarified the link between rainfall intensity in each thickness of the surface and the time necessary for the formation of groundwater levels in the soil layers.

6. GROUND WATER LEVEL ANALYSIS

A portion of rain water evaporates from the surface of ground, and some is also intercepted by objects such as trees and the grasses. The rain water that infiltrates into the ground forms a high moisture content belt (HMCB) and descends from the surface to the bottom. When the HMCB reaches the basement rock, it flows here as underground water, and it flows out to the surface of the ground when the water table reaches the surface. An equilibrium relation exists among the amount of rainfall supplied in a certain period, the amount saved on the surface, and the volume of water that flows out from the surface. Here, it is thought that the amounts of evapotranspiration and that intercepted by trees and grasses are very small compared with the amount of the rainfall, and those were neglected. If all the amounts of rainfall infiltrate in the ground, the following equation can be derived:

$$R_{input} = Gw + Gw_{out} \tag{3}$$

where, R_{input}= amount of rainfall, Gw= amount of rainfall saved in the layer, and Gw_{out}= net amount of water flowing out due to the groundwater flow.

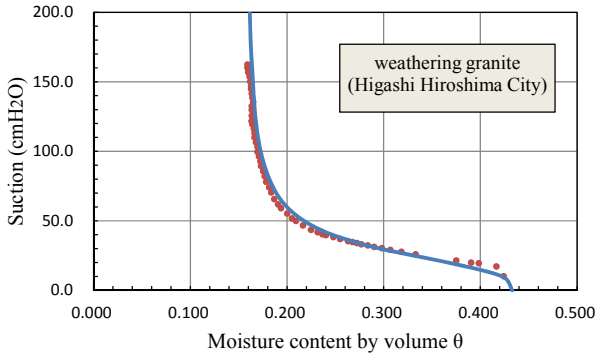

Fig. 6. Soil moisture characteristic curve used in this study (Yuri, 2010).

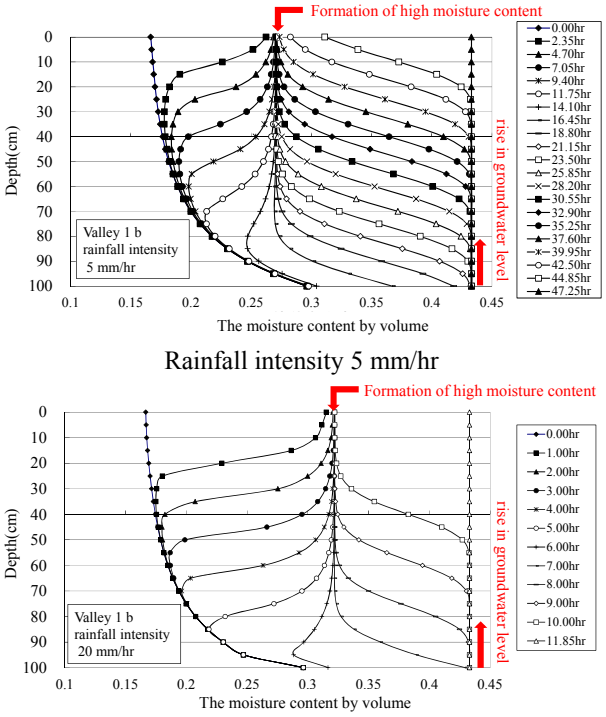

Fig. 7. Change of volumetric moisture content.

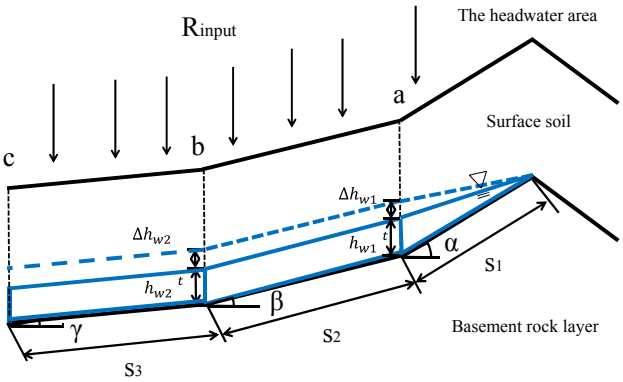

Fig. 8. High moisture content belt descent process, and groundwater level rise process.

Fig. 8 showed the computing model of the groundwater level rise.
Water change for each Δt (hr) at Point a of Fig. 8.The amount of rainfall between the ridge and Point a is:

$$R_{input} = r \times s_1 \cos\alpha \times \Delta t \tag{4}$$

where, r=rainfall intensity(mm/hr), s_1= slope length(m).
The amount saved as underground water in the ground of Section S_1 in Δt is:

$$Gw = \frac{1}{2} n_e \left(h_{w1}^t + \Delta h_{w1}\right) s_1 \cos\alpha - \frac{1}{2} n_e h_{w1}^t s_1 \cos\alpha \tag{5}$$

where, n_e=effective porosity, h_{w1}^t=groundwater level of Point a in t (m), and Δh_{w1}=groundwater level rise amount of Point a in Δt (m).
In addition, the amount where underground water flows of Section S_1 in Δt is:

$$Gw_{out} = k \sin\alpha \cdot h_{w1}^t \cos\alpha \cdot \Delta t \tag{6}$$

where, k= hydraulic conductivity.
By substituting Equations (4), (5), and (6) into Equation (7), we obtain the following:

$$h_{w1}^{t+\Delta t} = \frac{2\left(r \cdot s_1 - k \sin\alpha \cdot h_{w1}^t\right) \cdot \Delta t}{s_1\left(\theta_s - \theta_h\right)} + h_{w1}^t \tag{7}$$

where, $h_{w1}^{t+\Delta t}$ =groundwater level of Point a in Δt (m), θ_s = saturated moisture content by volume.
Water change for each Δt (hr) in Point b of Fig. 8.As well as the Equation (7):

$$h_{w2}^{t+\Delta t} = \frac{2\left\{r \cdot s_2 - k \sin\beta \cdot \left(h_{w2}^t - h_{w1}^t\right)\right\} \cdot \Delta t}{s_2\left(\theta_s - \theta_h\right)} + h_{w2}^t + h_{w1}^t - h_{w1}^{t+\Delta t} \tag{8}$$

where, $h_{w2}^{t+\Delta t}$ =groundwater level of Point b in Δt (m), h_{w1}^t =groundwater level of Point a in t (m), s_2= slope length (m) .
Equation (7) is used in Point a of Fig.8. Equation (8) is used in the other Points of Fig.8.
Fig. 9 shows the changes with the lapse of groundwater level.

7. SLOPE STABILITY ANALYSIS AND RISK ASSESSMENT

Results of the one-dimensional unsaturated seepage analysis, the slope stability analysis in the high-moisture belt descent process, and the groundwater level rise process were accomplished based on the physical property values obtained in the in situ geotechnical investigation, and on the estimated strength parameters. Fig. 10 shows the high moisture belt descent process and the groundwater level rise process. The slope stability analysis was done as a slide surface with a

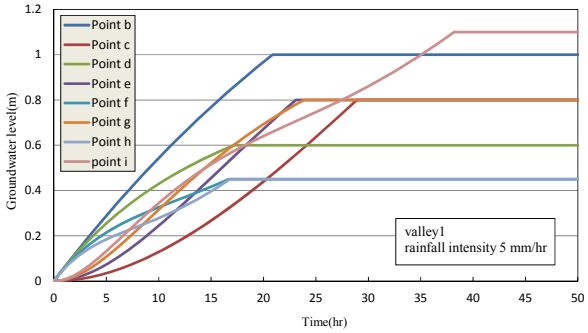

Fig. 9. Groundwater level with the lapse of time after HMCB reaches the bottom of lay (Valley 1).

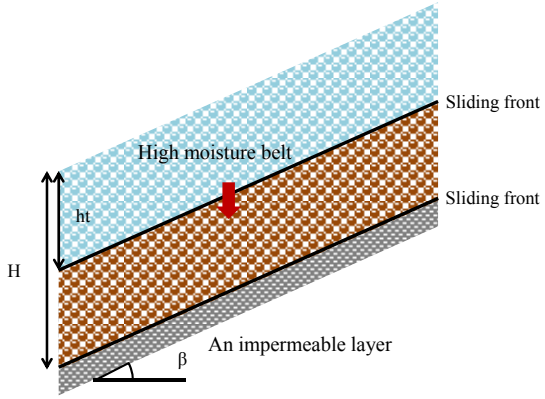

High moisture content belt descent process

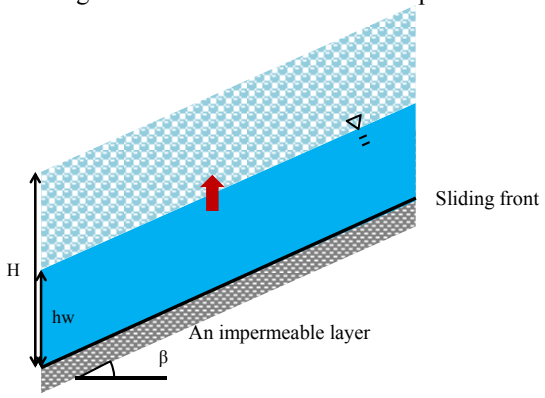

Groundwater level rise process

Fig. 10. High moisture content belt descent process, and groundwater level rise process.

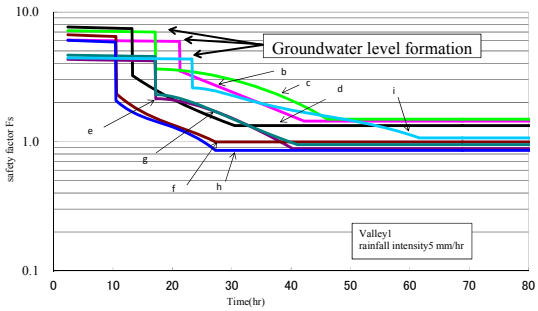

Fig. 11. Changes with the lapse of time of safety factors of a slope.

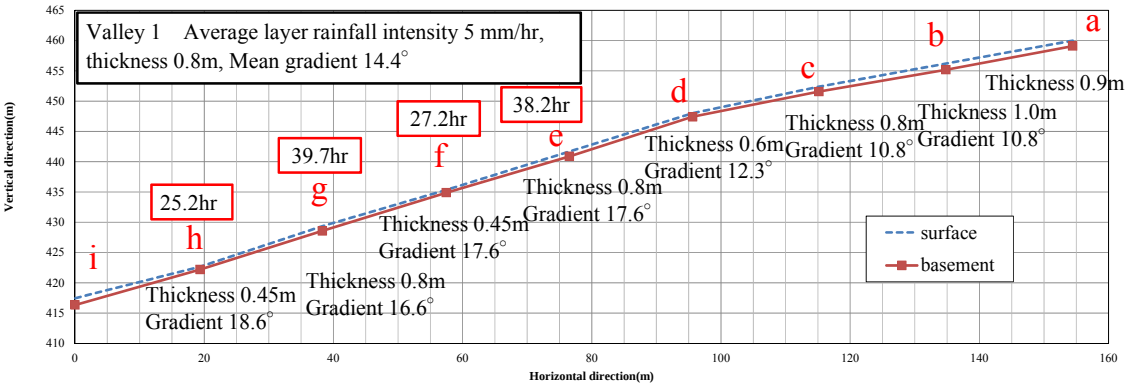

Valley 1

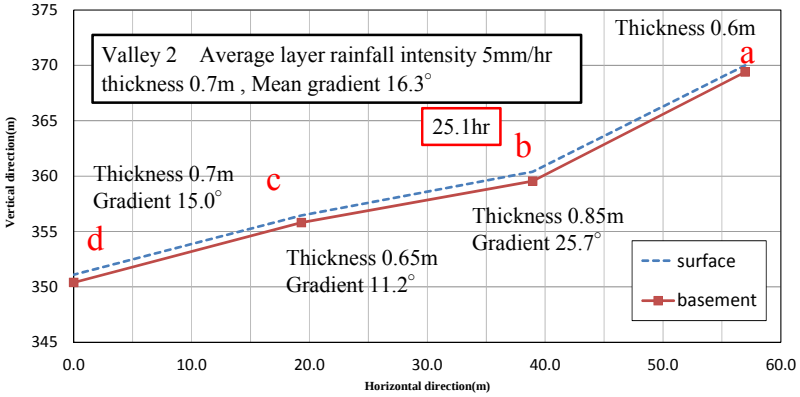

Valley 2

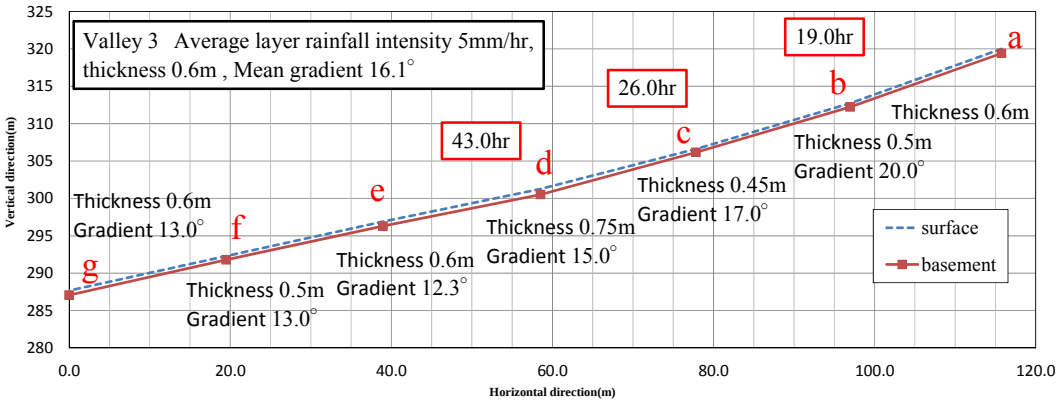

Valley 3

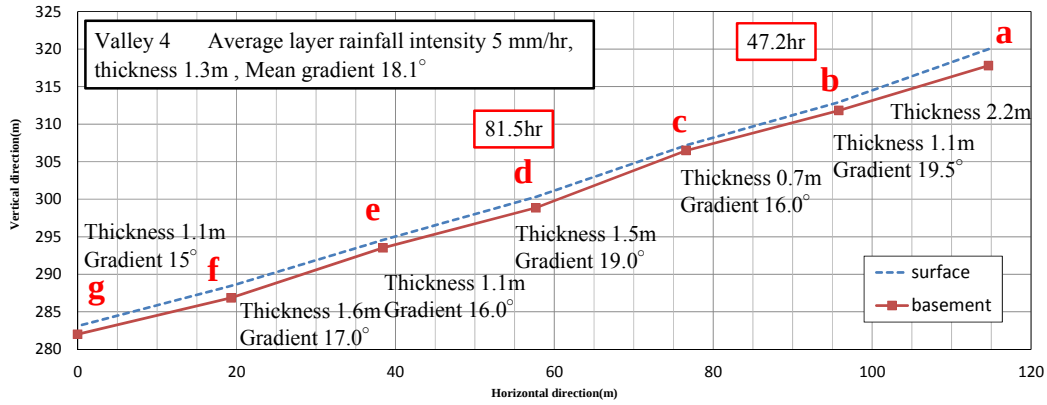

Valley 4

Fig. 12. Time in which the safety factor of a slope becomes less than one (Rainfall intensity 5 mm/hr).

basement rock and a lower side of the high moisture belt during the HMCB descent process, and as a slide surface with the basement rock during the groundwater level rise process. Slope stability analyses were also carried out in different rainfall conditions: in the various points of the valleys. those being, rainfall intensities of 5 mm/hr, 20 mm/hr, and 50 mm/hr. Fig. 11 shows the results of the slope stability analysis with a rainfall intensity of 5 mm/hr in Valley 1. In addition, Fig. 12 shows the required time in which the safety factor of the slope becomes less than one, in the points in Valley 1 when the rainfall intensity is 5 mm/hr.

Table 2 shows the risk assessments of the four valleys relatively. In Table 2, the risk assessment points in each valley are given by:

- Time when a safety factor of a part of the valley becomes less than 1.0.
- Range of the valley where the safety factor becomes less than 1.0

And finally, the total risk assessment value was calculated as a sum of the three risk assessment points. It was shown that Valley 1 is the most dangerous. However, a social importance, the number of residences downstream is not thought this study. It will be necessary to investigate social importance in the future.

Table 2. Relative risk assessment of four valleys.

	Valley 1	Valley 2	Valley 3	Valley 4
Maximum slope gradient(°)	18.6	25.7	20.0	19.5
Average thickness of the surface soil(m)	0.8	0.7	0.6	1.3
Time that the safety factor of slope becomes less than one in rainfall intensity 5mm/hr(hr)	25.2	25.1	19.0	47.2
Time that the safety factor of slope becomes less than one in rainfall intensity 20mm/hr(hr)	5.2	7.7	5.2	12.2
Time that the safety factor of slope becomes less than one in rainfall intensity 50mm/hr(hr)	2.3	3.7	2.4	5.7
Risk assessment point 1 1) Time that it becomes less than safety factor 1 （On a scale of 1 to 5）	4.1	3.8	5	1
Risk assessment point 2 2) Range that it becomes less than safety factor 1 （On a scale of 1 to 5）	5	1	3	3
Total risk assessment overall risk assessment （On a scale of 1to10）	9.1	4.8	8	4

8. CONCLUSION

In Hiroshima Prefecture, the prefectural land is divided into 350 unit areas of 5 kilometers square, and in each unit area, the criteria using the rainfall indexes, such as the soil water index and rainfall intensity, are determined on the basis of past records of landslide disasters due to heavy rain. However, in this system, the risk of individual valleys or natural slopes in each area cannot be shown. In this study, a series of in-situ geotechnical investigation of four potentially dangerous valleys inn Higashi-Hiroshima City were carried out. Models of the valleys for the geotechnical analysis were constructed by the investigation results. The one-dimensional infiltration analysis during the rain, the ground water seepage analysis, and the slope stability analyses when the rainfall intensities were 5, 20, and 50 mm/hr were continuously carried out. Based on these analysis, the risk of the four valleys were shown quantitatively .The risk of slope failure for each of four valleys was given as the risk assessment point, and was compared and discussed. The methods developed in this study are a useful to assess the landslide risk of individual slopes in potentially dangerous areas.

REFERENCES

[1] Higashi Hiroshima City: http://www.city.higashihiroshima.hiroshima.jp/site/bousai/hazard.html

[2] Hiroshima Prefecture, http://www.pref.hiroshima.lg.jp/page/1171592994610/index.html

[3] Langton, D.D., “The PANDA-lightweight penetrometer for soil investigation and monitoring material compaction,” Ground Engineering, September 1999, pp. 33-37.

[4] Cassan, M., “Les essays in situ en mechanique des sols, realization et interpretation,” Eyrolles, Paris, 2nd ed. Vol. 1, pp. 146-151.

[5] Tsuchida T, Athapaththu A.M.R.G., Kano S, Suga K, “Estimation of in-situ shear strength parameters of weathered granitic (Masado) slopes using lightweight dynamic cone penetrometer,” Soils and Foundations, vol. 51, No. 3. (to be published), 2011.

[6] Richards,L.A. , “Capillary Conduction of Liquids in Porous Mediums,” Physics 1, 1931, pp. 318-333.

[7] Yuri H, “Influence of rainfall characteristics and soil properties on soil moisture change,” master's thesis of graduate school of Hiroshima university, 2010, pp. 61-89.

First International Conference on Geotechnique, Construction Materials and Environment, Mie, Japan, Nov.21-23, 2011, ISBN: 978-4-9905958-0-7 C3051

Analyses of Piping under Foundation of Weirs in Different Ground Density by FEM

OKAJIMA Kenji, Department of Environmental Science and Technology, Mie University

ABSTRACT: Creep flow theories that are Bligh's and Lane's equation have been used as the safety criteria against piping under foundation of weirs. These methods were not able to estimate the mechanism leading to piping under foundation of weirs. In this study the effectiveness of our FEM for piping analysis under foundation of weirs was verified by model experiments.

These model experiments were carried out in five patterns and had same creep length by changing the installation position and length of cut-off wall in high ground density. These critical water heads of model experiments were different from each pattern. It was clear that creep flow theories were not able to predict these differences in high ground density.

The finite element analysis employs the elasto-plastic constitutive equations with a non-associated flow rule and strain hardening-softening. The constitutive equations based on the yield function of Mohr-Coulomb and the plastic potential function of Drucker-Prager. The finite element is 4-noded iso-parametric element with one point integration. The explicit dynamic relaxation method combined with the generalized return-mapping algorithm is applied. The elasto-plastic constitutive relations including the effect of the shear band are employed. A simplified and generalized version of mesh size-dependent softening modulus method (Tanaka and Kawamoto, 1989) is used in this study.

Our FEM predicted these critical water heads of model experiments. Maximum shear strain contour line by our finite element analysis indicated that shear strain concentrated in similar soil mass as Terzaghi assumed in the seepage failure equation. The analyses of piping under foundation of weirs in different ground density indicated that the critical water head approach to constant with the position of cut-off wall in loose ground density and the domain for concentration of maximum shear strain in same weir shape changed by each ground density.

Keywords: Piping, Creep theory, FEM, Relative density

1. INTRODUCTION

Creep flow theories are applied to the design criteria against piping of foundation of a weir. Bligh's creep flow theory was developed as the empirical equation for the design of floating type weirs in permeable layer through many experiences in 1910 (Bligh)[1]. After suggestion of this theory it was indicated that vertical sections of the creep length contribute more to reduce the danger of piping than horizontal sections of the length. In the response to this, Lane (1935)[2] suggested the weighted creep flow theory. These creep flow theories were based on the assumption that the cause of piping was erosion along the contact surface between soils and weir.

The purpose of this study is the reexamination of these practical safety criteria against seepage failure. We conducted a series of model experiments that have same creep length, and then evaluated these practical safety criteria and the validity of the elasto-plastic FEM by applying to the experiments in high relative density sand.

The condition of the foundation of weir is different in each weir. So we estimated the impact of relative density in the foundation of the weir on the critical water head by the elasto-plastic FEM.

2. CREEP THEORIES

To prevent piping at the down-stream side of a weir, practical manuals indicate that a safe creep length have to be ensured under the surface of the weir and along the side of the weir. The creep length to be ensured must be larger than the values calculated by two methods.

The first method is Bligh's method.

$$L_B \geq C_B \Delta H \tag{1}$$

Where L_B is the creep length that is measured along the bottom face of the weir, C_B is Bligh's creep ratio which varies depending on the type of the foundation soil, and ΔH is the water head. For example the fine sand C_B is 15. The critical head is ΔH_{CB} when $L_B = C_B \Delta H_{CB}$.

The second method is Lane's method.

$$L_L \geq C_L \Delta H \tag{2}$$

Where L_L is the weighted creep length.

$$L_L = \sum l_v + k_v / k_h \sum l_h \tag{3}$$

Where, l_v is the creep length of vertical direction (inclination angle of more than 45 degrees), l_h is the creep length of horizontal direction (inclination angle of lower than 45 degrees). k_v is the vertical coefficient of permeability and k_v is the horizontal coefficient of permeability. However, k_v / k_h has been used 1/3 customarily. C_L is Lane's creep ratio which varies depending on the type of the foundation soils. For example the fine sand C_L is 7.0. ΔH is the water head. The critical head is ΔH_{CL}, when $L_L = C_L \Delta H_{CL}$.

3 MODEL EXPERIMENTS

The experimental apparatus was consisted of a glass-walled

sand box. The size was 1000mm long, 500mm high and 200mm wide. The permeable layers in these model experiments were made by using clean sand. The sand was the Toyoura sand with a specific gravity of 2.64, a mean diameter (D_{50}) of 0.16 mm and a uniformity coefficient of 1.46. The weir was made of rigid acrylic plates. The weir was fixed to sand box and was sealed by silicon rubber and silicon adhesion bond to prevent water and sand from spilling out. The sandpaper was pasted on the bottom and side of the weir to prevent roofing. The cut-off wall was made of aluminum plate. The sand layers were prepared by pouring dry sand using hopper into stored water and deleting air during the soil particle falling. The high density of the sand layers was obtained: the relative density was about 85% (Figure1).

After setting up the water levels of both upstream and downstream side equal, the downstream water level was lowered incrementally (5mm after an hour). The deformation of the sand layer was measured. When piping or boiling occurred, the water head was defined to attain the critical water head.

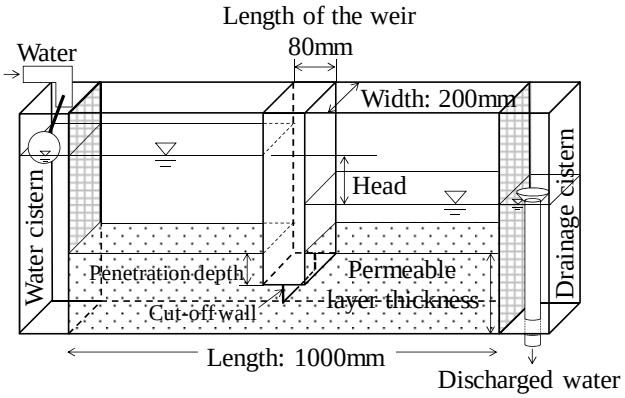

Figure 1 The layout of the test apparatus

The data of a series of model experiments are indicated in Figure2. All patterns had same creep length in which Bligh's creep length is 180mm and Lane's creep length is 123mm. These data were obtained by conducting 2 or 3 times in each experiment. These experiments are divided into 3 groups (Figure1). The first group was named "Depth group" to change penetration depth of the weir: 10-40-M, 20-30-M and 50-0 (penetration depth - depth of cut-off wall - the position of cut-off wall). From these experiments we can evaluate the influence of the depth of the weir for piping. The second group was named "Position group" to change the position of a cut-off wall: 10-40-L, 10-40-M and 10-40-R. From these experiments we can evaluate the influence of the position of the cut-off wall for piping.

Table1 shows results of model experiments that are relative density (%), critical water head, the kind of seepage failure (Piping or Boiling) and average of critical water head. Piping was observed in some patterns of model experiments. The heaving was observed because sand ground in down-stream side deformed. Relative densities were about 85% from 81.2% to 88.9%. Critical water heads in each pattern were similar water heads. In these model experiments the reproducibility was observed.

These model experiments had same creep length. Bligh's and Lane's creep flow theories predict a critical water head with patterns. However, each critical water head was different from the other pattern. The result indicated that creep flow theories were not able to predict the critical water head in the hard foundation.

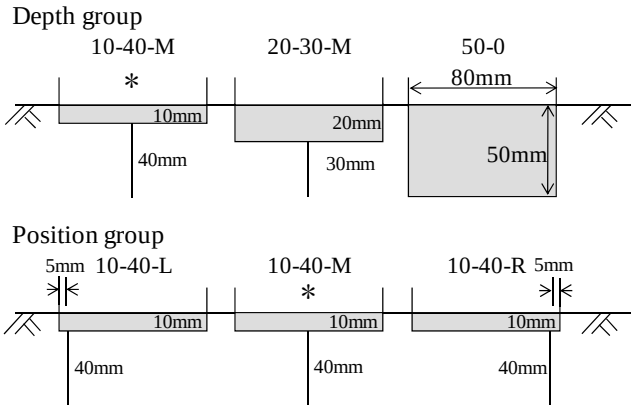

Figure 2 Patterns of model experiments

Table1 Results of model experiments

Pattern		Relative Density %	Critical water head mm	Piping / Boiling	Average of critical water head mm
	10-40-M	82	80	Piping	87
		86.3	90	Piping	
		83.6	90	Piping	
	20-30-M	84.7	140	Piping	137
		86.1	145	Boiling	
		84.5	125	Piping	
	50-0	88.9	250	Boiling	258
		85.1	251	Boiling	
		81.4	271	Boiling	
	10-40-L	87.4	70	Piping	73
		81.2	75	Piping	
		81.5	75	Piping	
	10-40-R	82.6	155	Boiling	170
		83.1	175	Boiling	
		87.4	180	Boiling	

4 SEEPAGE FAILURE ANALYSES BY ELASTO-PLASTIC FEM

4.1 Finite element method and analysis conditions

In this study the finite element analysis consisted of two steps. The first step is the seepage flow analysis by FEM. The second is the seepage failure analysis by the elasto-plastic FEM to input effective stress regarding the seepage force as the external force.

The finite element analysis employs the elasto-plastic constitutive equations with a non-associated flow rule and strain hardening-softening. The constitutive equations based

on the yield function of Mohr-Coulomb and the plastic potential function of Drucker-Prager. The finite element is 4-noded iso-parametric element with one point integration. The explicit dynamic relaxation method combined with the generalized return-mapping algorithm is applied. The elasto-plastic constitutive relations including the effect of the shear band are employed.

A simplified and generalized version of mesh size-dependent softening modulus method (Tanaka and Kawamoto, 1989)[3] is used in this study. A material model for a real granular material (i.e., Toyoura sand) with a high angle of internal friction is used with the features of nonlinear pre-peak, pressure-sensitivity of the deformation and strength characteristics of sand, non-associated flow characteristics, post-peak strain softening, and strain-localization into a shear band with a specific width. The material model will be briefly described in this section.

In the elasto-plastic finite element analysis, the material constants of Toyoura sand are as follow: relative density = 88%, residual friction angle = 33 degree. The calibration of the other elasto-plastic parameter of air-dried Toyoura sand in the elasto-plastic constitutive model was performed using the plane strain compression tests by Tatsuoka et al (1993)[4]. The analysis was performed using a series of finite element mesh of each model experiment, as shown in Figure3. Elements around the weir were consisted of 2mm square mesh. Elements bordering on the weir were boundary elements and the friction was set to be equal to the friction between sand and weir in these elements.

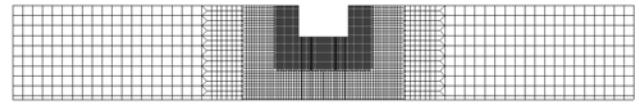

(a) All mesh of 50-0 mesh

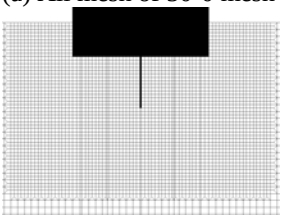

(b) 20-30-M mesh

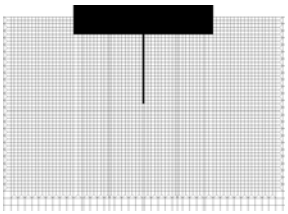

(c) 10-40-M mesh

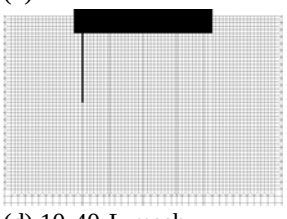

(d) 10-40-L mesh

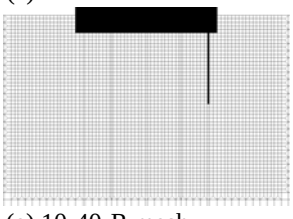

(e) 10-40-R mesh

Figure3 FEM mesh

4.2 The validation of this FEM

Result of model experiments and FEM in each groups are discussed about the effectiveness of FEM and the tendency of seepage failure of foundation of the weir. Figure4 indicates the critical water head of Position group. The critical water head gradually increases with the moving to the downstream end of the weir in Position group which has same creep length. Results of FEM predicted each critical water head well. Figure5 indicates the critical water head of Depth group. The critical water head gradually increases with the increasing the penetration depth of the weir in Depth group which has same creep length. Results of FEM predicted each critical water head well.

Results of FEM which penetration depth of weir was 10mm and the cut-off wall was set at upstream side or middle of the length of weir were computed higher than results of model experiments (10-40-M and 10-40-L). The reason is considered that the continuum model might not hold true when number of particle of sand (the average particle side is 0.16mm) was about 60 at the downstream edge of the weir. Result of FEM which penetration depth of weir was 50mm was computed lower than results of model experiment (50-0). The reason was considered that the friction of the side glass wall influenced the water head of boiling because it was observed that larger sand mass moved during the boiling in the model experiments of 50-0. These discussions indicated that our FEM was effective analysis to compute the critical water head of the foundation of the weir.

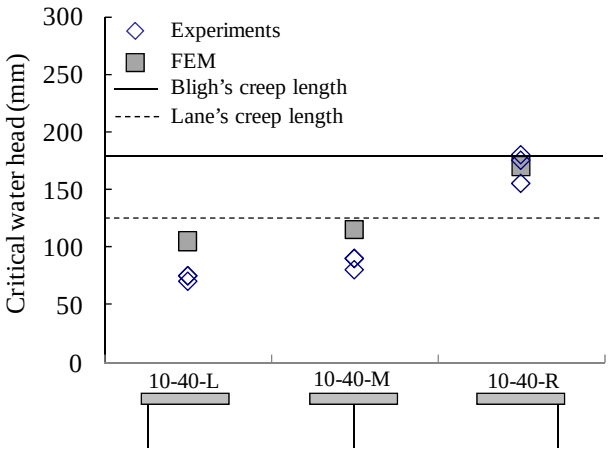

Figure 4 Critical water head of Position group

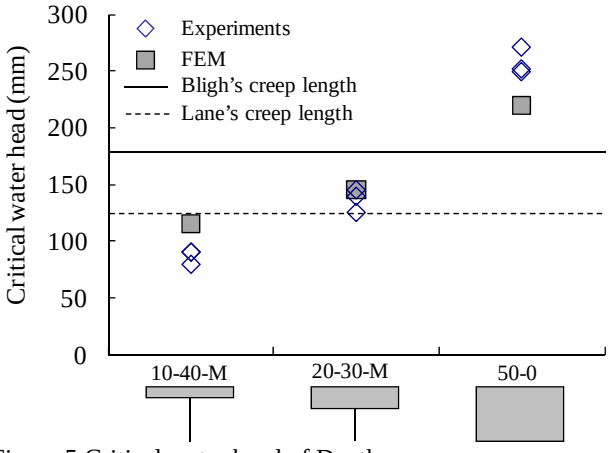

Figure 5 Critical water head of Depth group

5 SEEPAGE FAILURE OF THE FOUNDATION IN DIFERENT RELATIVE DENSITY

5.1 Finite element method and analysis conditions

It was considered that the foundation of the weir had various densities. In this study the effectiveness of our FEM was verified on the seepage failure of the foundation of the weir. The effectiveness of our FEM had been verified on the seepage failure of the ground around the sheet pile by Okajima et al. (2009)[5]. We considered that our FEM was able to be applied to the seepage failure problem in different relative density foundation.

We prepared the set of model cases to estimate the impact of relative density in the seepage failure of the foundation of the weir. Shapes of weirs were 10-40-L, 10-40-M, 10-40-R, 20-30-L, 20-30-M and 20-30-R. The tendency of seepage failure in the difference of the position of the cut-off wall and penetration depth of the weir was checked. Finite element meshes which were indicated in Figure 6 were applied to analyses of 20-30-L and 20-30-R. Conditions of relative density of the foundation were high(85%), middle(50%) and low(15%) in each weir shape.

5.2 Impact of relative density in seepage failure of weir

Critical water heads of finite element analyses was shown in Figure 7. Even when relative density was changed, each difference of critical water heads of the group of penetration depth 20mm and cut-off length 30mm (20-30 group) was much the same difference. On critical water heads of the group of penetration depth 10mm and cut-off length 40mm (10-40 group), each difference of critical water heads in high(85%) and middle(50%) relative density was much the same difference but critical water heads in low(15%) relative density were almost same.

To estimate the seepage failure mechanism of 10-40 group in low(15%) relative density, Figure8 showed the maximum shear strain distribution around the weir of 10-40 group in low(15%) relative density. The contour lines showed ten lines from 0.1 to 1.0 of maximum shear strain. Our elasto- plastic FEM has the frictional hardening-softening functions. When the maximum shear strain reached about 0.1, the frictional function changed from hardening regime to softening regime. We evaluated that the shear band develops in these elements at that time. The concentration of maximum shear strain contour line reached under downstream edge of the weir in 10-40-L and 10-40-M. This indicated that seepage failure progressed in the ground of downstream in 10-40-L and 10-40-M. On the other hand the concentration of maximum shear strain contour line reached under upstream edge of the weir in 10-40-R. The seepage failure of 10-40-R which had shallow penetration depth progressed from upstream. 10-40 group of low(15%) relative density had almost same critical water head, but the mechanism of seepage failure of each weir was different. And critical water heads of 10-40-R in middle(50%) and high(98%) were near to critical water heads of 20-30-R in middle(50%) and high(98%). Critical water heads of 20-30-L and 20-30-M and critical water heads of 10-40-L and 10-40-M were near each other. It indicated that the seepage failure of the foundation of the weir might depend on penetration depth of downstream side of the weir.

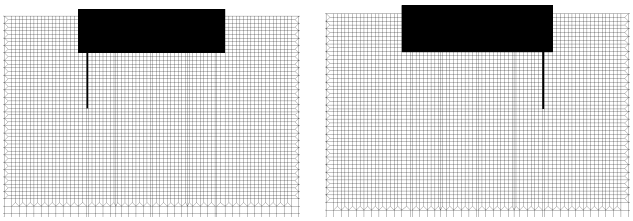

(a) 20-30-L mesh (b) 20-30-R mesh

Figure6 FEM mesh

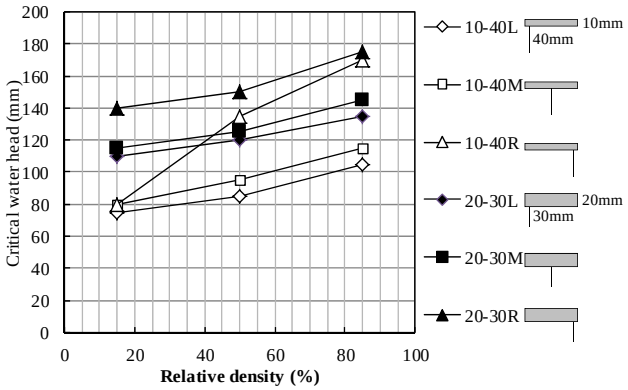

Figure7 Relationship of relative density and critical water head

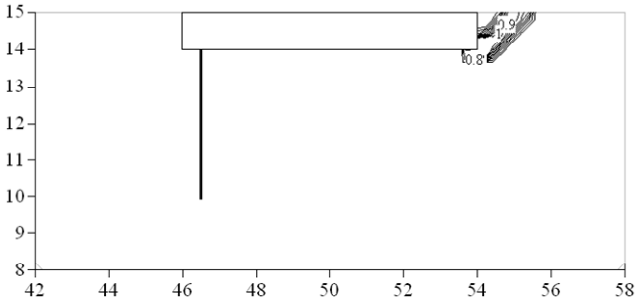

(a) Maximum shear strain distribution at water head 75mm of 10-40-L in low relative density (15%)

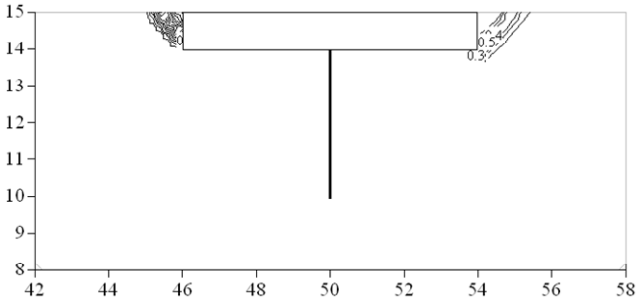

(a) Maximum shear strain distribution at water head 80mm of 10-40-M in low relative density (15%)

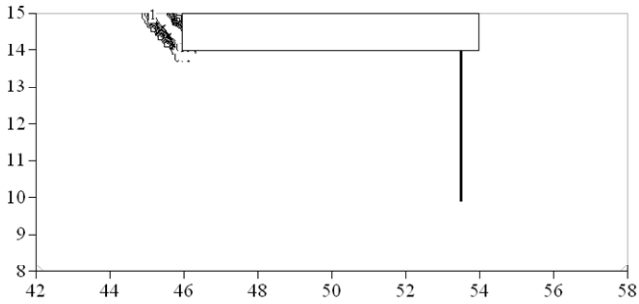

(a) Maximum shear strain distribution at water head 80mm of 10-40-R in low relative density (15%)

Figure8 Maximum shear strain distribution of elasto-plastic FEM

6 RESULT

Creep flow theories were reexamined by model six patterns experiments and finite element analyses that had same creep length by changing the installation position and length of cut-off wall in this study. These critical water heads of model experiments were different from each pattern. It was clear that creep flow theories were not able to predict the critical water head.

Our FEM predicted these critical water heads of model experiments.

We estimate the impact of relative density in the seepage failure of the foundation of the weir. Difference of each critical water head depending on position of cut-off wall was less affected by relative density. When the penetration depth of the weir was shallow, however, difference of each critical water head depending on position of cut-off wall was few by the difference of mechanism of seepage failure.

7 REFERENCES

[1] Bligh, W. G., “The practical design of irrigation works”, London Constable, 1910, pp.162-205

[2] Lane, E.W., “Security from Under seepage Masonry Dams on Earth Foundations”, Trans. ASCE, vol. 100,1935, pp.1234-1351

[3] Tanaka, T. and Kawamoto, O., “Three dimensional finite element collapse analysis for foundations and slopes using dynamic relaxation”, Proc. of Numer. Meth. in Geomech., 1988, pp.1213-1218

[4] Tatsuoka, F., Siddiquee, M. S. A, Park, C. S., Sakamoto, M. and Abe, F., “Modeling Stress-Strain Relations of Sand”, Soils and Foundations, vol.33(2), 1993, pp.60-81

[5] Okajima, K, Tanaka, T, Zhang, S and Komatsu, T, “Model experiments and elasto-plastic finite element analysis about seepage failure of sand behind fixed sheet pile”, Transactions of the JSIDRE, vol.260, 2009, pp.107-112

First International Conference on Geotechnique, Construction Materials and Environment, Mie, Japan, Nov.21-23, 2011, ISBN: 978-4-9905958-0-7 C3051

Shear Deformation and Failure of Sandy Slope According to Pore Pressure Generation due to Rainfall Infiltration

Sasahara K., Kochi University, Sakai N. , NIED

ABSTRACT: Monitoring of surface displacement of slope has been widely adopted as time prediction method of shallow landslide due to rainfall. Modeling of shear deformation according to rainfall infiltration is necessary for establishment of the method. In order to examine the constitutive relation for the model, surface displacement, pore pressure at the base, volumetric water content (hereafter, V.W.C.) and suction, shear strain in the sandy model slope are monitored during artificial rainfall. Analysis of the monitored data shows that surface displacement proceeds at small rate under unsaturated condition first, then increases remarkably with the rise of pore pressure at the base. Unsaturated component of surface displacement of steeper slope is larger than that of gentler slope. It is likely to be due to that shear strain with the increase of suction is larger in steeper slope while shear strain according to the increase of pore pressure is larger in gentler slope.

Keywords: Shallow landslide, Rainfall, Shear strain, Pore pressure, Suction

1. INTRODUCTION

The modeling of shear deformation of steep slope due to rainfall infiltration is necessary for the establishment of time prediction method of shallow landslide due to rainfall. Observations of deformation of the slope under artificial rainfall or specimen under anisotropic condition just before the failure had been implemented by some researchers [1]-[3], and produced the empirical law between time and deformation. The law has been adopted as the time prediction method based on the monitoring surface displacement [2], [3].

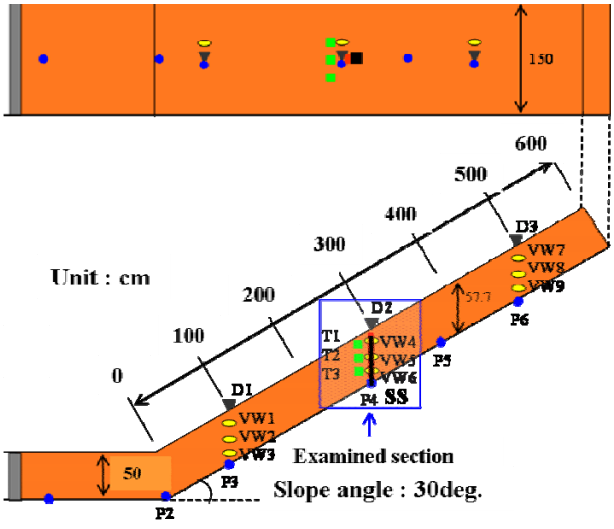

Fig.1 Geometry of model slope and location of monitoring devices

Because this method is empirical one, it does not take the change of stress in the slope into consideration. So it often failed to predict the time of failure of the slope under sudden change of rainfall intensity.

Recently some researches [4], [5] tried to observe slope deformation by Microelectro-mechanical system (MEMS) tilt-meter under the change of geometry of the slope such as cutting works, and other researches [6], [7] observe the deformation of the slope under artificial rainfall. Although they made much efforts to measure the slope deformation, they could not examine the mechanical law of the slope deformation.

In order to examine the constitutive law for the deformation of the slope under rainfall, the monitoring of V.W.C., suction, shear strain, pore pressure, and surface displacement are measured in the sandy model slope under constant rainfall in this paper. And some consideration are made in order to derive the relation between V.W.C., suction and shear strain, or that between shear strain and pore pressure in the slope under rainfall infiltration.

2. METHODOLOGY

2.1 Model slope and monitoring devices

Fig.1 shows the plane and longitudinal section of the model slope and location of monitoring devices with slope angle of 30deg. Model slope is made in a flume of 300cm length, 150cm width, and 50cm height at horizontal section, and 600cm length, 150cm width, and 50 cm depth at slope section (Fig.2). The flume has vertical steel blades of 1cm height located every 50cm in the longitudinal direction at the base of the slope in order to prevent slip between the soil mass and the base. Model slope is made of granite soil (Fig.3). The soil is filled and compacted horizontally at every 20cm thickness due to human stepping on the soil, and is managed to keep

Fig.2 Flume and model slope

void ratio of 1.46~1.52. Water content of the soil layer is 3.7~4.4%. The soil layer thickness is 50cm so that soil depth to gravitational direction is 57.7cm The base and upper boundary of the flume is undrained condition, while the lower boundary is drained condition.

In the model slope, soil moisture sensors (expressed as 'VW' in Fig.1) are installed at the depth of 10, 25, 40cm at 100, 300,500cm from the toe of the slope. They has the accuracy of 0.02 (m^3/m^3). Tensiometers (expressed as 'T' in Fig.1) are installed at the depth of 10, 25, 40cm at 300cm from the toe of the slope. They have accuracy of 1(kPa). Shear strain gauge (expressed as 'SS' in Fig.1) is installed at 300cm from the toe of the slope. It is series of tilt meter at every vertical depth of 9.2cm and tilt meters are connected by bolt and nut. So the meters can incline only to slope inclination direction. Shear strain increment at some depth $\Delta\gamma$ is defined as $\tan(\Delta\theta)$, while $\Delta\theta$ is the inclination increment of the tilt meter (Fig.4). Tilt meter has non-linearity of 0.2 degree which corresponds to that of 0.0035 for $\Delta\gamma$. Groundwater level (hereafter G.W.L.) gauges (expressed as 'P' in Fig.1) with the accuracy of 1cmH_2O are located at the base of the model at 0, 100, 300, 400, 500cm from the toe of the slope. The measurement data of the gauge at 100, 300, 500cm are used for the examination in this paper. Extensometers are installed at the surface of the slope. The location is 100cm, 300cm, 500cm from the toe of the slope. It has the non-linearity of 0.1mm

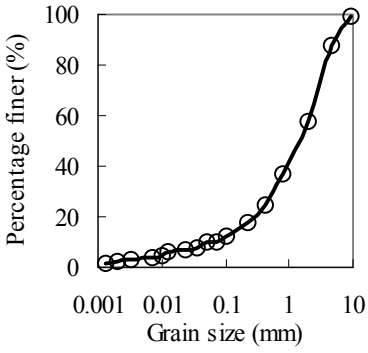

Fig.3 Grain size distribution of granite soil

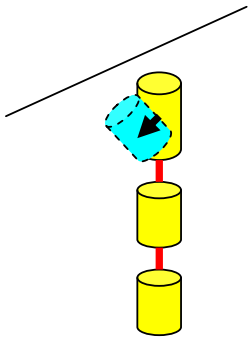

Increase of increment of tilt-meter :$\Delta\theta$

Shear strain increment $\Delta\gamma = \tan(\Delta\theta)$

Fig.4 Measurement of shear strain by tilt meter

2.2 Experimental conditions

2 types of model slope with different inclination 30deg. (Fig.1), 40deg. are prepared for the examination of the influence of the slope inclination to the relation between shear deformation and rainfall infiltration. The arrangement of measurement devices in the slope of 40deg. are just same with that of 30deg. The difference between the slope of 30deg. and that of 40deg. are soil layer depth to gravitational direction at the slope section of the model. Soil layer depth to gravitational direction of 30deg. is 57.7cm, while that of 40deg. is 65.3cm. Artificial rainfall with the constant intensity of 50 mm/h is sprayed from the rainfall simulator above the model slope until the onset of slope failure.

3. RESULTES OF EXPERIMENTS

Fig.5 shows time variation of V.W.C., suction and shear strain in the slope at 300cm from the toe of the slope, G.W.L. and surface displacement at 100cm, 300cm, 500cm from the toe of the model slope with 30deg inclination. Slope failure occurred at 5150sec. in the model slope of 30deg.. V.W.C. keeps constant just after the start of the experiment, then makes rapid increase earlier with shallower depth, and it continues to be almost constant after rapid rise. After constant value, V.W.C. at 40cm depth increases again at 4300sec. and that at 25cm also increase again at 5000sec., while that at 10cm keeps almost constant. Suction starts rapid decreasing earliest at 25cm at 500sec., then 40cm at 1300sec., and keeps almost constant negative value after that. Suction at 10cm keeps constant just after the start of experiment then makes rapid decrease at 3000sec. then makes second decrease at 6000sec.. Shear strain at each depth is almost zero until 3700sec., then increase rapidly. Shear strain at 4.6cm, 13.8cm, 23cm, and 50.6cm proceeds to positive while that at 32.2cm, 41.4cm proceeds to negative. Negative value may be due to reaction of tilt meter at this depth against large movement of tilt meters at upper or lower location. Time variation of G.W.L. and surface displacement at 100cm is almost same with those of 300cm, 500cm. This fact suggests that shear deformation and groundwater rise at any cross-section from 100cm to 500cm is almost same. G.W.L. continues slight decreases from the start of the experiment until 4000sec., and then makes remarkable increase after almost 4000sec.. Surface displacement also makes no increase until 4000sec., then increases rapidly. Surface displacement and shear strain in the slope makes remarkable increase after around 4000sec when G.W.L. starts rise. It suggests that shear deformation proceeds according to increase of pore pressure in the slope of 30deg..

Fig.6 shows time variation of V.W.C., suction and shear

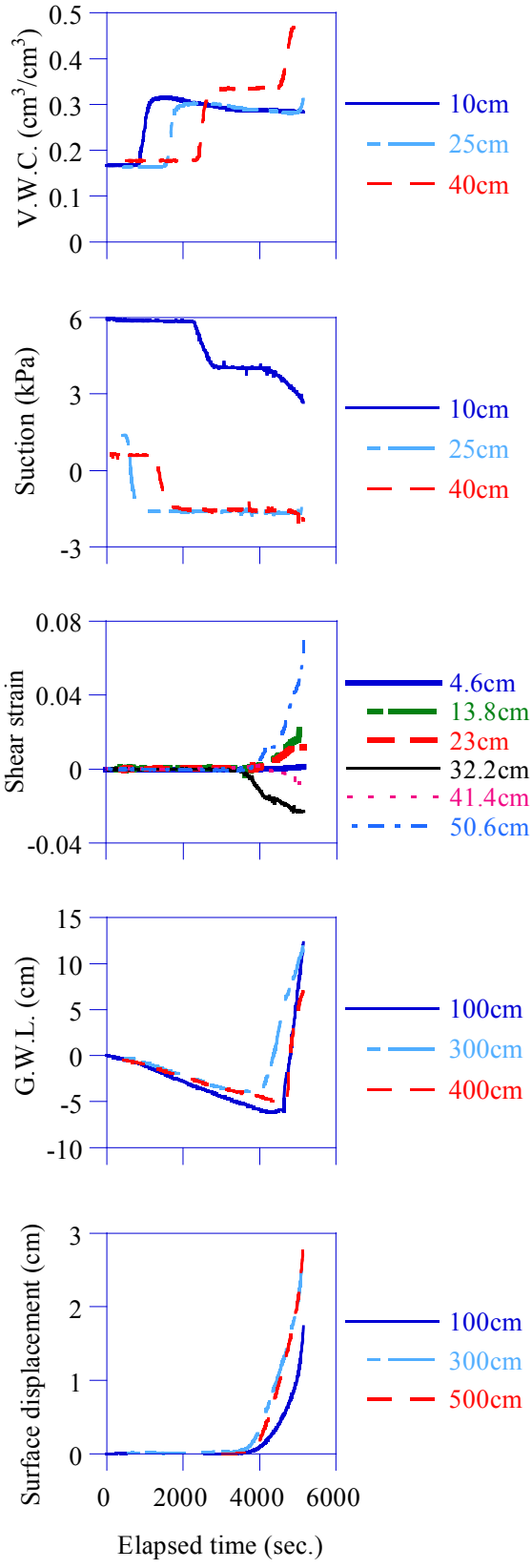

Fig.5 Time variation of V.W.C., suction, shear strain, pore pressure, and surface displacement (30 deg.)

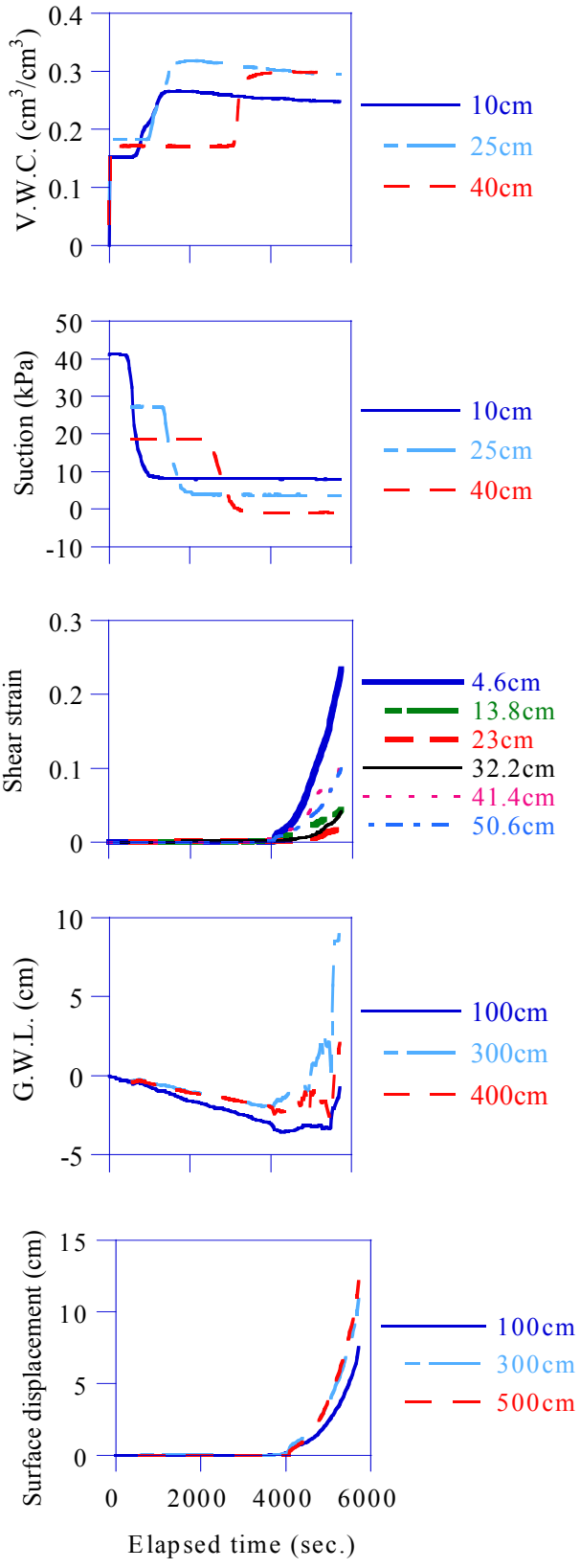

Fig.6 Time variation of V.W.C., suction, shear strain, pore pressure, and surface displacement (40 deg.)

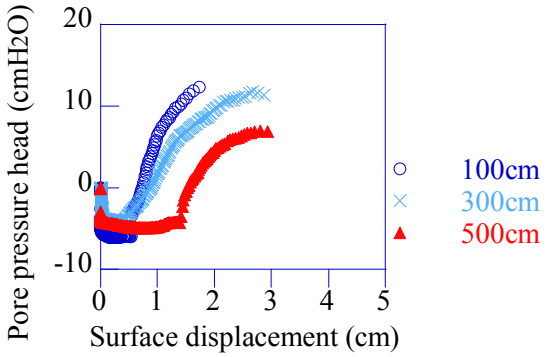

(a) 30deg.

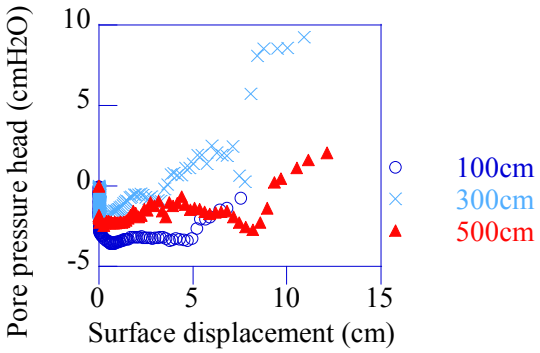

(b) 40deg.

Fig.7 Relation between surface displacement and pore pressure

strain in the slope at 300cm from the toe of the slope, G.W.L. and surface displacement at 100cm, 300cm, 500cm from the toe of the model slope with 40deg inclination. V.W.C. starts increase earlier at shallower depth, then keeps almost constant vale within 0.25~0.3. Suction also starts decrease earlier at shallower depth, then keeps almost constant value within 0~10 kPa. Shear strain make little variation until 4000sec., then remarkably increase to positive. G.W.L. keeps negative and continues slight decrease until 4000sec., then increase largely. G.W.L. at 100cm, 500cm is lower than that at 300cm.Surface displacement also shows almost no variation until 4000sec., then rapidly increases. Remarkable increase of shear strain and surface displacement starts around 4000sec. when G.W.L. starts rise also in the case of the model slope of 40deg.. It suggests that shear deformation in the slope of 40deg. also greatly influenced by generation of pore pressure.

4. DISCUSSION

4.1 Surface displacement and pore pressure

Fig.7(a) shows the relation between surface displacement and pore pressure head on the base at 100, 300, 500cm from the toe of the slope of 30deg.. Pore pressure head at the base is equal to G.W.L.. Pore pressure head decreases and then keeps -7~-3 cmH_2O just after the start of the experiment. Surface displacement increases under unsaturated condition with negative pore pressure at this stage. After the surface displacement of 0.5~1.4cm, it increases with the increase of pore pressure head. Surface displacement increment becomes larger as pore pressure head increase. So the relation between surface displacement and pore pressure head can be modified by hyperbolic curve which is often adopted for stress-strain relation of the element of soil. The unsaturated component and all surface displacement are 0.5 and 1.7cm for 100cm, 0.4 and 2.8cm for 300cm, 1.4cm and 2.9cm for 500cm. So the ratios of unsaturated component to all surface displacement are 0.29 for 100cm, 0.14 for 300cm, and 0.48 for 500cm in the slope of 30deg..

Fig.7(b) shows the relation between surface displacement and pore pressure head on the base at 100, 300, 500cm from the toe of the slope of 40deg.. Similar to the relation of the slope of 30deg., pore pressure sudden decreases just after the experiment and keeps -4~0 cmH_2O until surface displacement of 5~8cm. Surface displacement proceeds under unsaturated condition in this stage. Although pore pressure of 300cm fluctuates and rises up to 2cm in this stage, it can be thought negative. Fluctuation of pore pressure may be due to error of measurement. Surface displacement remarkably increases with increase of pore pressure after that. Even though pore pressure at the start of this stage of 100, 500cm is negative, this stage can be thought to be under generation of positive pore pressure. Negative value of pore pressure of -4~0 kPa might mean quasi-saturated condition near the base of the slope. The unsaturated component and all surface displacement are 5 and 7.9cm for 100cm, 7.8 and 10.9cm for 300cm, 8.2cm and 12.2cm for 500cm. So the ratios of unsaturated component to all surface displacement are 0.63 for 100cm, 0.72 for 300cm, and 0.8 for 500cm in the slope of 40deg.. The ratio of unsaturated component is larger in the slope of 40deg. than that of 30deg..

4.2 Suction and shear strain in the slope

Fig.8(a) shows the relation between suction and shear strain at the same depth in the slope of 30deg.. Suction decreases with small increase of shear strain in the soil layer shallower than 23cm. Especially shear strain at 4.6cm is almost zero even after the increase of suction up to 4 kPa. Suction is still positive after the decrease at those depths. At the depth shallower than 23cm, shear strain continues to be almost zero with the increase of suction up to -4~0 kPa of suction, then it proceeds under almost constant suction. Shear strain proceeds to positive at 23, 50.6cm while it proceeds to negative at 32.2, 41.4cm with positive constant suction..

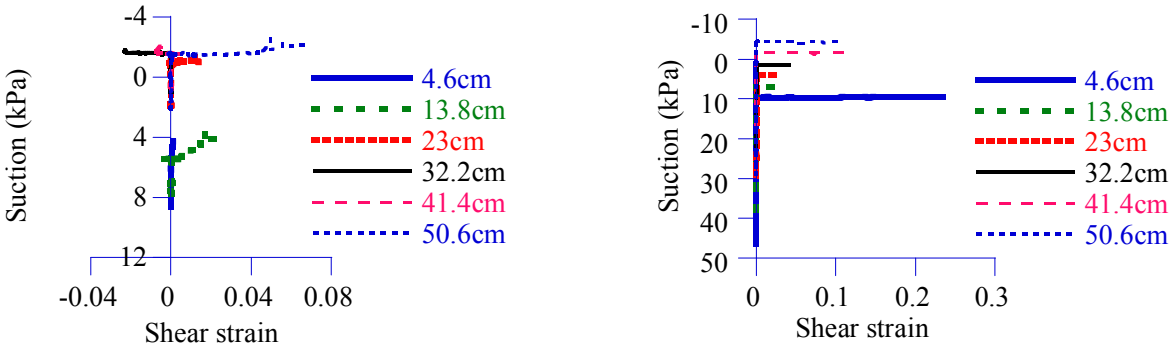

(a) 30deg. (b) 40deg.

Fig.8 Relation between shear strain and suction

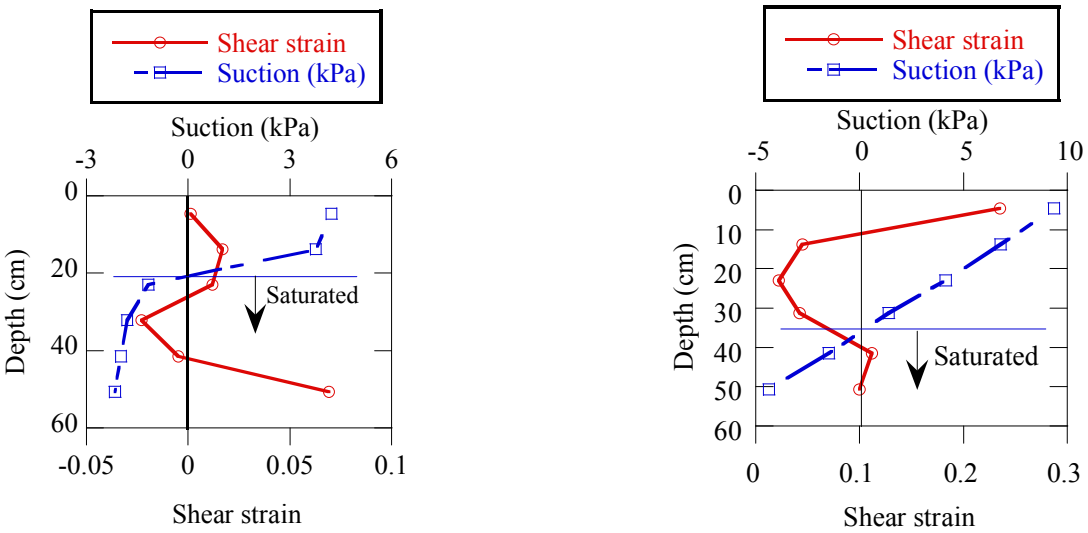

(a) 30deg. (b) 40deg.

Fig.9 Vertical profile of shear strain just before failure

Fig.8(b) shows the relation between suction and shear strain at the same depth in the slope of 40deg.. Shear strain keeps almost zero with the increase of suction at first, then proceeds with almost constant suction at all depths. Shear strain increases under positive suction (unsaturated condition) in the soil layer shallower than 32.2cm while it increases under negative suction at 41.4, 50.6cm. Shear deformation proceeds at unsaturated condition at deeper soil layer in the slope of 40deg. than that of 30deg..

Fig.9(a) shows the vertical profile of shear strain and suction at 300cm from the toe of the slope of 30deg.. Soil layer with negative suction is assumed to be saturated. Shear strain at deeper soil layer is larger than that near surface. Shear strain at 23~41.4cm depth is negative which might mean inverse movement of tilt meter at the depth corresponding to large movement of upper or lower tilt meter. Deeper soil layer is saturated. In the slope of 30deg., shear strain increases largely at saturated soil layer. Fig.9(b) shows the vertical profile of shear strain and suction at 300cm from the toe of the slope of 40deg.. Shear strain is larger near surface where suction is positive, while it is relatively smaller near the base which is saturated. In the slope of 40deg., shear strain increases largely at unsaturated soil layer.

4.4 Shear deformation under different slope inclination

According to the examination as above, shear deformation at saturated layer is larger in the gentler slope while shear deformation at unsaturated layer is larger in steeper slope. In order to compare the contribution of unsaturated component to shear deformation at examined section of the slope under different slope inclination, ratio of unsaturated part of shear

area under different slope inclination is calculated from Fig.9. Shear area is defined as sum of shear strain from one depth to other depth, and is derived by the equation below.

$$A = \int_{z1}^{z2} \gamma dz \quad (1)$$

Here, A: shear area, γ : shear strain at some depth, z1, z2: depth (z1<z2). Shear area under unsaturated layer and saturated area in each slope is calculated. The ratio of shear area of unsaturated layer are 0.17 for the slope of 30deg. while it is 0.58 for 40deg.. So contribution of shear deformation at unsaturated layer is larger in the steeper slope. It is same trend with the ratio of unsaturated component of surface displacement that is larger in the steeper slope.

5. CONCLUSION

From the examination as above, the facts as bellows are made clear.

(1) Surface displacement and shear strain in the slope makes remarkable increase at the time of rise of G.W.L.

(2) Surface displacement proceeds at unsaturated condition at first, then increase remarkably with the increase of pore pressure at the base. The relation between surface displacement and pore pressure is hyperbolic just like stress-strain curve of soil element. The ratio of unsaturated component to all surface displacement is larger in steeper slope.

(3) In the slope, shear strain proceeds under almost constant suction after rapid increase of suction. Unsaturated soil layer near surface is thicker in the steeper slope.

(4) Shear strain at saturated zone near bottom is larger than that at unsaturated layer in the slope of 30deg., while shear strain at unsaturated layer near surface is larger in the slope of 40deg..

(5) Contribution of unsaturated shear deformation is larger in steeper slope.

REFERENCES

[1] Saitou M and Uezawa H, "Failure of Soil Due to Creep", Proc. 5th International Conference on Soil Mechanics and Foundation Engineering, vol.1, 1961, pp.315-318.

[2] Saitou M, "Forecasting the Time of Occurrence of a Slope Failure", Proc. 6th International Conference on Soil Mechanics and Foundation Engineering, vol.2, pp.537-541.

[3] Fukuzono T, "A New Method for Predicting the Failure Time of a Slope", Proc. IVth International Conference and Field Workshop on Landslides, 1985, pp.145-150.

[4] Ito K and Toyosawa Y, "Field test of slope failure during slope cutting work", JSCE Journals, vol.65, no.1, 2009, pp.254-265(in Japanese with English abstract).

[5] Uchimura T, et. al., "Simple monitoring method for precaution of landslides watching tilting and water contents on slopes surface", Landslides, DOI 10.1007/s10346-009-0178-z., 2009.

[6] Moriwaki H, et. al., "Failure process in a full-scale landslide experiment using a rainfall simulator", Landslides, vol.1, no.4, 2004, pp.277-288.

[7] Ochiai H, "AFludaized landslide on a natural slope by artificial rainfall", Landslides, vol.1, no.3, 2004, pp.211-219.

First International Conference on Geotechnique, Construction Materials and Environment, Mie, Japan, Nov.21-23, 2011, ISBN: 978-4-9905958-0-7 C3051

Load Settlement Relationships of Circular Footings Considering Dilatancy Characteristics of Sand

Yusuke Tomita, Graduate Student, Dept. of Architecture, Faculty of Environmental and Urban Eng., Kansai Univ., M. Eng.
Tatsuaki Nishigata, Prof., Dept. of Civil, Environmental and Applied System Eng., Faculty of Environmental and Urban Eng., Kansai Univ., Dr. Eng.
Takeshi Masui, Assoc. Prof., Dept. of Architecture, Faculty of Environmental and Urban Eng., Kansai Univ., Dr. Eng.
Shintaro Yao, Prof. Emeritus, Kansai Univ., Dr. Eng.

ABSTRACT: In order to elucidate the mechanical properties of load-settlement relationships of spread foundations on sand ground, experimental and analytical study on strain hardening and dilatancy of sand is needed. Here we present the theoretical properties which were derived from circular footing model experiment and computer simulation. The model experiment was carried out through vertical loading on circular footing, and used relative density and tank dimensions as parameters. The quantitative relationship between load and settlement was analyzed through FEM simulation with SMP-Cam-Clay model, which is capable of estimating the dilatancy of sand. The results are summarized as follows; In both cases of dense and loose sand models, before reaching the ultimate load, the load-settlement relationship obtained from FEM simulation corresponded with that of obtained from the experiment. After reaching the ultimate load, "Terzaghi's bearing capacity line" corresponded with the load-settlement relationship obtained from the experiment. In the case of medium-dense sand models, some binding effect of a soil tank rectangle was recognized. The effect was considered to be exerted by the positive dilatancy of the sand, which occurred steadily with the settlement progresses.

Keywords: Spread Foundation, Sand Ground,
Load-Settlement Curve, Constitutive Equation, Dilatancy

1 INTRODUCTION

Although the quantitative load-settlement relationships of spread foundation have been experimentally well demonstrated on sand ground [1]–[4], the underlying mechanical properties of the relationships still remained to be elucidated. Especially, since little study has been done on the mechanical properties characterized through strain hardening and dilatancy of sand. Here we present the theoretical properties which were derived from circular footing model experiment and computer simulation. The model experiment was carried out through vertical loading on circular footing, and used relative density and tank dimensions as parameters. The quantitative relationship between load and settlement was analyzed through FEM simulation with SMP-Cam-Clay model. In addition, a part of the contents of this paper have been reported in [5], [6].

2 VERTICAL LOADING TEST OF CIRCULAR FOOTING

2.1 Test Pit and Loading Equipment

The model experiments were performed on Toyoura sand, with different relative densities. The Maximum and minimum densities of the sand, as determined by the standard procedure, are given in Table1. The loose sand models were built by pouring sand from containers. The density of the sand models is a unique-function of the height of free fall of sand. Medium-dense and dense sand models were built by vibration provided by an earthquake simulator. The soil tank was made of steel, which made the tank completely resistant to earth pressure. Teflon sheets with double layers of grease were set on the sides of the soil tank, in order to omit the friction caused by the experiment ground [7]. To study the effect of sand dilatancy on mechanical properties of the load-settlement relationship, soil tanks with different volumes were used in the experiments. The short side of the big soil tank was measured to be 400 millimeters in Fig.1-1 which shows the experimental device, whereas that of the small soil tank was 100 millimeters in Fig.1-2 which shows the experimental device. The model footing has a circular cross section with diameter of 20 millimeters, and is 80 millimeters in height. Moreover, the model footing is made of wood, and sandpapers are put on the tip [1]. In the following,

Table1 Specifications of the Experiment Ground

Density of Soil Particles ρ_s	2.558g/cm^3
Maximum Density $\rho_{d\,max}$	1.645g/cm^3
Minimum Density $\rho_{d\,min}$	1.337g/cm^3

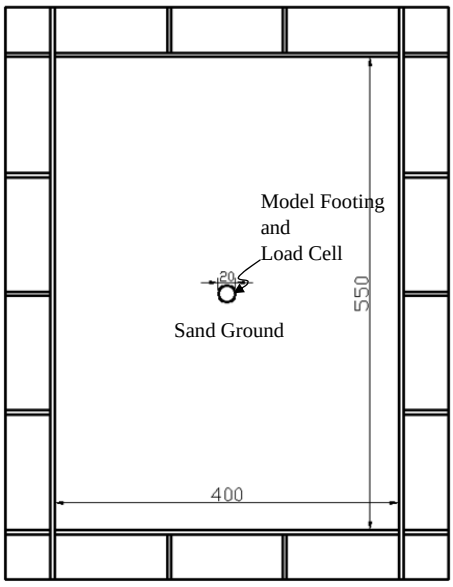

The Ground Plan : ℓ 20B (Unit : mm)

Fig.1-1 Experimental Device (ℓ 20B)

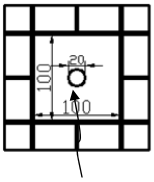

The Ground Plan : ℓ 5B (Unit : mm)

Fig.1-2 Experimental Device (ℓ 5B)

Table2 Experiment Name

Name	Relative Density D_r	Soil Tank
L-20B	20～30%	ℓ 20B
L-5B	20～30%	ℓ 5B
M-20B	50～60%	ℓ 20B
M-5B	50～60%	ℓ 5B
D-20B	80～90%	ℓ 20B
D-5B	80～90%	ℓ 5B

short side length of the soil tank is named ℓ , diameter of the model footing is named B, the soil tank that ℓ is 400 millimeters is named ℓ 20B, and the soil tank that ℓ is 100 millimeters is named ℓ 5B. In other words, ℓ 20B expresses that ℓ is 20 times of B, ℓ 5B expresses that ℓ is 5 times of B. Experiment name is shown in Table2. In Table2, L, M, and D indicate the loose sand ground, the medium-dense sand ground, and dense sand ground, respectively. Also, 20B indicates soil tank ℓ 20B, whereas 5B indicates ℓ 5B. The binding effect caused by the soil tank was treated as a negligible factor throughout the experiment. This was confirmed when the result of separate experiment conducted on dense sand ground using ℓ as 800 millimeters corresponded to that of D-20B [5]. Therefore, the binding effect was also considered to be negligible in the experiments of L-20B and M-20B.

2.2 Loading Procedure

300kN universal testing machine is used as a loading device. By vertical loading to the settlement rate 12.5μm/sec on the model footing, the quantitative load-settlement relationship was determined. In the case of loose sand models and medium-dense sand models, the load measured by load cell installed at the top of the model footing divided by the bottom area of the model footing was defined as the load. In the case of dense sand models, the load measured by load cell installed at the bottom of the soil tank divided by the bottom area of the model footing was defined as the load. In all the experiments, the amount of relative displacement between the soil tank and the loading plate of a universal testing machine was defined as the settlement. In the following, the load is named *p*, the settlement is named *S*. In lastly, loading was performed until *S* reached 10 millimeters.

2.3 Test Results

2.3.1 In the Case of Loose Sand Models

L-20B and L-5B were performed three times, each. As a result, the *p*-*S* relationship showed no significant variation. The results of two typical cases are shown by both logarithms indications in Fig.2. In any results of L-20B and L-5B, *p* steadily increases as the settlement progresses, and both results appear to be consistent. Based on [3], the ultimate load in *p*-*S* relationship was defined as a load at the point that shifts from a curve to a straight line. This point corresponds to an inflection point in log *p*-log *S* relationship. In any results of L-20B and L-5B, the inflection point was

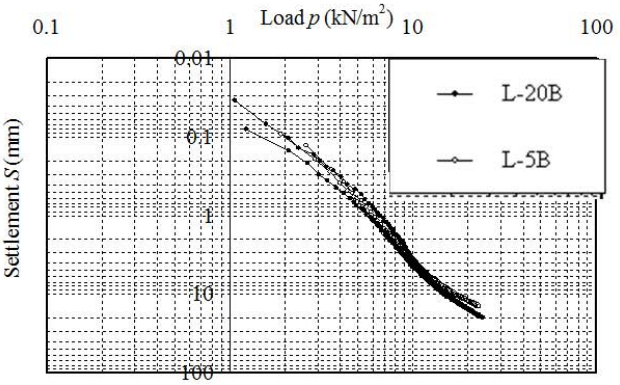

Fig.2 log*p*-log*S* Relationships (In the Case of Loose Sand Models)

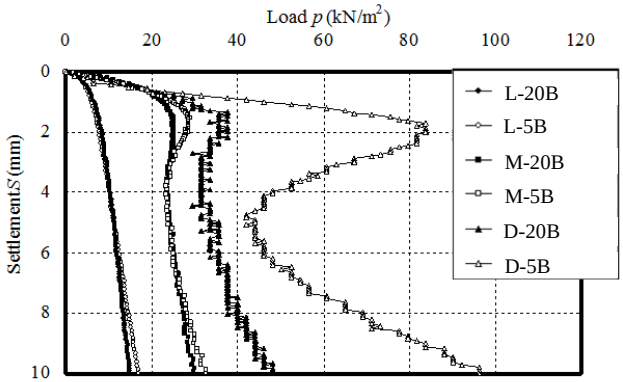

Fig.3 *p*-*S* Relationships (Comparison of the Relative Density)

confirmed when *S* reached 3 millimeters, so the load at this point was defined as the ultimate load. Probably because the loose sand ground under the model footing exhibit contractile behavior, the elevation of sand surface around the model footing did not appear in any results of L-20B and L-5B.

2.3.2 In the Case of Dense Sand Models

D-20B and D-5B were performed three times, each. As a result, the *p*-*S* relationship showed no significant variation. The result of a typical case is shown in Fig.3. In any results of D-20B and D-5B, *p* steadily increases until *S* reaches about 2.0 millimeters. Both results are almost consistent until *S* reaches 1.0 millimeters. But the stiffness on settlement of D-5B becomes larger than that of D-20B from 1.0 millimeters to 2.0 millimeters. As a result, *p* of D-5B is about 2.4 times larger than that of D-20B as *S* reached about 2.0 millimeters. From 2.0 millimeters to 4.5 millimeters, *p* steadily decreases as the settlement progresses where the rate of decrease in *p* of D-5B is about 6 times larger than that of D-20B. In any results of D-20B and D-5B, *p* then steadily increases again as the settlement progresses, and the stiffness on settlement of D-5B becomes larger than that of D-20B. In addition, in both results of D-20B and D-5B, the ultimate load was confirmed when *S* reached about 2.0 millimeters. The elevation of sand surface around the model footing appeared when *S* reaches about 4.5 millimeters in the result of D-5B. In this paper, the failure surface was decided to have reached the sand surface, based on the appearance of the elevation of the sand surface around the model footing [8].

2.3.3 In the Case of Medium-Dense Sand Models

M-20B and M-5B were performed three times, each. As a result, the *p*-*S* relationship showed no significant variation. The result of a typical case is shown in Fig.3. In any results of M-20B and M-5B, *p* steadily increases until *S* reaches about 1.6 millimeters. Both results are almost consistent until *S* reaches 0.8 millimeters. But the stiffness on settlement of M-5B becomes larger than that of M-20B from 0.8 millimeters to 1.6 millimeters. As a result, *p* of M-5B is about 1.2 times larger than that of M-20B at *S* reached about 1.6 millimeters. From 1.6 millimeters to 4.0 millimeters, *p* steadily decreases as the settlement progresses where the rate of decrease in *p* of M-5B is about 3 times larger than that of M-20B. In any results of M-20B and M-5B, *p* then steadily increases again as the settlement progresses, and both results appeared to be consistent. In addition, in both results of M-20B and M-5B, the ultimate load is confirmed when *S* reached about 1.6 millimeters. Such characteristics of the *p*-*S* relationship were similar to that of the *p*-*S* relationship which was derived from D-20B and D-5B. The elevation of sand surface around the model footing did not appear in any results of M-20B and M-5B. Such behavior of sand was similar to what was derived from L-20B and L-5B.

3 THE INFLUENCE OF SAND DILATANCY ON P-S RERATIONSHIPS

3.1 In the Case of Dense Sand Models

In the case of dense sand models, sand ground under the footing seemed to exhibit a continuous behavior with positive dilatancy until *p* reaches the ultimate load, whereas the sand behavior under footing exhibits a discontinuous behavior with a sign of failure surfaces after *p* reached the ultimate load. Therefore, the FEM simulation was performed until *p* reaches the ultimate load, and then the rigid-plastic analysis based on the bearing capacity of Terzaghi's theory was performed [5]. In the following, SD-20B expresses the analysis corresponding to D-20B, and SD-5B expresses the analysis corresponding to D-5B.

3.1.1 In the Case of D-20B

[Until p reaches the ultimate load]

The comparison of the load-settlement relationship obtained from D-20B and SD-20B, and "Terzaghi's bearing capacity line" is shown in Fig.4. Here, "Terzaghi's bearing capacity line" is calculated as D_f S in (1), indicating the line that linked q_u as a parameter S. In Fig.4, both *p* of SD-20B and D-20B are roughly consistent until *S* reaches about 1.0 millimeter. From 1.0 millimeter to 2.0 millimeters, *p* of SD-20B is larger than that of D-20B.

$$q_u = \alpha c N_c + \beta \gamma_1 B N_\gamma + \gamma_2 D_f N_q \qquad (1)$$

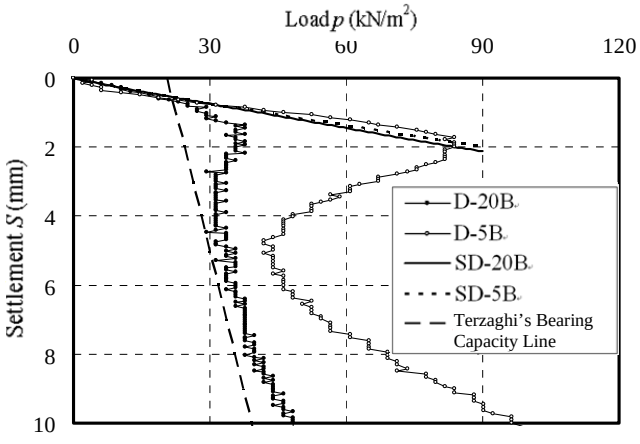

Fig.4 Comparison of the Load-settlement Relationship obtained from D-20B and SD-20B, and "Terzaghi's Bearing Capacity Line"

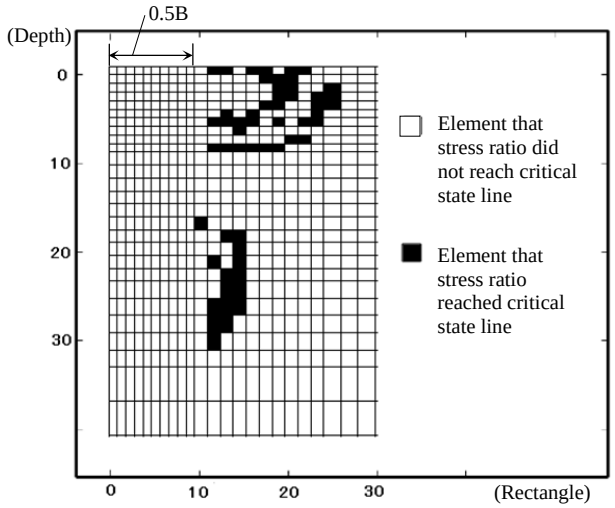

Fig.5 The Distribution of Stress Ratio obtained from SD-20B(Unit：mm)

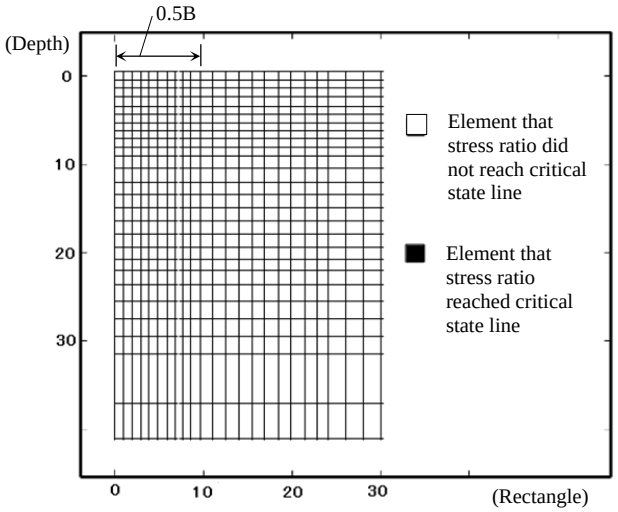

Fig.6 The Distribution of Stress Ratio obtained from SD-5B(Unit：mm)

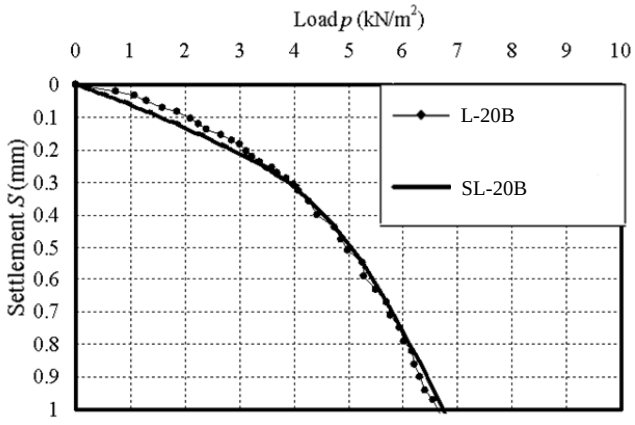

Fig.7 Comparison of the Load-settlement Relationship obtained from L-20B and SL-20B

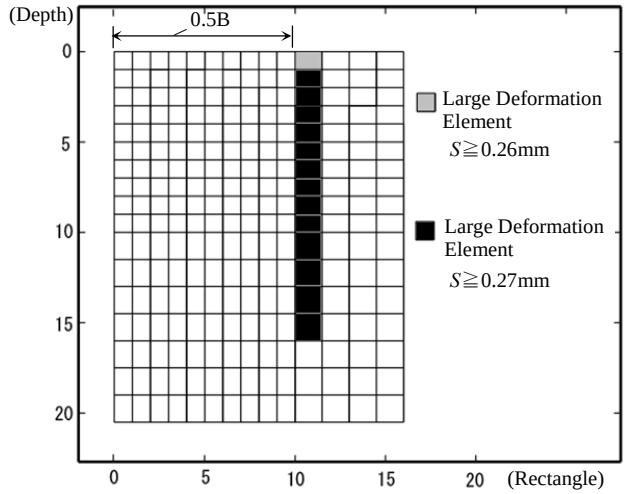

Fig.8 The Distribution of "Large Deformation Element" obtained from SL-20B (Unit：mm)

This is because the progressive failure accompanied by the generation of the failure surface occurs. It can be confirmed from Fig.5 which shows the distribution of stress ratio obtained from SD-20B when S reached about 2.0 millimeters. In addition, the element that stress ratio reached critical state line occurred first when S reached about 1.0 millimeter. In Fig.5, it is confirmed that the element that stress ratio reaching critical state line steadily increases from 1.0 millimeter to 2.0 millimeters. Therefore, because the condition that the boundary of the element changes discontinuous when stress ratio reached critical state line is not considered in the case of SD-20B, p of SD-20B is considered to be larger than that of D-20B from 1.0 millimeter to 2.0 millimeters. From the above, it is considered that sand behavior shifts from a continuous behavior based on SMP-Cam-Clay model to a discontinuous behavior accompanied by the generation of the failure surface when S reached about 1.0 millimeter, and that the sheared mass of sand appears under the footing when S reached about 2.0 millimeters.

[After p reached the ultimate load]

In Fig.4, from 2.0 millimeters to 4.5 millimeters, p decreases slightly as the settlement progresses. When S reached about 4.5 millimeters, the load-settlement relationship is asymptotic to "Terzaghi's bearing capacity line". Therefore, sand behavior is considered to result in a total failure at this stage. After S reached about 4.5 millimeters, p increases steadily along "Terzaghi's bearing capacity line" as the settlement progresses, indicating the sand behavior resulted in a continuous failure.

3.1.2 In the Case of D-5B

[Until p reaches the ultimate load]

The comparison of the load-settlement relationship obtained from D-5B and SD-5B is shown in Fig.4. Because both p of SD-5B and D-5B are roughly consistent until S reaches about 1.0 millimeter, the mechanical properties of the p-S relationship obtained from D-5B is considered to be similar to that of obtained from D-20B. From 1.0 millimeter to 2.0 millimeters, both p of SD-5B and D-5B are roughly consistent throughout. As a result, the ultimate load of D-5B is 2.4 times larger than that of D-20B. To analyze the cause, the comparative studies shown in Fig.5 and Fig.6 were conducted. Fig.6 shows the distribution of stress ratio obtained from SD-5B. In the case of SD-20B, the area recognized as sheared mass of sand appears under the footing. On the other hand, in the case of SD-5B, the area recognized as sheared mass of sand does not appear. In other words, in the case of D-5B, positive dilatancy exerts a marked binding effect of a soil tank rectangle and the dilatancy causes the increase of mean principal stress as a result. Therefore, from 1.0 millimeter to 2.0 millimeters, the ultimate load of D-5B is considered to be 2.4 times larger than that of D-20B.

[After p reached the ultimate load]

In Fig.4, from 2.0 millimeter to 4.5 millimeters, p decreases slightly until p reaches half of the ultimate load. Such characteristic of the p-S relationship is not recognized in the case of D-20B. Because the failure surface appeared at the sand surface when S reached 4.5 millimeters, the effect of positive dilatancy which occurred from 1.0 millimeter to 2.0 millimeters is considered to disappear from 2.0 millimeters to 4.5 millimeters.

3.2 In the Case of Loose Sand Models

In the case of loose sand models, shear failure which occurs and progresses below edge of the footing is considered to have a significant influence on the mechanical properties of the p-S relationship. Therefore, the element that stress ratio reached critical state line and shear strain excelled was defined as "Large deformation element", and regarded it as a gap element in each step, and the FEM simulation was performed [6]. In the following, SL-20B expresses the analysis corresponding to L-20B, and SL-5B expresses the analysis corresponding to L-5B. In addition, because both results of SL-20B and SL-5B were almost consistent, only the results of SL-20B are described as follows.

[Until p reaches the ultimate load]

The comparison of the load-settlement relationship obtained from L-20B and SL-20B is shown in Fig.7. In Fig.7, both p of SL-20B and L-20B are almost consistent until S reaches about 1.0 millimeter. To investigate the stress condition in the sand ground, the distribution of "Large deformation element" was obtained from SL-20B as shown in Fig.8. In Fig.8,

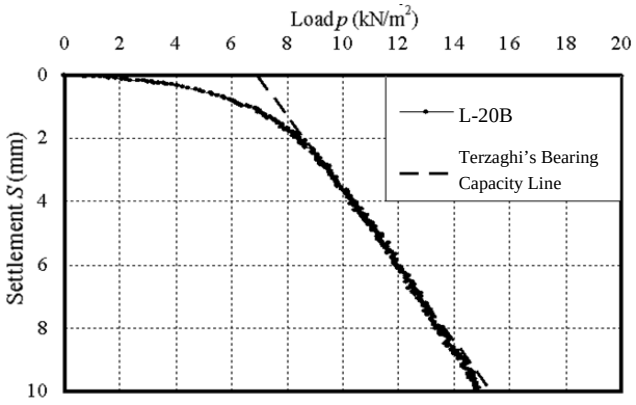

Fig.9 Comparison of the Load-settlement Relationship obtained from L-20B and "Terzaghi's Bearing Capacity Line"

Table3 Comparison of the Ultimate Load by the Relative Density

Experiment Name	The Ultimate Load (kN/m^2)	R_u
L-20B	9.51	0.96
L-5B	9.17	
M-20B	25.01	1.15
M-5B	28.70	
D-20B	35.66	2.35
D-5B	83.91	

"Large deformation element" appears below edge of the footing first when S reached 0.26 millimeters, and after S reached 0.27 millimeters, it appears directly below "Large deformation element" which occurred when S reached 0.26 millimeters. Because both p of SL-20B and L-20B are almost consistent until S reaches about 1.0 millimeter, the sand ground under the footing is considered to exhibit a behavior based on SMP-Cam-Clay model until S reaches about 0.26 millimeters. In other words, sand ground under the footing is considered to exhibit a contractile behavior with negative dilatancy. From 0.26 millimeters to 1.0 millimeters, it is considered that sand ground under the footing exhibits a contractile behavior continuously with negative dilatancy and that shear failure occurs and progresses at the same time below edge of the footing.

[After p reached the ultimate load]

In Fig.7, the p-S relationship obtained from SL-20B showed a good correspondence with that of obtained from L-20B until S reaches 1.0 millimeter. After S reached 1.0 millimeter, the simulation of the p-S relationship was carried out based on "Terzaghi's bearing capacity line," since SL-20B was difficult to perform as p of L-20B approached the ultimate load. Here, the relative density D_r was determined to be consistent with q_u when S reached 3.0 millimeters and the ultimate load of L-20B. The relationship between D_r and internal friction angle ϕ was estimated from [9]. As a result, D_r=59%, ϕ =38.9°, $\gamma_1=\gamma_2$=1.52g/cm^3 were obtained. These values correspond to the constants representing the mechanical properties of the medium-dense sand ground. The comparison of "Terzaghi's bearing capacity line" using these values and the load-settlement relationship obtained from L-20B is shown in Fig.9. In Fig.9, it was obtained the interesting results that "Terzaghi's bearing capacity line" shows a good correspondence with the p-S relationship obtained from L-20B after S reached 3.0mm millimeters.

3.3 In the Case of Medium-dense Sand Models

A comparison of the ultimate load in the case of each sand model is shown in Table3. In Table3, R_u is the ratio of the ultimate load in the case of using ℓ 5B against ℓ 20B. Some binding effect of a soil tank rectangle is recognized on R_u in the case of medium-dense sand model. A binding effect of a soil tank rectangle becomes marked by positive dilatancy as described in Section 3.1.2. Therefore, in the case of medium-dense sand model, because the condition of dilatancy occurrence is located between positive dilatancy and negative dilatancy, some binding effect of a soil tank rectangle recognized on R_u is considered to be exerted by positive dilatancy which occurred steadily as the settlement progresses.

4 CONCLUSIONS

In this paper, we present the theoretical properties of the load-settlement relationship on sand ground, which were derived from circular footing model experiment and computer simulation. To study the effect of sand dilatancy on the mechanical properties of the load-settlement relationship, the model experiment was carried out on relative density and tank dimensions as parameter. The quantitative relationship between load and settlement was analyzed through FEM simulation with SMP-Cam-Clay model, which is capable of estimating the dilatancy. The results are summarized as follows;

1) In the case of dense sand models with large soil tank (D-20B), it is considered that sand behavior shifts from a continuous behavior based on SMP-Cam-Clay model to a discontinuous behavior accompanied by the generation of the failure surface when S reached about 1.0 millimeter, and that the sheared mass of sand appears under the footing when S reached about 2.0 millimeters. When S reached about 4.5 millimeters, sand behavior is considered to result in a total failure. After S reached about 4.5 millimeters, sand behavior is considered to result in a continuous failure.
2) In the case of dense sand models with small soil tank (D-5B), until S reached about 1.0 millimeter, the mechanical properties of the p-S relationship obtained from D-5B is considered to be similar to that of obtained from D-20B. From 1.0 millimeter to 2.0 millimeters, it is considered that positive dilatancy exerts a marked binding effect of a soil tank rectangle and the dilatancy causes the increase of mean principal stress. Accordingly, the ultimate load of D-5B was 2.4 times larger than that of D-20B. From 2.0 millimeter to 4.5 millimeters, the effect of positive dilatancy which occurred from 1.0 millimeter to 2.0 millimeters is considered to disappear. When S reached about 4.5 millimeters, mechanical properties of D-5B are considered to be similar to that of D-20B.

3) In the case of loose sand models with large and small soil tank (L-20B and L-5B), sand ground under the footing is considered to exhibit a behavior based on SMP-Cam-Clay model until S reaches about 0.26 millimeters. In other words, sand ground under the footing is considered to exhibit a contractile behavior with negative dilatancy. From 0.26 millimeters to 1.0 millimeters, it is considered that sand ground under the footing exhibits a contractile behavior continuously with negative dilatancy and that shear failure occurs and progresses at the same time below edge of the footing. After S reached 3.0millimters, the results showed that, with the values correspond to the constants representing the mechanical properties of medium-dense sand ground, "Terzaghi's bearing capacity line" seemed to correspond with the p-S relationship obtained from L-20B.
4) In the case of medium-dense sand models (M-20B and M-5B), some binding effect of a soil tank rectangle was recognized on R_u which shows the ratio of the ultimate load in the case of using ℓ 5B against ℓ 20B. This is considered to be exerted by positive dilatancy which occurred steadily as the settlement progresses, because the condition of dilatancy occurrence is located between positive dilatancy and negative dilatancy.

5 REFERENCES

[1] Rei Morimoto et al, "Large-scale plane strain bearing capacity tests of shallow foundation on sand. (Part 2) ," 24th Japan National Conference of Geotechnical Engineering, 1989, pp.1243-1246

[2] K. Terzaghi, "Theoretical Soil Mechanics," John Wiley & Sons. Inc., 1963, pp118-134

[3] Vesic, A.S. "Bearing Capacity of Deep Foundations in Sand," Highway Research Record, Vol.39, 1963, pp112-153

[4] E. E. De Beer, "Experimental determination of the shape factors and the bearing capacity factors of sand, Geotechnique, Vol.20, No.4, 1970, pp387-411

[5] Yusuke Tomita et al., "Load Settlement Relationships of Circular Footings Considering Dilatancy Characteristics of Dense Sand ," Journal of Structural and Construction Engineering (Transactions of AIJ), No. 646, 2009, pp.2263-2270

[6] Yusuke Tomita et al., "Load Settlement Relationships of Circular Footings Considering Negative Dilatancy Characteristics of Loose Sand ," Journal of Structural and Construction Engineering (Transactions of AIJ), No. 661, 2011, pp.563-570

[7] Wei Li et al., "Measurement of soil Displacement around Pile Tip by Digital Image Analysis," Geotechnical Engineering in Urban Construction, Proceeding of the Sino-Japanese Symposium on Geotechnical Engineering, Beijing, China, 2003, pp.393-400

[8] Naotoshi Kashiwa et al. "Displacement Amplitude Dependence of Effect of Pile Group by Cyclic Lateral Loading Tests on Large Displacement," Journal of Structural and Construction Engineering (Transactions of AIJ), No. 614, 2007, pp.53-60

[9] Yorihiko Osaki, "Architectural Foundation Structure," gihodobooks, 1991

First International Conference on Geotechnique, Construction Materials and Environment, Mie, Japan, Nov.21-23, 2011, ISBN: 978-4-9905958-0-7 C3051

Thermally Modifying Bentonite for Construction Industry

Abdoullah Namdar, Department of Civil Engineering and Earth Resources, Universiti Malaysia Pahang

ABSTRACT – The application of geology in civil engineering make possibility of ground improvement. This paper involve with the thermally modification of construction material based on changing micro and macro characteristics. The heat could modify the soil shape, size and chemical composite as well as crystal structure. In this research work the bentonite subjected to the heat for 6 hours from 100 ºC to 500 ºC in increment of 100 ºC. The different techniques and methods have been used for changing soil micro and macro characteristics. And also the different technique validated this research investigation and the result has been shown that heat has significant affect on controlling geotechnical engineering problem. And in the final author would like suggest that the there is still more scope for continuing this research work on several natural soil and mineral in applying heat for different time and level for approaching better results.

Keyword: Soil characteristics; natural soil; ground improvement; geotechnical problem; soil atomic structure

1. INTRODUCTION

Clay has always played a major role in human life. Clay raw materials are used and their value recognized in many economic branches, agriculture, civil engineering and environmental studies. This is largely because of their wide ranging properties, high resistance to atmospheric conditions, geochemical purity, and easy access to their deposits near the earth's surface and low price.

Clay minerals, the essential constituents of argillaceous rocks, can be classified in seven groups according, to their crystal structure and crystal chemistry. Clay raw materials are divided in the same way into seven groups. An eighth group covers clay ochres and pigments. Further classification is based on the purpose-made technological application. It gives information on the application of clay raw materials or individual clay minerals: in the production of foods, feedstuffs, beverages, paper, rubber, plastics, artificial leather, protective coatings for interior and exterior use, pharmaceutics, cosmetics, paints, pencils, pastels, porcelain, etc [1]. There are many tests have been performed on bentonite for simulating compaction and densities. It is heated on one end while hydration with deionised water takes place by the opposite end to simulate the thermal gradient created by the heat generated by the radionuclide decay and the hydraulic gradient generated by the groundwater coming from the host rock into the bentonite barrier [2-3]. It has been considered the engineering behavior of bentonite enhanced sand (BES) mixtures in relation to their performance as environmental barriers. Data on the swelling and hydraulic conductivity are presented. At low effective stresses the bentonite within BES mixtures swells sufficiently to separate the sand particles. In such states two factors affect the void ratio reached by the bentonite after swelling: the ionic concentration of the pore solution and the bentonite fabric after compaction. Bentonite swelling is very sensitive to the pore solution concentration because increasing concentration suppresses the diffuse double layer component of swelling. Remoulding during compaction can result in a slight reduction in bentonite swelling, probably because of disruption to the cluster-based fabric of bentonite. At high effective stresses the bentonite has insufficient swelling capacity to force the sand particles apart, and the sand pore volume thus limits swelling [4]. Bentonite enhanced sand (BES) mixtures are widely used as barriers to control the movement of liquid from waste disposal facilities because BES can combine relatively high strength and low compressibility with very low hydraulic conductivity. This is achieved by using a mixture that contains sufficient sand to ensure the stability of the compacted mixture and enough bentonite to seal the voids between the sand particles. Other benefits are that compacted BES containing modest amounts of bentonite is fairly resistant to the effects of desiccation, and the bentonite in BES has a high chemical buffering capacity [5-6].

It has been reported on GMZ bentonite as a potential material for the construction of engineered barrier in the Chinese program of geological nuclear waste disposal, for its high montmorillonite content, high cation exchange capacity (CEC) and large specific surface etc. Studies on mineralogy and chemical composition, mechanical properties, hydraulic behavior, swelling behavior, thermal conductivity, microstructure and volume change behavior of GMZ bentonite were performed from 1980s. Based on a review of the former studies, achievements on experimental and theoretic results obtained on compacted GMZ bentonite specimens including basic properties, thermal, hydraulic and mechanical behaviors are presented. Results show the thermal conductivity of GMZ bentonite and the bentonite based mixtures influenced by its dry density, water content, mixture of other materials and degree of saturation etc. Water retention capacity of highly compacted GMZ bentonite decreases as the temperature increases under confined and unconfined conditions. The hysteretic behavior in the water retention curves of the compacted GMZ bentonite is not so significant at 20 or 40 °C. The unsaturated hydraulic conductivity of compacted GMZ bentonite under unconfined conditions is higher than that of under confined conditions. This is possibly induced by the difference in the mechanism of micro-structural changes during hydration under different confining conditions. The compaction curves for GMZ bentonite with different dry densities are clearly step phased. And the optimum water content for GMZ bentonite is about 15%. An exponential relationship between swelling pressure and dry density of highly compacted GMZ bentonite was determined for the prediction of swelling pressure. Furthermore, the void ratio after swelling for unconfined sample also can be predicted using diffuse double layer (DDL) theory [7]. Conceptually the design of high-level radioactive waste (HLW) repositories in deep geological media includes the construction of an engineered barrier around the waste containers constituted by a buffer backfill material [8].

The purpose of the entire this research exercise would be (i) identification under heat bentonite morphology and mechanical properties (ii) and modify bentonite characteristic for innovation of new material could be use for mitigation of geotechnical and geo-environment problems.

2. METHODOLOGY AND EXPERIMENTS

To innovation a new construction material for solving geotechnical and geo-environment problems an investigation on thermally treated bentonite has been executed. The bentonite has been submitted to the heat for 6 hours from 100 ºC to 500 ºC in increment of 100 ºC. The main research attempt was to modifying construction material under laboratory condition. The evaluation of both for the macro and micro of bentonite characteristics based on new research work and previous investigation have been taken systematically trough of laboratory testing. And in the laboratory triaxial, XRF and SEM tests have been conducted.

3. RESULTS AND DISCUSSION

The heat has been affected on soil mechanical behavior based on soil crystal structure and chemical composite and had significant affect on soil mechanical properties in macro and micro scale. In this investigation has been observed that the heat strongly changed soil mechanical properties. From the previous investigation in the table 1 is indicated unit weight, optimum moisture content and natural moisture content of bentonite.

Table. 1 the bentonite mechanical properties [9]

Heat ºC	γ kN/m^3)	OMC (%)	NMC (%)
RT	12.1	42.4	13.43
100	12.2	42.5	9.46
200	12.3	42.77	8.9
300	12.1	42.3	5.3
400	11.6	39.2	2.53
500	11.5	38.8	2.33

Table. 2 the bentonite mechanical properties

Heat ºC	γ (KN/m^3)	C (KN/m^2)	Φ [◦]
RT	12.1	38	0
100	12.2	48	0
200	12.3	56	5
300	12.1	70	10
400	11.6	84	3
500	11.5	98	12

From this research work some other mechanical properties of bentonite has been mentioned in the table 2. The heat is playing in reducing bentonite unit weight and the interesting issue is the bentonite cohesive characteristic is increased linearly and from other hand the internal angle of friction is changing nonlinearly. In overall it is find that the bentonite with new characteristic is with less weight and more bearing capacity. The changing bentonite crystal structure due to heat resulted in improved permeability. It could be suggested that for increasing waterproof of soil foundation thermally treated bentonite could be acceptable material. The soil mechanics experiment result has been shown that the best safe bearing capacity appeared when soil is subjected to 500 ºC heat, and the decreasing unit weight in this level has not affected on final result compare to when bentonite is under less heat level. In the room temperature bentonite has 700.06 kN/m^2 safe bearing capacity, when it is submitted to the heat for 500 ºC has been improved up to 3132.90 kN/m^2, it was understood that the application of heat on soils could helps in modification of construction material for improving earth structure stability and impermeability, and also could used in other industry. The fig 1 is stress-strain relationship of bentonite from triaxial test and the fig 2 is [9] also stress-strain relationship of bentonite from compression tests when subjected to different level of heat. The results of both methods are almost close to each other. When the heat is increased the stress-strain relationship increased but not linear and always increasing of heat not resulted in improving soil bearing capacity in this regard could bring example of bentonite is submitted to the 400 ºC. This investigation was for applying heat on the bentonite up to 500 ºC and has also been limited for 6 hours. For the future investigation could be extend the heat time and level in applying on bentonite, or other material for approaching better or optimizing result. For evaluation of changing bentonite mechanical properties subjected to the heat the chemical element and the morphology of the bentonite have also been investigated.

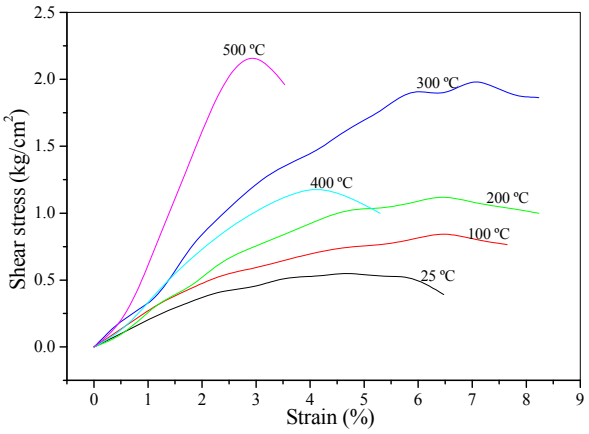

Fig 1 shear stress Vs strain in bentonite clay

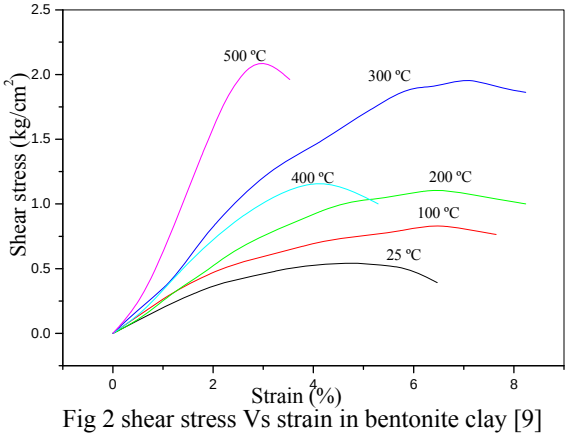

Fig 2 shear stress Vs strain in bentonite clay [9]

Table. 3 Chemical element of the bentonite in different level of heat

Heat ºC		O	Mg	Al	Si
25	Wt %	40.71	0.89	8.42	26.97
	At %	59.18	0.85	7.25	22.33
100	Wt %	40.91	-	8.34	26.79
	At %	59.68	-	7.22	22.27
200	Wt %	43.09	-	8.57	27.26
	At %	61.27	-	7.23	22.09
300	Wt %	36.29	-	8.05	28.17
	At %	55.41	-	7.28	24.50
400	Wt %	40.06	-	8.44	27.98
	At %	58.72	-	7.33	23.36
500	Wt %	39.65	-	9.21	27.67
	At %	58.29	-	8.03	23.17

Table continued

C	K	Ti	V	Fe
1.12	1.90	2.68	0.48	16.84
0.73	1.13	1.30	0.22	7.01
1.09	1.95	2.97	-	17.95
0.71	1.16	1.45	-	7.50
1.14	2.11	2.82	-	15.01
0.73	1.22	1.34	-	6.12
0.82	1.95	3.03	-	21.69
0.56	1.22	1.54	-	9.49
0.93	1.73	2.50	-	18.36
0.62	1.04	1.22	-	7.71
0.50	1.91	2.27	-	18.79
0.33	1.15	1.11	-	7.91

The table 3 indicated the chemical composite of the bentonite subjected to the heat from 100 ºC to 500 ºC in increment of 100 ºC, and the XRF chemical analysis experiment has been indicated that the Mg and V of the bentonite have been disappeared after applying 100 ºC heat, and the from other hand the remaining elements which are O, Al, C, K, Ti, Si, Fe showing different level in changing heat level, and could be understand that the chemical elements are not responsible for changing soil mechanical properties.

The SEM photographs have clearly revealed that the surface morphology, shape and size of the minerals (figs 3-8). The bentonite under heat for 6 hours from 100 ºC to 500 ºC in increment of 100 ºC selected to study its morphology modification, the result shown that under all conditions results are closely similar (fig 3-8) and also same result is observed about soil chemical composite from the XRF experiment (table 3) it could be expected that the soil crystal structure is main reason in modification of soil mechanical properties. It is observed different color of bentonite at any level of heat is applied. The changing bentonite color during increasing heat is due to modification of crystal structure of bentonite.

It is to be noted that innovation of the better construction material is possible by application of the heat on bentonite. It is interesting to be mention that in the bentonite submitted to the heat for 500 ºC after return to room temperature when mixed with the water to carry out of compaction test the small hydration has been observed. It is due to developed new bentonite characteristic based on changing crystal structure. The modification of crystal structure was responsible for improving bentonite mechanical properties.

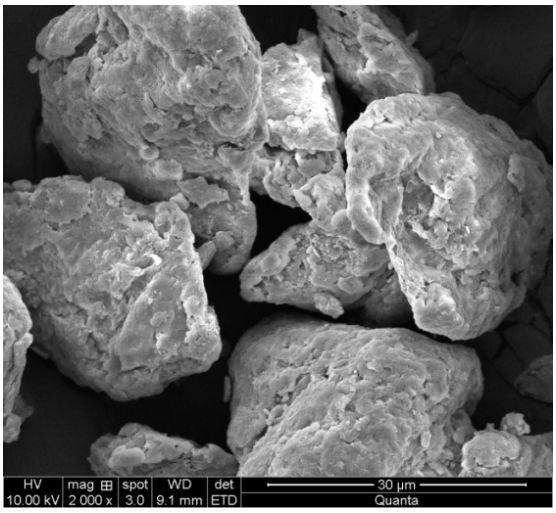

fig. 3 SEM Photo of bentonite at 25 ºC

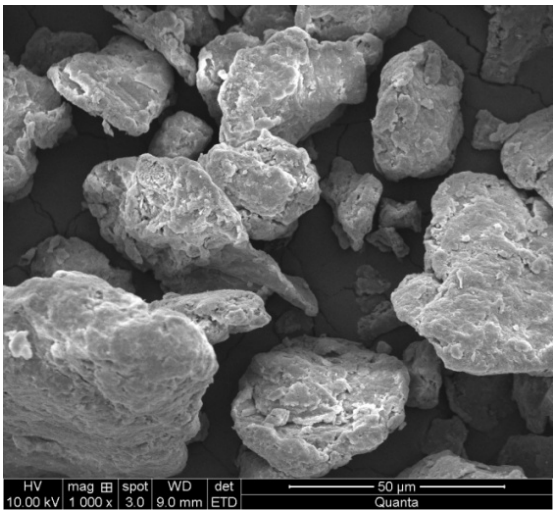

Fig. 4 SEM Photo of bentonite processed under 100 ºC for six hours

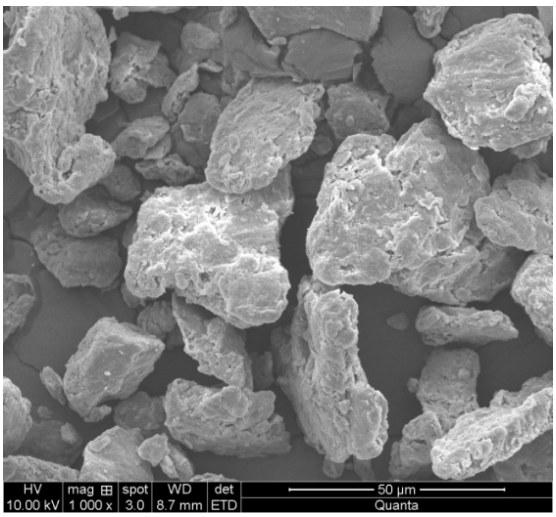

Fig. 5 SEM Photo of bentonite processed under 200 ºC for six hours

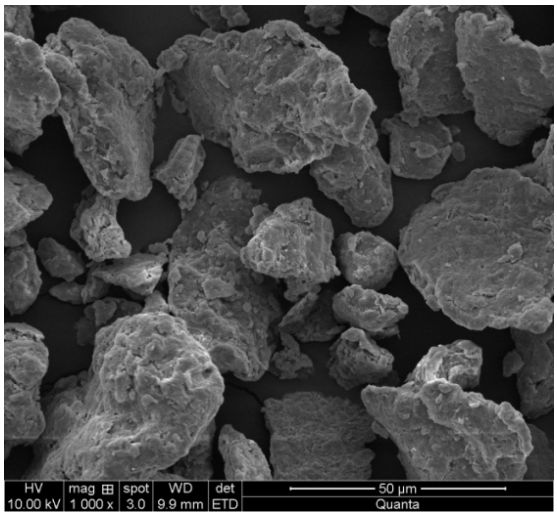

Fig. 6 SEM Photo of bentonite processed under 300 ºC for six hours

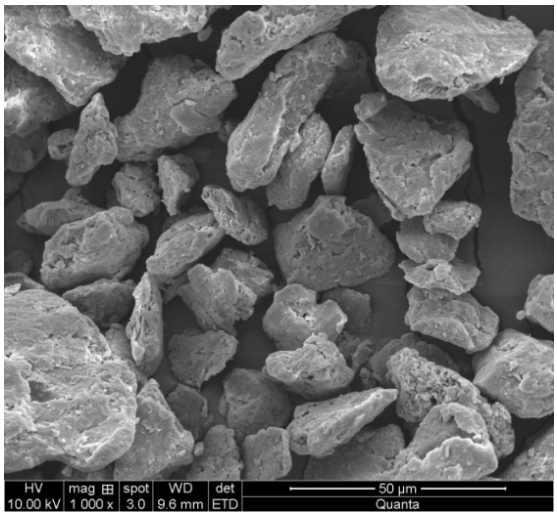

Fig. 7 SEM Photo of bentonite processed under 400 ºC for six hours

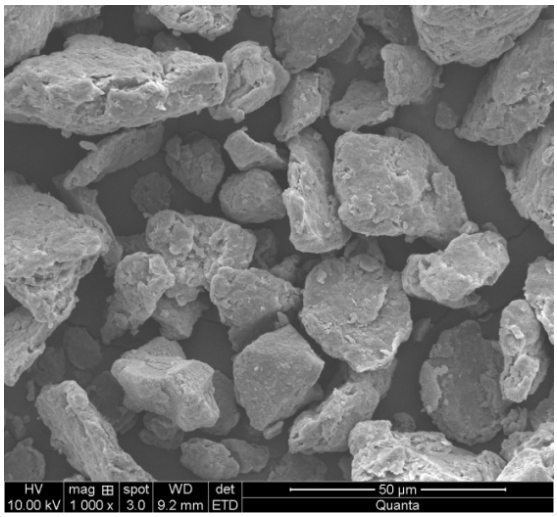

Fig. 8 SEM Photo of bentonite processed under 500 ºC for six hours

4. CONCLUSION

- The validation of the results have been proved by comparing different results
- The bentonite crystal structure was responsible for soil mechanical properties modification
- It could be suggested this method can apply for improving construction material characteristic.
- There is different material could be investigated in applying heat for different time and level for approaching better results

5. ACKNOWLEDGEMENTS

The author would like to express his thanks to faculty of civil engineering, SJCE, Mysore, India, and faculty of earth science of University of Mysore, India for timely guidance.

6. REFERENCES

[1]. Ji i Konta, Clay and man: clay raw materials in the service of man , Applied Clay Science, 10, (4), (1995), pp 275-335.

[2]. Martín, M., Cuevas, J., Leguey, S., 2000. Diffusion of soluble salts under a temperature gradient after the hydration of compacted bentonite. Applied Clay Science 17, 55–70.

[3]. Villar, M.V., Sánchez, M., Gens, A., 2008b. Behaviour of a bentonite barrier in the laboratory: experimental results up to 8 years and numerical simulation. Physics and Chemistry of the Earth 33 (Supplement 1), S476–S485.

[4]. D.I. Stewart, P.G. Studdsb, T.W. Cousens, The factors controlling the engineering properties of bentonite-enhanced sand, Applied Clay Science 23 (2003) 97 – 110.

[5]. Tay, Y.Y., Stewart, D.I., Cousens, T.W., 2001. Shrinkage and desiccation cracking in bentonite – sand landfill liners. Engineering Geology 60, 263 – 274.

[6]. Yong, R.N., 1999a. Soil suction and soil – water potentials in swelling clays in engineered clay barriers. Engineering Geology 54, 3 – 13.

[7]. Wei-Min Ye, Advances on the knowledge of the buffer/backfill properties of heavily-compacted GMZ bentonite, Engineering Geology 116 (2010) 12-20.

[8]. Villar, M.V., Lloret, A. 2008. Influence of dry density and water content on the swelling of a compacted bentonite. Applied Clay Science 39, 38–49.

[9]. Abdoullah Namdar, et al (2011), Bentonite Thermal Behavior in Geotechnical Engineering, Annals of faculty engineering Hunedoara, International Journal Of Engineering, Tome IX, Fascicule 1

7. NOMENCLATURE

Φ (Degree)	= Angle of Friction
C (KN/m^2)	= Cohesive of Soil
OMC (%)	= Optimum Moisture Content
SBC (KN/m^2)	= Safe Bearing Capacity
γ (KN/m^3)	= Unit Weight
NMC (%)	= Natural Moisture Content

First International Conference on Geotechnique, Construction Materials and Environment, Mie, Japan, Nov.21-23, 2011, ISBN: 978-4-9905958-0-7 C3051

Mesh-Free Analysis of Beam on Elastic Foundation

S. M. Binesh, Department of Civil and Environmental Engineering, Shiraz University of Technology, Shiraz, Iran

ABSTRACT: The concept of beam on elastic foundation has been extensively used by geotechnical engineers for foundation design and analysis. However most of the studies on the analysis of beam on elastic foundation are devoted to the mesh based methods. In this paper a mesh-free method is implemented for the analysis of beam on two parameter elastic foundation. The geometry of the problem is modeled by nodes and the displacement field is constructed by radial basis functions. The final system of equations is derived by the substitution of the displacement field into the weak form of the governing equation. The elastic foundation is simulated by the concept of linkage element and there is no need of node or element in the traditional sense. At the end of the paper the results of analysis with the mesh-free method are compared with the results of the finite element analysis.

Keywords: Mesh-Free, Beam, Elastic Foundation

1. INTRODUCTION

There are many geotechnical engineering problems that can be idealized as beams on elastic foundations. This kind of modelling helps to understand the soil-structure interaction phenomenon and predict the contact pressure distribution and deformation within the medium. The most common theory for the beam on elastic foundation modelling is the Winkler approach [1]. However the modelling of soil using the Winkler's theory was considered inadequate in the handling of various problems. The main weakness lies in the fact that it overlooks the shear interaction between the spring elements. Hence the two-parameter models were proposed some decades ago [2-3]. The numerical solution for these two-parameter models are mainly obtained by mesh based methods such as finite element or finite difference method [4].

In this paper a mesh-free method is implemented for the analysis of beam on two-parameter elastic foundation. In the proposed approach the geometry of the beam is modelled by nodes and the displacement field is constructed by radial basis functions. The two-parameter foundation is simulated by a virtual layer consists of two sets of springs with different stiffness coefficients. At the end of the paper the results of analysis with the mesh-free method are compared with the results of the finite element analysis.

2. MESH-FREE METHODS

A new family of numerical methods is developed to get rid of the deficiencies related to mesh definition. These methods are globally coined as mesh-free or mesh-less methods and their main characteristic is their independency to the traditional mesh definition. There are many mesh-free methods such as smoothed particle hydrodynamics (SPH) [5], element free Galerkin method (EFGM) [6], reproducing kernel particle method (RKPM) [7], etc. In this paper the radial basis point interpolation method (RPIM) is used for the analysis of beam on elastic foundation.

2.1 Enriched RPIM

According to the enriched RPIM A field function u(x) can be approximated using both radial and polynomial basis as

$$u(\mathbf{x}) = \sum_{i}^{n} R_i(\mathbf{x}) a_i + \sum_{j}^{m} P_j(\mathbf{x}) b_j = \mathbf{R}^T(\mathbf{x})\mathbf{a} + \mathbf{P}^T(\mathbf{x})\mathbf{b} \qquad (1)$$

where $\mathbf{R}(\mathbf{x})$ and $\mathbf{P}(\mathbf{x})$ are, respectively, the vector of radial and polynomial basis and n is the number of field nodes in the local support domain for point $\mathbf{x}$. Vectors $\mathbf{a}$ and $\mathbf{b}$ are coefficients for $\mathbf{R}(\mathbf{x})$ and $\mathbf{P}(\mathbf{x})$ respectively .

The coefficient vectors $\mathbf{a}$ and $\mathbf{b}$ are determined by enforcing Eq. (1) to be satisfied at all the n nodes within the local support domain. Hence, Eq. (1) can be written as:

$$u(\mathbf{x}) = \mathbf{\Phi}(\mathbf{x})\mathbf{U}_s \qquad (2)$$

where $\mathbf{U}_s$ is a vector of nodal displacements, and $\mathbf{\Phi}(\mathbf{x})$ contains RPIM shape functions for the n local nodes in the support domain. For details the reader is referred to [8].

3. BEAM ON ELASTIC FOUNDATION MODELING

3.1 Beam Modeling

In the present approach, a beam with any arbitrary thickness can be simulated readily. As shown in Fig. 1 two or more parallel sets of nodes may be used to model the beam structure. Considering the variational (weak) form of the total potential energy functional for the beam, the discrete form of equations in mesh-free approach can be written as

$$\mathbf{K}_\mathbf{B}\mathbf{U}_\mathbf{B} = \mathbf{F}_\mathbf{B} \qquad (3)$$

where

$$\mathbf{K}_\mathbf{B} = \iint_\Omega \mathbf{B}_\mathbf{B}{}^T \mathbf{D}_\mathbf{B} \mathbf{B}_\mathbf{B}\, d\Omega \qquad (4)$$

$$\mathbf{F}_\mathbf{B} = \iint_\Omega \mathbf{\Phi}_\mathbf{B}{}^T \mathbf{b}\, d\Omega + \int_\Gamma \mathbf{\Phi}_\mathbf{B}{}^T \overline{\mathbf{T}}\, d\Gamma \qquad (5)$$

where $\mathbf{\Phi}$ and $\mathbf{B}$ are respectively, the shape functions and the gradient of shape functions matrices, $\mathbf{b}$ is the body force vector, $\mathbf{D}$ is the material matrix, Ω is the problem domain, $\overline{\mathbf{T}}$ is the prescribed surface traction and Γ is the boundary along which the surface traction is imposed. It should be noted that

subscript B stands for the beam media.

3.2 Elastic Foundation Modeling

In order to simulate the elastic foundation, the concept of linkage element is used [9]. As shown in Fig. 2 the two-parameter foundation can be considered as a layer with two stiffness coefficients along two orthogonal directions (i.e. K_S and K_n). According to Fig. 2, the relative deformation vector δ at point P between the top and bottom surfaces can be related to the displacements of points A and B. Hence it can be written as

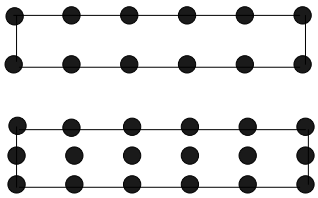

Fig. 1 Mesh-free modeling of beam media

$$\boldsymbol{\delta} = \begin{bmatrix} \delta_S \\ \delta_n \end{bmatrix} = \overline{\boldsymbol{U}}_A - \overline{\boldsymbol{U}}_B = \begin{bmatrix} u_A - u_B \\ v_A - v_B \end{bmatrix} \tag{6}$$

where δ_S and δ_n are respectively, the shear and normal relative displacement at point P. $\overline{\boldsymbol{U}}_A$ and $\overline{\boldsymbol{U}}_B$ are the displacement vectors in the local coordinate n-s at points A and B respectively. However, as the location of point B is fixed, the displacement components of $\overline{\boldsymbol{U}}_B$ (i.e. u_B and v_B) are both zero. Then equation (6) can be re-written as

$$\boldsymbol{\delta} = \begin{bmatrix} \delta_S \\ \delta_n \end{bmatrix} = \overline{\boldsymbol{U}}_A = \begin{bmatrix} u_A \\ v_A \end{bmatrix} \tag{7}$$

where u_A and v_A are respectively, the displacement of point A in the s and n directions.

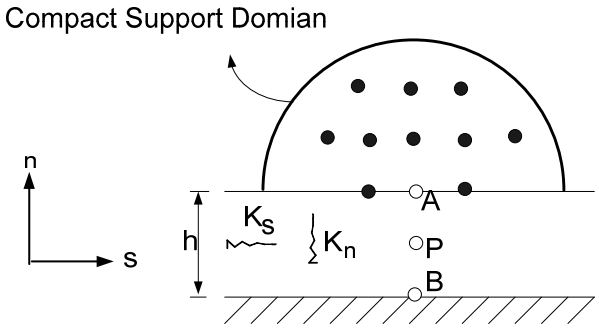

Fig. 2 Foundation modeling by linkage element concept

Considering the relation between local and global coordinate, we have

$$\overline{\boldsymbol{U}}_A = \boldsymbol{L}\boldsymbol{U}_A \tag{8}$$

where $\boldsymbol{L}$ is coordinate transform matrix and $\boldsymbol{U}_A$ is the displacement vector of point A in global coordinate.

As shown in Fig. 2 the field variable (i.e. displacement) at point A can be estimated by its nodal values at the nodes located in the compact support domain of point A. According to Eqs. (2) , (7) and (8) the displacement of point A can be written as

$$\boldsymbol{\delta} = \boldsymbol{B}_f \boldsymbol{U}_{SA} \tag{9}$$

where $\boldsymbol{U}_{SA}$ is the displacement vector composed of displacement at all nodes in the compact support domain of point A and

$$\boldsymbol{B}_f = \boldsymbol{L}\boldsymbol{\Phi} \tag{10}$$

Neglecting the normal strain component in the s direction, the strain vector in the local coordinate can be defined as

$$\boldsymbol{\varepsilon} = \frac{1}{h}\boldsymbol{\delta} \tag{11}$$

where h is the virtual thickness assumed for the foundation layer and $\boldsymbol{\varepsilon} = \begin{bmatrix} \gamma_{ns} & \varepsilon_n \end{bmatrix}^T$, in which ε_n is the normal strain in the n direction, and γ_{ns} is the shear strain. By substituting Eq. (11) into Eq. (9) the relation between strain and nodal displacement can be obtained as

$$\boldsymbol{\varepsilon} = \frac{1}{h}\boldsymbol{B}_f \boldsymbol{U}_{SA} \tag{12}$$

To evaluate the stiffness matrix related to the elastic foundation, the relation between stress and strain in this region is also needed. According to Fig. 2 the relation between stress vector and relative deformation can be written as

$$\boldsymbol{\sigma} = \boldsymbol{D}_f \boldsymbol{\delta} \tag{13}$$

where the stress vector $\boldsymbol{\sigma}$ consists of the normal stress σ_n and the tangential stress τ in the foundation region.

$$\boldsymbol{\sigma} = \begin{bmatrix} \tau & \sigma_n \end{bmatrix}^T \tag{14}$$

Matrix $\boldsymbol{D}_f$ can also be defined as

$$\boldsymbol{D}_f = \begin{bmatrix} K_S & 0 \\ 0 & K_n \end{bmatrix} \tag{15}$$

Substituting (11) into (12) gives

$$\boldsymbol{\sigma} = \frac{1}{h}\boldsymbol{D}_f \boldsymbol{\varepsilon} \tag{16}$$

Using the variational principle the stiffness matrix of elastic foundation can be written as

$$\boldsymbol{K}_{\mathrm{f}} = \int_A \left(\frac{1}{\mathrm{h}}\boldsymbol{B}_f\right)\left(h\boldsymbol{D}_f\right)\left(\frac{1}{h}\boldsymbol{B}_f\right) dA \tag{17}$$

Assuming constant virtual thickness for foundation layer, Eq. (17) can be written as

$$\boldsymbol{K}_{\mathrm{f}} = \int_\beta \boldsymbol{B}_f \boldsymbol{D}_f \boldsymbol{B}_f \, d\beta \tag{18}$$

where β is the length parameter along the foundation layer. The final matrix form of equations for the whole system of beam on elastic foundation can be written as

$$\left[\boldsymbol{K}_B + \boldsymbol{K}_f\right]\boldsymbol{U} = \boldsymbol{F} \tag{19}$$

where $\boldsymbol{U}$ and $\boldsymbol{F}$ are nodal displacement and nodal force respectively.

4. NUMERICAL STUDY

A typical example is investigated to verify the efficiency of proposed method in this paper. As shown in Fig. 3, a beam with 10 m length and 1 m thickness is assumed. The elastic modulus and Poisson ratio of the beam material are 2 GPa and 0.25 respectively. The normal and shear stiffness modulus are respectively, 15000 and 10000 kN/m^3. Plane strain condition is assumed. Two 500 kN concentrated loads are exerted in a symmetric manner at 2 m distance from each end.

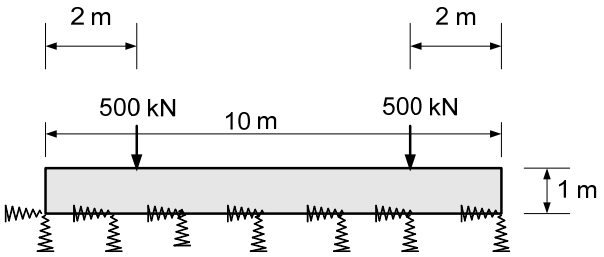

Fig. 3 Typical problem of beam on two parameter elastic foundation

The problem is solved by the finite element program SIGMAW as well as the proposed mesh-free method. The finite element modelling consists of two models; 10 elements model and 40 elements model (Fig. 4). It is obvious that by increasing the number of elements the accuracy of results will also increase. Hence this can be a measure to investigate the accuracy of proposed mesh-free method. As it is depicted in Fig. 5 the mesh-free model is constructed by the same number of nodes as the 10 elements finite element model. The results of analyses are shown for the upper and lower surfaces of the beam in Figs. 6 and 7. Due to the symmetry of the model only the results for one half of the beam are demonstrated. As it is obvious from the figures, the proposed mesh-free method offers acceptable results that are even more accurate than the results of finite element analysis with the same order of nodes.

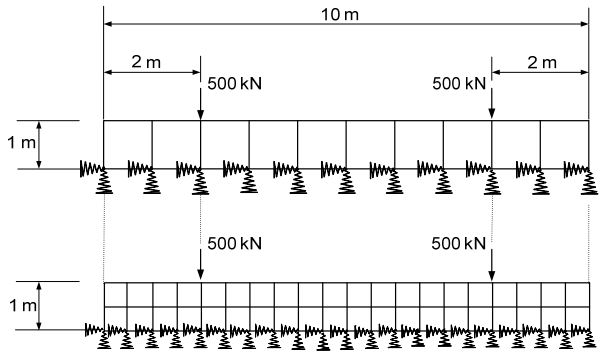

Fig. 4 Finite element models of beam on two parameter elastic foundation using 10 and 40 elements

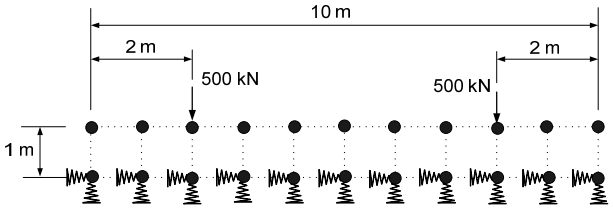

Fig. 5 Mesh-free model for the beam on two parameter elastic foundation

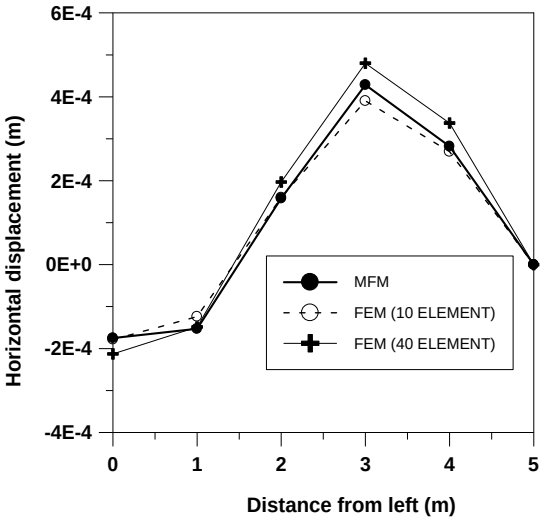

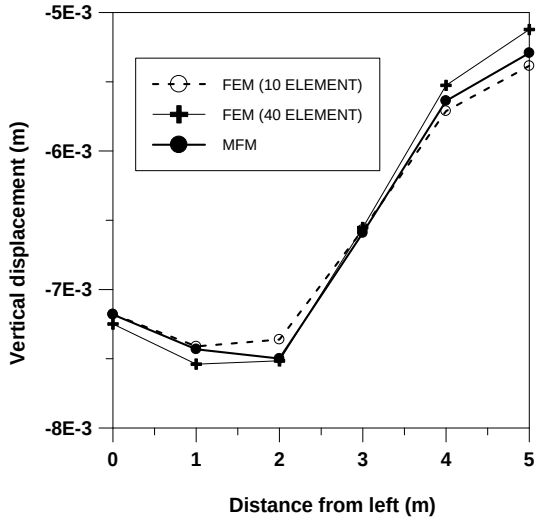

Fig. 6 Horizontal and vertical displacement of the nodes located at the lower edge of the beam

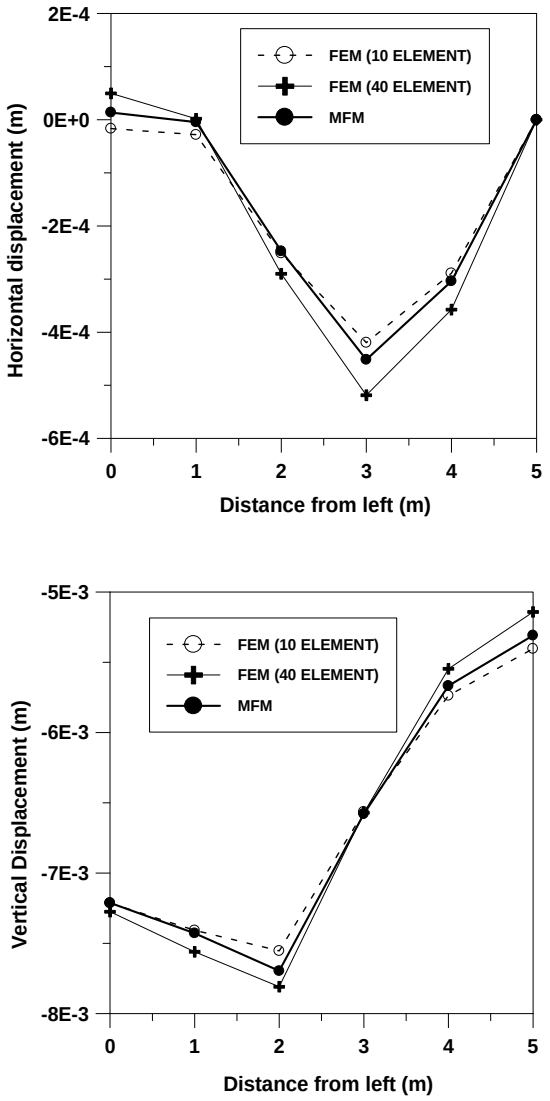

Fig. 7 Horizontal and vertical displacement of the nodes located at the upper edge of the beam

5. CONCLUSION

A mesh-free procedure is implemented for the analysis of beam on two parameter elastic foundation. The elastic foundation is simulated by the linkage element concept and there is no need of node or element in the traditional sense. The thickness of the beam can be readily adjusted and the nodes can be added or omitted easily. Besides all these benefits, the accuracy of results is also acceptable and they are even better than the finite element results with the same order of nodes.

6. REFERENCES

[1] Winkler E., in: Die Lehre von der Elastizitat und Festigkeit, Domonicus, Prague, 1867

[2] Pasternak P.L., "On a new method of analysis of an elastic foundation by means of two foundations constants", (in Russian), Gasudarstvennoe Izdatelstvo Literaturi po Stroitelstvui Arkhitekture, Moscow, USSR, 1954.

[3] Pronk A.C., "The Pasternak foundation- An attractive alternative for the Winkler foundation", Proc. of the 5th Int. Conf. on concrete pavement design and rehabilitation, Purdue Univ. West Lafayette, Indiana, 1993, Vol. 1.

[4] Bowles J.E., Foundation analysis and design, 5th edition, The McGraw-Hill Companies, Inc., 1996, Ch. 9.

[5] Libersky L.D., Petschek A.G., "Smoothed particle hydrodynamics with strength of materials", Proc. of The Next Free Lagrange Conf., 1991, PP. 248-257.

[6] Belytschko T., Lu Y.Y., Gu L., "Element-free Galerkin methods", International Journal for Numerical Methods in Engineering, 1994, Vol.37, PP.229-256.

[7] Liu W.K., Jun S., Zhang Y.F., "Reproducing kernel particle methods", International Journal for Numerical Methods in Fluids, 1995, Vol.20, PP.1081-1106.

[8] Liu, G.R., Meshfree Methods: Moving Beyond the Finite Element Method, CRC Press, Boca, 2003, Ch. 8.

[9] Herrmann L.R., "Finite element analysis of contact problems", ASCE, Journal of Engineering Mechanics Division, 1978, Vol. 104, No. 5, PP. 1043-1057

First International Conference on Geotechnique, Construction Materials and Environment, Mie, Japan, Nov.21-23, 2011, ISBN: 978-4-9905958-0-7 C3051

Frictional Performance of Infilled I-Blocks with Geosynthetic Inclusions

Faisal Hj Ali, Department of Civil Engineering, National Defense University of Malaysia

Md. Zahidul Islam Bhuiyan*, Department of Civil Engineering, University of Malaya

Firas A. Salman, Department of Civil Engineering, University of Malaya

Siau Lian Sang, Managing Director, Soil & Slope Sdn. Bhd.

ABSTRACT: Geosynthetic reinforced segmental retaining walls (GR-SRWs) are in a period of development and have achieved popularity all over the world. Inclusion of geosynthetic layer at the interface has great influence on interface frictional performance of segmental retaining wall units. In this investigation, three (3) types of geosynthetic reinforcements were chosen and used to find out their influences on the interface shear capacity of newly designed and locally produced precast I-blocks. A series of direct shear tests were conducted using a specially designed and fabricated direct shear apparatus to assess the frictional characteristics of the blocks with geosynthetic inclusions. The results presented in this paper report that flexible geosynthetic reinforcements perform well than stiff geosynthetics although decrease the interface shear capacity than no inclusion condition. The presence of geosynthetic layers also minimizes the localized stress concentrations at the interface.

Keywords: *geosynthetics; interface shear; segmental block; retaining wall; reinforced soil*

1. INTRODUCTION

Segmental concrete units (segmental retaining wall units) as the facing element for geosynthetic MSE (mechanically stabilized earth) walls have been frequently used worldwide for about three (3) decades [1]. They have achieved popularity due to many advantages in the fields of geotechnical engineering. In Malaysia, geotechnical engineers have been widely exercising geosynthetic reinforced segmental retaining walls (GR-SRWs) for last decades [2].

Facing stability is an important issue in the current design guidelines [3], [4] and it is related to shear and connection failures. Past research works [5], [6] reported that facing instability basically occurs due to poor connection strength and inadequate connection systems.

In GR-SRW constructions, polymer reinforcements are used to stabilize the backfill soils and facing columns. The presence of geosynthetic layers at the interface might increase or decrease the interface shear capacity of segmental concrete units [1], [7]. It depends on the flexibility of geosynthetic reinforcements as well as block's geometry.

In this investigation, three (3) types of geosynthetic reinforcements were chosen: a knitted polyester (PET) geogrid (flexible), a high density polyethylene (HDPE) geogrid (stiff), and a non-woven polyester geotextile (flexible) those which are mostly used in Malaysia for GR-SRW constructions. Plastic shear pins and natural coarse aggregate (NCA) were used to increase the interface shear capacity of the facing systems "to be published" [8]-[9]. A series of direct shear tests were executed under various normal loading conditions [3], [10]. Test results were presented in the form of shear stress-displacement relationship to compare the effect of different types of polymer reinforcements at interface. Shear capacity envelopes were also drawn using Mohr-Coulomb failure criteria to outline the angle of friction for different inclusions.

2. MATERIALS

2.1 Segmental concrete unit

"I" blocks were used as segmental concrete units in this research. "I" blocks are wet cast concrete units (G30), which have one center web and the tail/rear flange is extended beyond the web (Fig. 1). The rear flange is tapered that allows the blocks to form curve walls. The maximum tapered angle of the "I" block is 11.3 deg. "I" blocks are double open-ended units and provide a larger hexagonal hollow space in conjunction with two units, and the equivalent hole dimensions are about 450 mm in length, 280 mm in width and 300 mm in height. The infill weigh is approximately 93 to 94 kg with the aggregate of bulk density of 1527 kg/m^3.The physical and mechanical properties of the used blocks are outlined in Table 1.

2.2 Granular infill

The hollow cores between the blocks were infilled with 100% crushed limestone aggregate and lightly compacted. The maximum and nominal maximum sizes of the aggregate were 25 and 19 mm respectively. The particle size distribution of the granular infill meets ASTM standard size #57 gradations [11]. The physical properties of infill are given in Table 2.

2.3 Plastic pin

Ultrahigh molecular weight polyethylene (UHMWPE) plastic bars were used in this investigation as flexible connectors because of their toughness and flexibility. UHMWPE has also highest impact strength. The physical and mechanical properties of the plastic bars are given in Table 3.

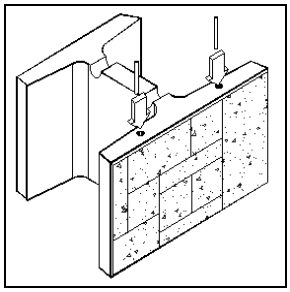

Fig. 1 Schematic of used "I" block

Table 1 Physical and mechanical properties of segmental concrete unit

Property		Value
Dimensions (WxHxL)* in mm		370x300x500
Weight (kg)		41-42
Oven dry density (g/cm^3)		2.17
Water absorption capacity	%	7.1
	g/cm^3	0.16
Moisture content (%)		3.7
Net compressive strength (MPa)		8.0

* W = Width (Toe to heel), H= Height, L= Length (Parallel to the wall face)

Table 2 Physical properties of granular infill

Property	Value
Bulk density (g/cm^3)	1.53
Specific gravity (SSD)	2.63
Void content (%)	42
Coefficient of gradation, Cc	1.15
Fineness Modulus (FM)	7.16

Table 3 Physical and mechanical properties of plastic bar

Property	Value
Yield strength at 23°C (MPa)	22
Modulus of elasticity (MPa)	750
Elongation at break (%)	>300
Notched impact strength (kJ/m^2)	No break
Density (g/cm^3)	0.94
Cross section area (mm^2)	127.66

2.4 Geosynthetic reinforcements

Three (3) different types of geosynthetic reinforcements were used in this study because of their high strength and low creep. Details of the reinforcements are referred as below:

Miragrid GX 80/30 is a knitted uniaxial geogrid prepared from high tenacity polyester yarns, and covered with a black polymeric coating. The major characteristics are good connection capacity with modular blocks and excellent interface friction behavior, and high tensile strength at low creep.

E'Grid 90R is an extruded uniaxial geogrid with elongated apertures. It is made of high density polyethylene (HDPE). The principal characteristics are good gripping capacity with the shear connectors of the modular block units and good creep performance with low strain, and high tensile strength under constant load.

Rock PEC 75 is a non woven needle punched composite geotextile consisting of combination between high tenacity polyester yarns stitched to polypropylene continuous filaments. It provides high tensile strength at low elongation and high water flow capacity in its plane.

Typical application areas of the geosynthetics (Fig. 2) are reinforcement of modular block walls, earth walls, slopes and bridge abutments. Table 4 summaries the physical and mechanical properties of the used geosynthetic reinforcements.

Fig. 2 Photographs of GX80/30, E'Grid 90R, and Rock PEC75 (left to right)

Table 4 Physical and mechanical properties of inclusions

Property		GX80/30	E'Grid 90R	Rock PEC75
Short term tensile strength T_c (KN/m)	MD	80.0	90.0	75.0
	CD	30.0	-	14.0
MD Tensile strength (KN/m)	5% strain	34.0	45.2	33.8
Strain at MD tensile strength (%)		11.0	11.5	10.0
Weight (Kg/m^2)		0.32	0.55	0.34
Aperture size (mm)	MD	23	240	-
	CD	21	16	
Thickness (mm)	Bond thickness (T_b)	1.40	4.1	2.2
	Rib thickness (T_r)		1.1	

Note: MD = machine direction; CD = Cross-machine direction. Unless noted otherwise, data are from manufacturers' literature.

3. TEST METHODOLOGY

3.1 Experimental device

A specially designed and modified large-scale apparatus was used to carry out the shear tests of the "I" blocks. A photograph of the modified test apparatus is illustrated in Fig. 3. It mainly consists of loading frame, hydraulic actuators, and a fabricated electric hydraulic pump. The vertical actuator was mounted with the loading frame using steel rollers to allow block movement during the shear test but in ASTM test protocol the vertical actuator was kept fixing [12]. The vertical and horizontal actuators were capable of applying around 45 tons of surcharge load and 130 tons of push/pull out force respectively and simultaneously. The electric hydraulic pump was connected to the actuators with pressure hoses.

A geosynthetic loading clamp was set with horizontal actuator to apply the tensile load as well as shear load. To hold the geosynthetic layer at back of the blocks, a geosynthetic gripping clamp was mounted for interface shear tests. Two (2) pressure transducers were installed over each hydraulic actuator of 150 mm stroke, and the actuators were calibrated by using load cell against the pressure transducers. Two (2) flow regulators were attached with the pump to control the rate of displacement of horizontal (shear) and vertical actuators.

The shear displacements were measured using of two 50 mm linear variable displacement transducers (LVDTs) with an accuracy of 0.001mm. Pressure transducers and LVDTs reading were continuously measured and recorded during the test by a data logger. The data were recorded at every 10 second interval.

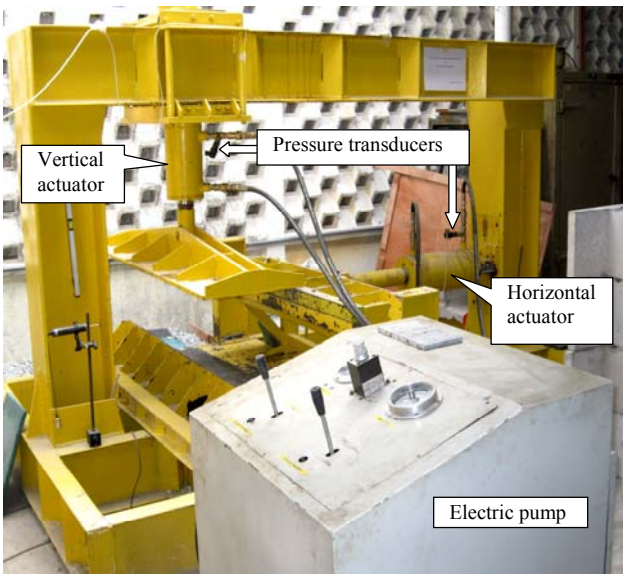

Fig. 3 Photograph of test apparatus

3.2 Interface Shear Tests

Two (2) courses of modular block units were used for interface shear tests. The bottom course consisting of two (2) "I" blocks was installed and braced laterally at the front of loading frame and the hollow space between the blocks was filled up with fresh aggregate, and lightly compacted using a steel rod. Due to tapered rear flange, a small steel plate was used at the back of the bottom course to hold the compacted aggregate. One end of the geosynthetic sample was placed over the bottom course and connected with the plastic shear pins, and then the other end of geosynthetic was gripped to the steel clamp for preventing the slippage of the reinforcement layer during the shear tests. A single "I" block was placed centrally over the running joint formed by the two underlying units to simulate the staggered construction procedure used in the field. The double open-ended space of the top block was filled up with aggregate and two (2) steel plates were used to hold the infilled aggregate of the top block. A photograph of interface shear test arrangement is shown in Fig. 4.

Normal load was imposed only over the top block through stiff rubber mat and simulated an equivalent height of the stacked blocks. The shear load was applied against the top block at a constant rate of 1 mm/min [10]. A steel plate with stiff rubber mat was used with geosynthetic loading clamp to concentrate the shearing load only over the centrally installed top block. A horizontal seating load was applied to the top block to ensure close fitting of the blocks, and after that the load and displacement devices were set to zero. The imposed seating load was 10% of maximum shear strength.
Mohr-Coulomb failure criteria were used to find out interface shear capacity at ultimate strength criterion.

$$V = N \tan\lambda + \alpha. \quad (1)$$

Where:
V = Interface shear capacity (kPa)
N = Normal stress (kPa)
λ = Angle of friction (deg.)
α = V interception (apparent cohesion)

Fig. 4 Photograph of interface shear test showing geotextile sample and gripping system

4. RESULTS AND DISCUSSION

Fig. 5 and 6 illustrate the typical curves for blocks with geosynthetic inclusions under different normal stresses. From the Figs. 5 and 6, it is also seen that the ultimate shear stresses of the infilled blocks without any geosynthetic inclusion is higher than inclusion conditions.

Among the three (3) types of inclusions, polyester geogrid (flexible) perform well than other types of geosynthetics. This is happened due to its cushion effects, which minimizes the stress concentration at interface and it also allows the aggregate interlocking through the apertures because of its grid structures. Figs 5 and 6 demonstrate that the shear stress behavior of the blocks with HDPE geogrid and polyester geotextile inclusion is quite same for both normal stresses (54 &124 kPa). Even at high normal stress the frictional performance of the blocks with HDPE geogrid inclusion is almost equal to those with polyester geotextile (Fig. 6). Due to the physical structure i.e. thickness and grid structure of HDPE geogrid, blocks can easily move over each others. HDPE geogrid works like a friction reducing layer for its grids, which are stiff and smooth. Its aperture systems also do not give better interlocking mechanism among the aggregates. On the other hand, although, the polyester geotextile provide better cushion at the block's interface but actually it interrupts the aggregates interlocking mechanism fully that reduces the frictional capacity of the blocks with geotextile inclusion.

Fig. 6 shows that the ultimate shear stress of the blocks with polyester geogrid inclusion is almost equal to those without inclusions. At high normal stress, the shear stress drop of the blocks with HDPE geogrid and polyester geotextile is more than those with polyester geogrid at low normal stress (Fig. 5).

Plots of the ultimate interface shear stress against the applied normal stress are presented in Fig. 7. It is seen that, the presence of geosynthetic inclusions reduces the ultimate interface shear capacity of the blocks. Bathurst and Simac [1], and Bathurst et al. [7] observed the same behaviors for different types of blocks with polyester geogrid inclusion. The ultimate interface shear capacity of the blocks with polyester geogrid inclusion is closer to no-inclusion condition because this flexible inclusion improves shear transfer across the block's interface than others. Fig. 7 also reports that the reduction in ultimate shear capacity for the inclusions of HDPE geogrid and polyester geotextile is higher than polyester geogrid inclusion. It is influenced by the physical structures of the used geosynthetics i.e. flexibility and grid patterns.

Table 7 summarizes performance parameters of the tested "I" block with and without geosynthetic inclusions. It is seen that the flexible geosynthetic inclusions give better angle of friction than stiff geosynthetic layer.

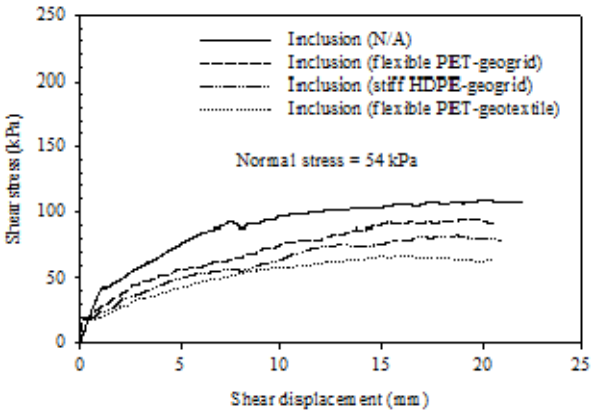

Fig. 5 Shear stress against displacement

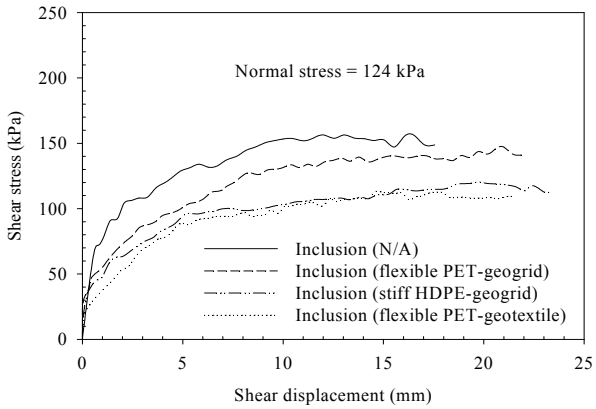

Fig. 6 Shear stress against displacement

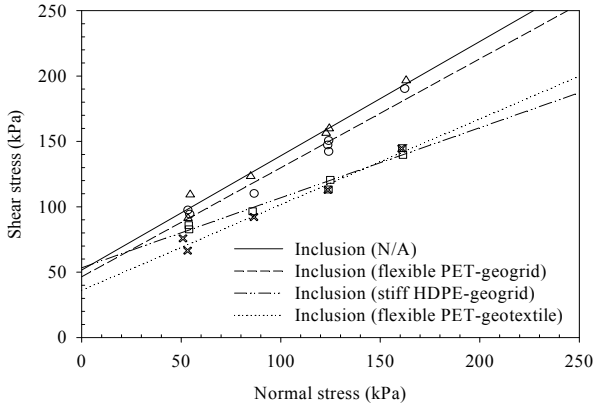

Fig. 7 Ultimate shear capacity for "I" blocks

Table 5 Interface shear parameters for different inclusion conditions

Inclusion	Angle of friction,λ (deg.)	Apparent cohesion, α (kPa)
N/A	41.2	51.6
Flexible PET-geogrid	39.8	46.4
Stiff HDPE-geogrid	28.2	53.4
Flexible PET-geotextile	33.2	36.1

5. CONCLUDING REMARKS

The presence of geosynthetic layer at the facing unit's (segmental concrete unit) interface reduces the interface shear capacity. It depends on the flexibility of the used geosynthetic samples as well as its grid patterns. The angle of friction of the blocks with polyester geogrid inclusion is higher than those with HDPE geogrid and polyester geotextile inclusions.

6. ACKNOWLEDGMENTS

The financial support for this study was provided by a grant (Fundamental Research Grant Scheme - 2010) from the Ministry of Higher Education of Malaysia awarded to the first author. Materials and technical support were provided by Soil & Slope Sdn Bhd (Malaysia).

7. REFERENCES

[1] Bathurst RJ, and Simac MR, "Geosynthetic reinforced segmental retaining wall structures in North America," in Proc. 5th Int. Conf. on Geotextiles, Geomembranes and Related Products, 1994, pp. 1-41.

[2] Lee CH, "Design and construction of a 9.6m high segmental wall," in Proc. 2nd Asian geosynthetics conference, 2000.

[3] National Concrete Masonry Association (NCMA) "Design manual for segmental retaining walls," Herndon, Virginia, 1997.

[4] Elias V, Christopher BR, and Berg RR, "Mechanically stabilized earth walls and reinforced soil slopes: Design & construction guidelines,"FHWA-NHI-00-043, Washington D.C., National Highway Institute, 2001.

[5] Bathurst RJ, and Simac MR, "Laboratory testing of modular concrete block - geogrid facing connections," in Proc. ASTM Symposium on Geosynthetic Soil Reinforcement Testing, 1993, pp. 32-48.

[6] Soong TY, and Koerner RM, "On the required connection strength of geosynthetically reinforced walls," Geotextiles and Geomembranes, vol. 15, Aug.-Dec. 1997, pp. 377- 393.

[7] Bathurst RJ, Althoff S, and Linnenbaum P, "Influence of test method on direct shear behavior of segmental retaining wall units," Geotechnical Testing Journal, vol. 31, Mar. 2008, pp. 1-9.

[8] Ali FH, Bhuiyan MZI, and Salman FA, "Effects of mechanical connectors on the interface shear capacity of segmental - concrete blocks in-filled with gravel," Int. J. of Civil Engineering and Building Materials, accepted, 2011.

[9] Bhuiyan MZI, Ali FH, and Salman FA, "Frictional behaviour of segmental retaining wall units infilled with recycled concrete aggregate," in Proc. Symposium on business, engineering and industrial applications, accepted, 2011.

[10] ASTM D 6916-03, "Standard test method for determining the shear strength between segmental concrete units," West Conshohocken, PA, USA, ASTM International.

[11] ASTM D 448-03a, "Standard classification for sizes of aggregate for road and bridge construction," West Conshohocken, PA, USA, ASTM International.

[12] ASTM D 6916-06c, "Standard test method for determining the shear strength between segmental concrete units," West Conshohocken, PA, USA, ASTM International

First International Conference on Geotechnique, Construction Materials and Environment, Mie, Japan, Nov.21-23, 2011, ISBN: 978-4-9905958-0-7 C3051

Varying Ground Water Level to Minimise Liquefaction Hazards in Urban Areas

Heitor, A.[1], Oka, F.[2], Kimoto, S.[2], Higo, Y.[2],
[1]Centre for Geomechanics and Railway Engineering, Faculty of Engineering, University of Wollongong,
[2]Dept. of Civil and Earth Resources Eng., Graduate School of Engineering, Kyoto University

ABSTRACT: During a seismic event, the occurrence of liquefaction causes severe ground deformations that compromise the structural integrity of many buried elements. Currently, there are a number of different ground improvement methods that can be adopted to treat the foundations of the newly constructed structures. However, fewer remediation methods have been developed for the treatment of the ground of already existing superstructures. This study explores the performance of a cost-effective remediation technique consisting of inducing ground water level (GWL) depth variation. A 2-D profile of a soil embankment (i.e. river levee) was selected to model the GWL variation effect on the deformations associated with the dynamic loading. The results show that the GWL located at higher depth, minimizes the overall embankment deformations and contribute to a significant reduction in the vertical displacements observed on the top of the embankment.

Keywords: Liquefaction, partially saturated ground, remediation method, GWL variation,

1. INTRODUCTION

In the event of an earthquake, the occurrence of liquefaction is often the main cause of severe ground deformations that compromise the structural integrity of many buried elements of urban superstructures, including buildings, foundation piles, and lifelines. This aspect is of paramount importance, since the vast majority of the largest cities centres in the world that are exposed to frequent seismic events, are located by the coast lines. Furthermore, due to the increasingly urban development pressure, there is a great deal of superstructures now constructed in high liquefaction susceptibility terrains that were part of earlier reclamation schemes. Currently, there are a number of different ground improvement methods that can be adopted to treat the foundations of the newly constructed structures, including soil densification, dynamic compaction or vibroflotation. However, there are few remediation methods developed for the treatment of the ground, on which already existing structures were built. In fact, a large number of old structures, currently erected in high liquefaction susceptibility areas, are without treatment against liquefaction.

The bubble injection method, proposed in [1], is an example of a current existing method for liquefaction remediation of existing structures. In general, this method consists of inducing partial saturation in the ground by injecting air bubbles, which constitutes a very attractive cost-effective liquefaction remediation technique. Conversely, in time the air bubbles will dissolve in the ground water and the recurrence interval of the treatment should be adequately studied. This is the main disadvantage of using this method, since the mechanics of air dissolution in ground water, necessary to establish the recurrence period are still not well understood.

The method proposed in this study is based on similar concept (i.e. inducing partial saturation in the ground) by artificially varying the ground water level (GWL) (i.e. by pumping water). Since the GWL is located at greater depth, the ground above the water level indirectly becomes partially saturated. And because liquefaction is less likely to occur under partially saturated conditions [2], [3], the application of this technique will likely reduce the overall deformations caused by the occurrence of liquefaction. This method has further advantages related to the supply of water, since it involves the continuous pumping of ground water to maintain the GWL at certain depth. By doing so, a steady supply of water can be guaranteed and the water extracted can be either lead to storage facilities or used for other purposes (i.e. agricultural, industrial use).

The study of the effectiveness of this technique was carried out numerically, adopting a 2-D profile of a soil embankment (i.e. river levee). Different GWL depths were superimposed in the ground profile and the effect of the GWL change on the deformations associated with the dynamic loading of 1Hz sinusoidal wave was investigated. The dynamic numerical analysis was conducted adopting a finite element code LIQCA-2D-SF, in which both saturated and partially saturated soil theoretical frameworks were included.

2 ELASTO-PLASTIC SIMPLIFIED MODEL FOR PARTIALLY SATURATED GROUND

The governing equations for gas-fluid-soil coupled problem can be derived from Biot's type theory of water saturated porous media based on the continuum mechanics. Herein, the compressibility of the air is assumed to be very high, or in other words, the three-phase analysis can be simplified into the soil-water coupled two-phase mixture theory [4], [5]. An elasto-plastic model with the effect of suction has been applied to the unsaturated soil using the skeleton stress concept expressed in (1) as follows,

$$\sigma'_{ij} = \sigma_{ij} - \left\{ S_r p^f \delta_{ij} + (1 - S_r) p^a \delta_{ij} \right\} \quad (1)$$

where S_r is degree of saturation, p^f and p^a are the pore water and pore air pressure, respectively and δ_{ij} is the Kronecker's delta.

In the present model the collapse behaviour is described by the shrinkage of the over consolidation boundary surface due to the decrease in suction, as shown in (2) and (3), as below:

$$f_b = \overline{\eta}^*_{(0)} + M_m^* \ln \frac{\sigma'_m}{\sigma'_{mb}} = 0 \quad (2)$$

where σ'_m is the mean effective stress, M^*_m is the stress ratio value at phase transformation, $\overline{\eta}^*_{(0)}$ is the relative stress ratio and σ'_{mb} is isotropic consolidation yield stress, which is given by

$$\sigma'_{mb} = \sigma'_{mbi} \exp\left(\frac{1+e_0}{\lambda-\kappa}\nu^p\right)\left[1 + S_I \exp\left(-s_d\left(\frac{P_i^C}{P^C}-1\right)\right)\right] \quad (3)$$

where σ'_{mbi} is initial value of consolidation yield stress σ'_{mb} pre-consolidation pressure, e_0 is the initial void ratio, λ is the compression index, κ is the swelling index, the ν^p is the plastic volumetric strain, S_I is the is the ratio of reduction of initial suction, s_d represents the rate of that change, P_i^C is initial suction and P^C is the current suction value. The governing equations and the elasto-plastic model are implemented in the finite element code to consider partial saturation and seepage flow LIQCA-2D-SF [6],[7].

In the numerical analyis the u-p formulation was adopted. For the discretization of the equations of the motion (or equilibrium of the mixture) FEM (Finite Element Method) was used, while for discretization of the continuity equations of the pore fluids (water and gas) FDM (Finite Difference Method) was used. The time discretization is based on Newmark's β method, with β and γ set at 0.3025 and 0.6, respectively. The time increment in the calculation was set to be small enough to guarantee the accuracy of the results without having large computational time (i.e. 0.01 seconds).

3 TWO-DIMENSIONAL NUMERICAL ANALYSIS

To study the influence of the GWL, an embankment-ground system was adopted, typically with a total ground depth of 15m. Three cases with GWL's located at different depths were adopted as follows:

Case1 ; GWL=0.0m

Case 2 ; GWL=-1.0m

Case 3 ; GWL=-3.0m.

The dynamic input motion used was a 1Hz of frequency sinusoidal wave with increasing amplitude, following an arithmetic progression scheme, with maximum amplitude of 250 gal (Fig.1). In the liquefaction analysis the definition of the initial effective is an important step. The profile adopted was composed of saturated and unsaturated domains, which means that two different approaches have to be considered. In the saturated domain the effective stress was calculated using the conventional Terzaghi's effective stress based on the unit weight. Conversely, in the unsaturated domain, the skeleton stress tensor, σ'_{ij}, as defined in (1) was adopted. The horizontal stresses were estimated from the vertical stresses under the at-rest condition, assuming a coefficient of earth pressure at rest K_0 of 0.5 and a Poisson's ratio ν of 0.33. In the unsaturated domain, the increase of the negative pore water pressure (or matric suction) as the depth decrease, was assumed to follow the relationship given by the soil water characteristic curve (SWCC) (Fig.2). At the transition between saturated-unsaturated regions the vertical mesh was refined, so that the change (herein assumed linear for simplicity) of degree of saturation and effective stress could be adequately considered. The dimensions of embankment-ground system used in the analysis were set to be consistent with of a river levee, as in Fig.3. For the boundary conditions it was adopted a horizontal and vertical fixed condition on the base, equal horizontal displacement condition on the lateral boundaries and impermeable boundary on base, lateral and top boundaries (Fig.3). The parameters concerning the soil, the elasto-plastic analysis and the hydraulic properties are representative of Edosakisa sand and were taken from [4], as shown in Table1.

The results were analysed in terms of top vertical displacement and acceleration reduction, as well as in the Effective Stress Decreasing Ratio (ESDR) minimisation. The ESDR is a quantitative indicator of the occurrence of liquefaction and is given as the ratio between the current effective stress value and the initial mean effective stress, as follows:

$$ESDR = 1 - \left(\frac{\sigma'_m}{\sigma'_{m0}}\right) \quad (4)$$

in which σ'_m is the mean effective stress and σ'_{m0} is the initial mean effective stress, and for the unsaturated soil the skeleton stress is used instead of the effective stress .

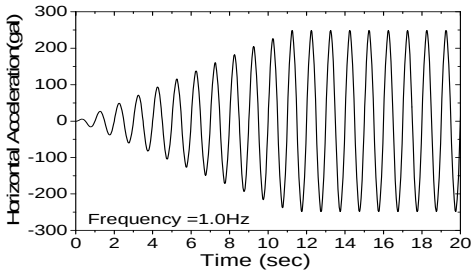

Figure 1: Sinusoidal input motion wave

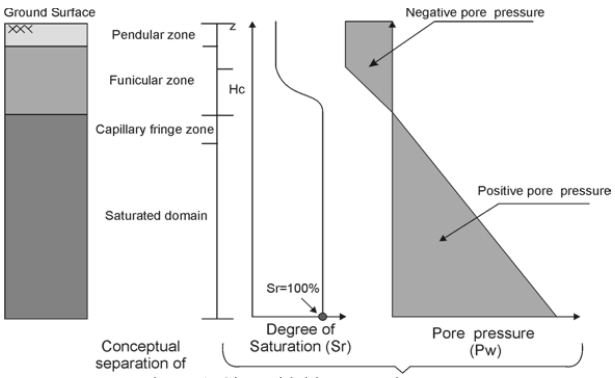

Figure 2: Unsaturated domain hydraulic model.

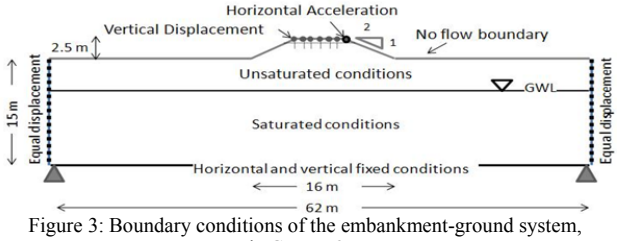

Figure 3: Boundary conditions of the embankment-ground system, ie.GWL=-3m

4 RESULTS AND DISCUSSION

The results show that the GWL located at higher depth, minimizes the overall embankment deformations and contribute to a significant reduction in the vertical displacements observed on the top of the embankment (Fig. 4). In fact, the GWL located at a larger depth yielded smaller vertical displacements on top of the embankment levee. However, the vertical displacements are reduced by a more significant amount for the case with GWL located closer to the surface at -1m depth (i.e. 24% reduction). In the case where GWL was set a deeper level (GWL=-3m) the reduction of the vertical displacements was marginal comparatively to the case with GWL -1m depth (increase of 4%). These results indicate that even small GWL depth changes (i.e. up to -1m depth) are likely to minimise significantly the vertical displacement of the superstructures located on high liquefaction susceptibility areas. In Figs. 5, 6 and 7 are represented the horizontal acceleration time profiles for the top right corner of the embankment levee together with their respective envelopes. In Fig. 7 the envelopes representative of the acceleration profiles for the GWL at different depths are shown together with the acceleration profile for GWL= -3m depth. The decrease in the water level leads to a progressive increase in the peak acceleration, varying from 0.38 m/s^2 for GWL= 0m depth to 0.42m/s^2 for GWL= -3m depth. This tendency is likely to be related with the reduction of the saturated region, that causes a more significant transmission of the dynamic motion to the upper elements located at the level of the embankment. Conversely, after the peak acceleration is reached (i.e. around 2sec) the acceleration values are smaller for the cases where GWL is located at higher depth.

Table 1: Soil and Elasto-plastic parameters

Initial void Ratio: e_0	0.85
Swelling index: κ	0.0018
Compression index: λ	0.006
Permeability: k (m/s)	2.5E-05
Density: ρ (kN/m^3)	19.0
Normalized Shear modulus: $G0/\sigma'_m$	873.28
Quasi Over consolidation ratio: OCR*	1.2
Phase transformation stress ratio: M_m*	0.91
Failure stress ratio: M_f*	1.12
Hardening parameter: B_0*	2200
Hardening parameter: B_1*	30
Dilatancy parameters: D*, n	1.1, 1.5
Elastic modulus of water: K^f (kPa)	2.04E6
Plastic, Elastic ref. strain: $\gamma_{ref}^{P*}\gamma_{ref}^{E*}$	0.005; 0.001
Initial degree of Saturation: S_r	0.6
van Genuchten parameters: α and n'	1.8 , 3.2
Initial suction: P_i^c (kPa)	6.6
Suction parameters: S_l and s_d	0.2 ; 0.2

Fig.8 a) to c) shows the 2D representation of the final values (t=20sec) of ESDR for GWL's located at different depths. ESDR values closer to 1 it suggest that the ratio between the current effective stress (which is decreasing during cyclic loading) and initial effective stress has become very small, which means that liquefaction has occurred.

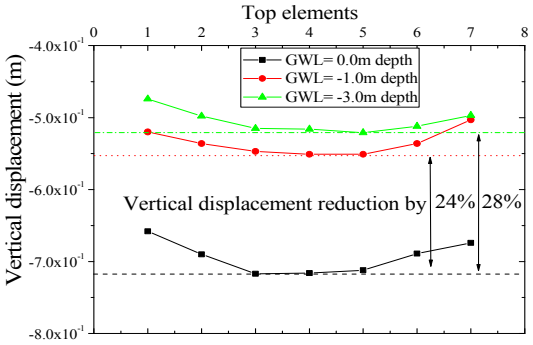

Figure 4: Top Vertical displacement at t=20sec.

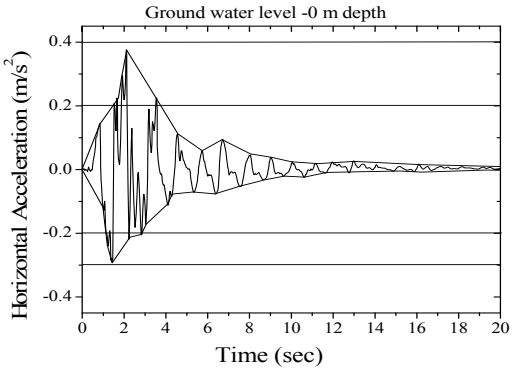

Figure 5: Top horizontal acceleration at the top boundary, t=20sec (GWL= 0m, surface).

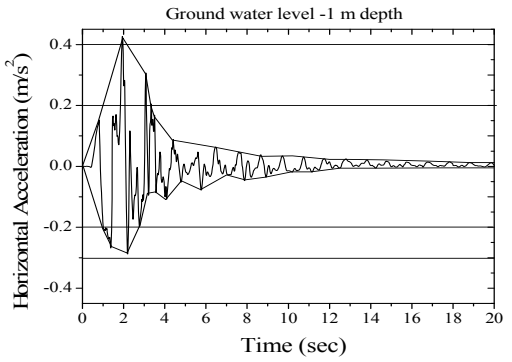

Figure 6: Top horizontal acceleration at the top boundary, t=20sec (GWL= -1m, surface).

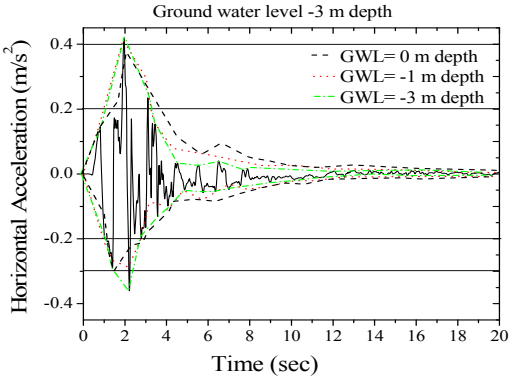

Figure 7: Top horizontal acceleration at the top boundary, t=20sec (GWL= -3m, surface).

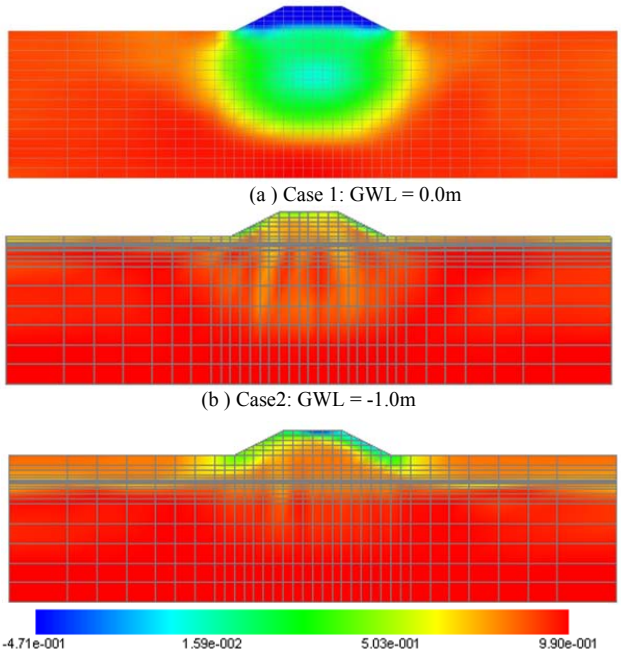

(a) Case 1: GWL = 0.0m

(b) Case2: GWL = -1.0m

(c) Case3: GWL = -3.0m

Figure 8: 2D representation of ESDR values at t=20sec.

Overall, the increase in GWL depth seems to decrease the area that is affected by liquefaction (i.e. ESDR =0.99).

In all the cases (Fig. 8a to 8c) ESDR values obtained for the unsaturated domain were smaller or even negative, particularly on top of the embankment. In this domain there is nearly no increase in pore water pressure and consequently the effective stress does not decrease during cyclic loading. However, negative ESDR values (i.e. ESDR=-0.471) indicate that effective stress is increasing beyond its initial value this is likely to be related with the definition of effective stress in the unsaturated domain; where matric suction (negative by convention) plays an important role in the shear strength of the soil. Below the embankment levee were obtained smaller values of ESDR this tendency is related to the effective confining stresses acting on the ground, which are higher for the portion below the embankment. Note also that the liquefaction condition closer to the toe of the embankment (Fig 8a) that are likely to cause severe lateral deformations to the embankment structure are considerably minimised for the cases where GWL in located at a deeper level.

5 CONCLUSION

An alternative cost-effective method for liquefaction mitigation inducing GWL variation was investigated. The artificially variation of GWL depth causes the soil to be partially saturated and in turn strengthens the soil against liquefaction hazards. In fact, smaller vertical displacements were observed for the cases where GWL was located at higher depth. Furthermore, even a small variation of GWL, i.e. GWL=-1m depth was enough to produce a vertical displacement reduction of 24% compared with a marginal increase of 4% obtained for GWL located at -3m depth. The peak acceleration values were higher for GWL depths located at deeper levels motivated by the transmission of dynamic motion to the upper unsaturated elements (that typically behaved like dry soil). However, the order of this difference was found to be small.

This study shows that artificially GWL variation can be used as an effective method to control the magnitude of the superstructures deformations caused by the occurrence of liquefaction. In this study a 1Hz sinusoidal input wave was adopted for simplicity. Similar results are likely to be obtained for a real earthquake wave, on which frequency and acceleration contents are quite different. Further studies using real earthquake data are necessary to confirm the present findings. Moreover, the successful application of this methodology lies on an adequate GWL numerical study, so that the best cost-benefit ratio (GWL depth vs. vertical displacement reduction) can be found.

6 ACKNOWLEDGMENT

The Authors wish to acknowledge the financial support given by the Japanese Ministry of Education (Monbugakusho). Thanks are also due to Dr. Kato, Mr. Morinaka and Mr. Sanagawa for assisting with the details of some of the numerical work contained in this study.

7 REFERENCES

[1] Okamura, M. Inexpensive liquefaction countermeasure- soil desaturation by air injection. Tsuchi to kiso-JGS , 54-7, 2006, pp 28 – 30 (Japanese)

[2] Yoshimi Y., Tanaka, K., Tokimatsu, K. Liquefaction resistance of a partially saturated soil. Soils and Foundations, 29-3, 1989, pp. 157-162.

[3] Nakazawa, H., Ishihara, K., Tsukamoto, Y. and Kamata, T. Cases studies on the evaluation of liquefaction resistance of imperfectly saturated soil deposits. In Proc. Of Cyclic Behavior of Soil and Liquefaction Phenomena Conference, Triantafyllidis(ed), 2004, pp. 295-304.

[4] Oka, F.,Yashima, A., Taguchi, Y. & Yamashita, S. –Geotechnique, 49-5,1999, pp.661–680.

[5] Oka, F., Kodaka, T., Kimoto, S., Kato, R. & Sunami, S. Key Engineering Materials, 340-341, 2007, pp.1223–1230.

[6] Kato, R.; Oka, F., Kimoto, S.; Kodaka, T. & Sunami,S. Transaction of JSCE, C, vol65-1, 2009, pp.226-240

[7] The LIQCA Research and Development Group – User's Manual for LIQCA2D04, 2005

First International Conference on Geotechnique, Construction Materials and Environment, Mie, Japan, Nov.21-23, 2011, ISBN: 978-4-9905958-0-7 C3051

Development of a New Type Reinforced Soil Wall

Hara, T. Tsuji, S. Yoshida, M. Ito, S. and Sawada, K., Department of civil engineering, Gifu Unicersity

ABSTRACT: Our aim in this study is to develop a new type of reinforced soil walls as substitute for concrete ones. The structure that piles are inserted into reinforced soil wall body has been studied as the new type structure. In this development, a static loading test, a dynamic centrifuge test and an impact loading test were carried out in order to confirm the practicability of the structure to actual diverse sites. In this paper, the details of the static and impact loading tests are introduced and the practicability of the structure is discussed.

Keywords: Reinforced soil, pile foundation, retaining wall, rockfall protection structure

1. INTRODUCTION

The high ductility of soil structures reinforced by geogrid is well known, as is the possibility of building independent soil structures. The independent reinforced soil structure, which is referred to “Geo-wall” in this paper, has been applied to such diverse structures as rockfall protection walls [1], mud and snow avalanche protection walls [2] and the suchlike. Fig. 1 shows an example of the application of Geo-wall to a rockfall protection wall. Since Geo-wall can be built using existing soil at the construction site if it is compactable one, they are being used ever more frequently as one of economic and CO2 reducible structures.

Fig. 1. Application to a rockfall protection wall.

At present, however, the adoption of the spread foundation for Geo-walls makes the design too wide for application to narrow construction sites, such as beside mountainous road. If a narrow Geo-wall as like as RC structure with pile foundation is achieved, Geo-walls could be widely applied. And it can also be applied as substitute for concrete structures and contribute sustainable development.

Therefore, a new type reinforced soil wall that piles are inserted into the Geo-wall body as shown in Fig. 2, which is referred to “Piled Geo-wall” in this paper, has been developed by authors. The application of piles to Geo-wall in order to improve lateral resistance is a completely new approach, since piles tend to be vertical bearing piles and are applied to soil fillings or as reinforcements to soil fillings on soft ground vertical pile [3]. In this novel approach, an assumption is made regarding the interaction between the pile and Geo-wall, as shown in Fig. 3. The high ductility of the Geo-wall was assumed to make it possible to transmit lateral force to the piles despite large relative displacement between the pile and Geo-wall. The validity of this assumption and practicability of Piled Geo-wall to actual diverse structure were confirmed through three experiments, a dynamic centrifuge model test [4]-[6], a static loading test and an impact loading test.

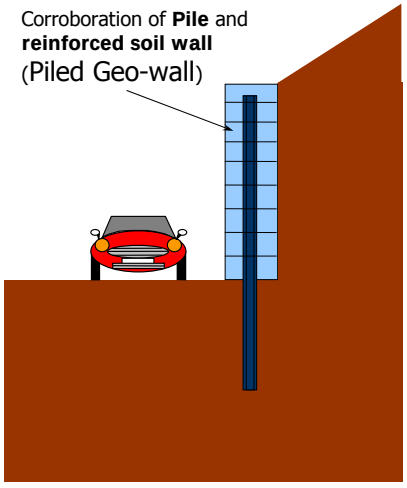

Fig. 2. An image of Piled Geo-wall.

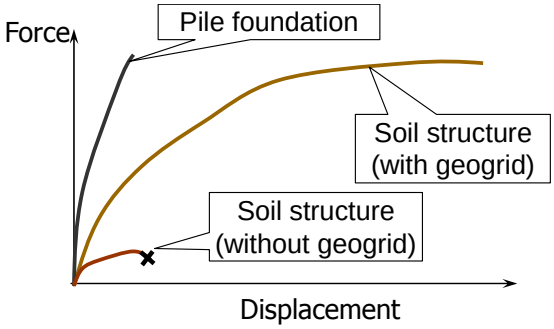

Fig. 3. Interaction between pile and Geo-wall.

In this paper, the details of the static and impact loading tests are introduced and the practicability of the Piled Geo-wall is discussed.

2. STATIC AND IMPACT LOADING TEST

2.1 Geo-walls for Experiments

Three full scale Geo-walls, normal Geo-wall (without pile), Piled Geo-wall-1 (PGW-1) and Piled Geo-wall-2 (PGW-2) were built on an actual field, and, at first, a static loading test was carried out with using the normal Geo-wall and PGW-1 and then an impact loading test was carried out with using all Geo-walls as shown in Fig. 4. Respective structural conditions, measurements and loading conditions are illustrated in each section of experiment. Fig. 5 shows the appearance of the Geo-walls.

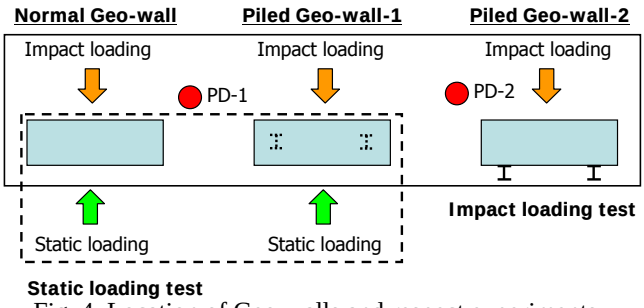

Fig. 4. Location of Geo-walls and respect experiments.

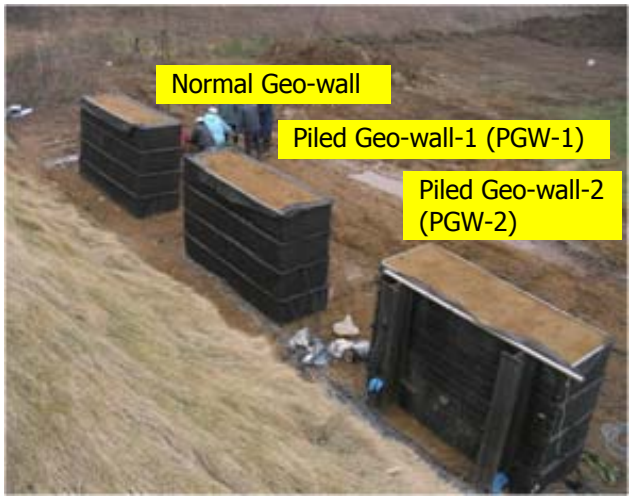

Fig. 5. Appearance of Geo-walls.

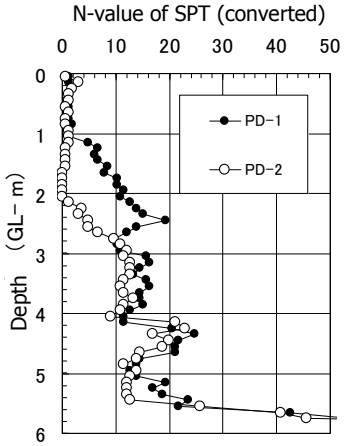

Fig. 6. Results of dynamic penetration tests.

2.2 Ground Condition

The foundation ground consists of three types of sandy silt, soft buried one, medium stiffness and stiffness ones. Fig. 6 shows the results of dynamic penetration test converted to N value of standard penetration test (SPT). The location of the borings, PD-1 and 2, is shown in Fig. 4. The thickness of the soft buried top soil is varied from the place of normal Geo-wall (PD-1) to Piled Geo-walls (PD-2).

2.3 Static Loading Test

A static loading test was carried out in order to confirm the practicability of Piled Geo-wall to earth retaining wall. In this test, two full scale Geo-walls, PGW-1 and normal Geo-wall (without pile), were adopted. Fig. 7 shows the structural summary of the test. Static horizontal load are given by two jacks set at 1.0m in height. And the horizontal load is carried as distributed pressure through an EPS of 0.5m in thickness, a steel plate of 0.12m in thickness and H steel (H200 x 200 x 8 x 12).

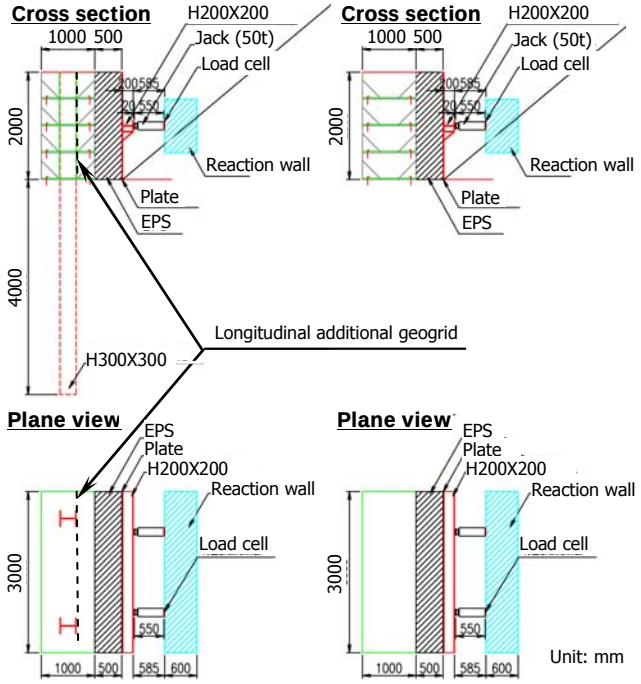

(a) PGW-1 (b) Normal Geo-wall

Fig. 7. Structural summary of static loading test.

The procedure of Geo-walls' building is as follows;

Pile installing (Piled Geo-wall only): H steel piles (H-300x300x10x15) of 6.0m in length are installed in 4.0m into the ground.

Setting of steel face member and installing of geogrid at each layer: steel face members were set on the both side of Geo-wall and a geogrid was installed at one layer. In the construction of Piled Geo-wall, a geogrid with holes located in the piles was installed through the piles, as shown in Fig.8. Fig. 9 shows the tensile stiffness of the geogrid.

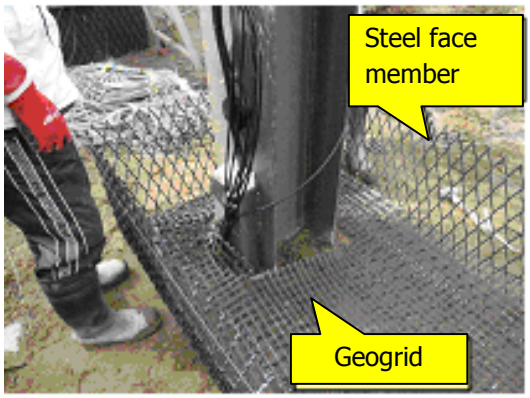

Fug. 8. Installing of steel face member and geogrid.

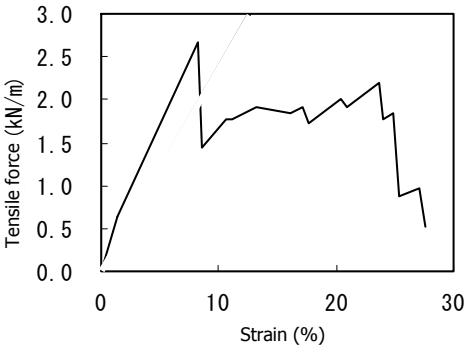

Fig. 9. Tensile stiffness of geogrid.

Installing of longitudinal additional geogrid at each layer (Piled Geo-wall only): the additional geogrid was installed on the loading side of piles, as shown in Fig. 10, in order to transmit the load to the piles from the Geo-wall body smoothly.

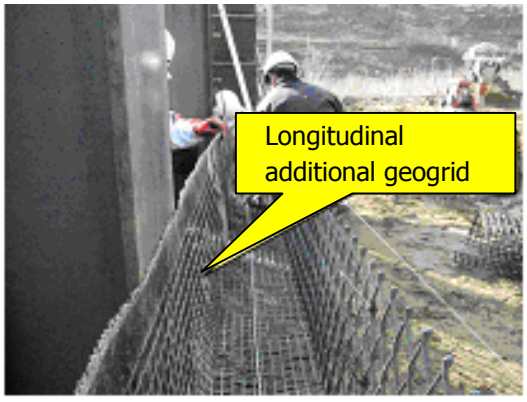

Fig. 10. Installing of longitudinal additional geogrid.

The executions of each layer, 0.5m in thickness, were repeated until that the Geo-walls, 2.0m in height, were completed.

The measurements of strains of geogrids, additional longitudinal geogrids and a pile, earth pressure of the Geo-walls at the loading side, deformation of the Geo-walls and jack pressures were planned. Figure 11 and 12 show the summary of measurements.

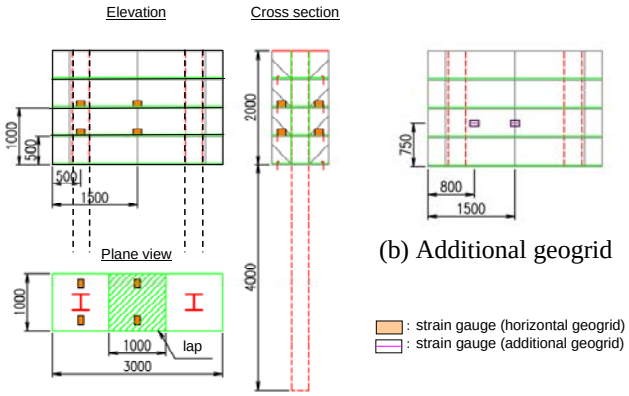

(b) Additional geogrid

(a) Horizontal installed geogrid

Fig. 11. Measurements of strain in geogrids.

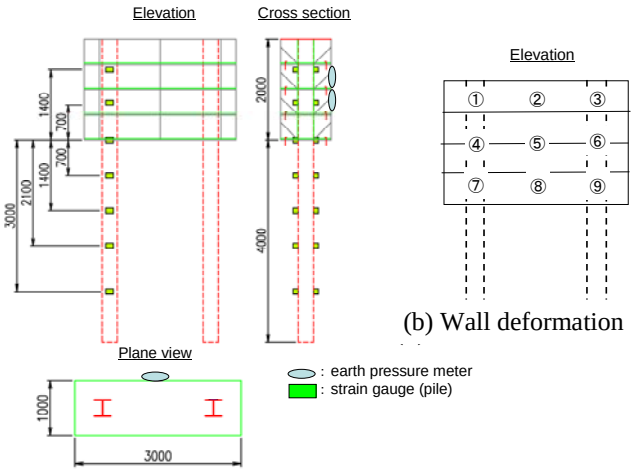

(b) Wall deformation

(a) Pile strain and earth pressure

Fig. 12. Measurements of strain of pile, earth pressure and deformation of Geo-wall.

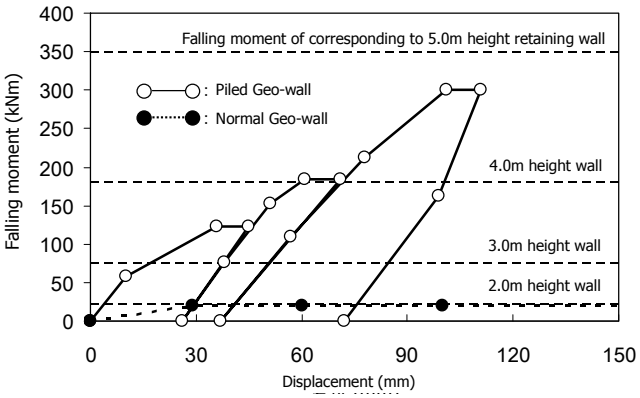

Fig. 13. Response of Geo-walls.

Fig. 13 shows the relationship between falling moment and displacement of center top of the Geo-walls (No.2 of Fig. 12(b)). Where, in order to compare with the active earth pressures loaded to retaining walls with different height, vertical axis is presented by falling moment. According to the results, high resistance characteristics of the Piled Geo-wall

can be confirmed from the view point of that the proof strength of Piled Geo-wall is still increasing even if corresponding earth pressure of retaining wall of 4.0m in height is loaded. Against the Piled Geo-wall, because of soft bearing foundation shown in Figure 6, the normal Geo-wall indicated the tendency of falling by corresponding earth pressure of retaining wall of 2.0m in height. Namely, in case of adoption of normal Geo-wall in this site, too wide Geo-wall has to be designed.

Fig. 14 shows the maximum response distribution of pile. According to the results, it can be confirmed that the horizontal load is transmitted to the pile and the pile contributes for improving the lateral resistance of the narrow Geo-wall.

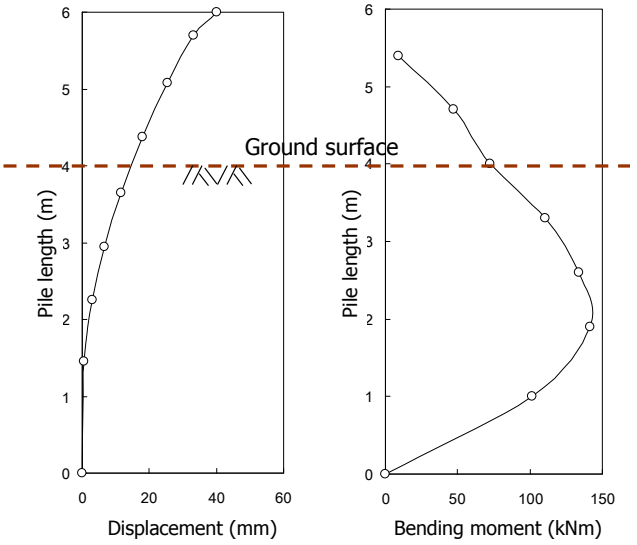

(a) Displacement (b) Bending moment

Fig. 14. Maximum response distribution of pile.

Fig. 15 shows the relationship between horizontal load and strain occurring in longitudinal additional geogrid. According to the results, the strain occurring in the geogrid of the pile side is larger than the center one and the strain depends on the intensity of the horizontal load, thus the geogrid is considered to sufficiently function for transmitting of lateral force to piles from Geo-wall body.

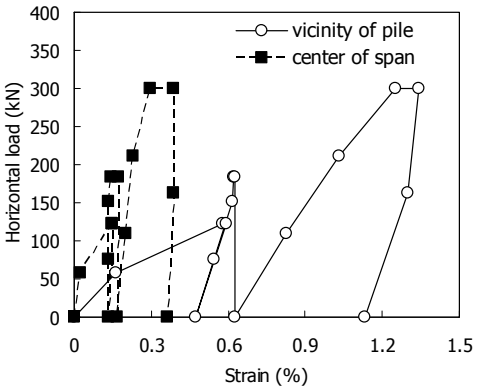

Fig. 15. Strain occurring in additional geogrid.

Fig. 16 shows the responses of the pile and the Geo-wall body at the point of pile top (No.1 of Figure 12(b)). According to the results, large relative displacement of the pile and Geo-wall is occurred though, the lateral force is transmitted to the pile from the Geo-wall and the lateral resistance of the Geo-wall was improved as abovementioned. Namely, the validity of the assumption established previously, “Geo-wall with high ductility can transmit lateral force to piles despite large relative displacement between the pile and Geo-wall as shown Fig. 3”, could be confirmed.

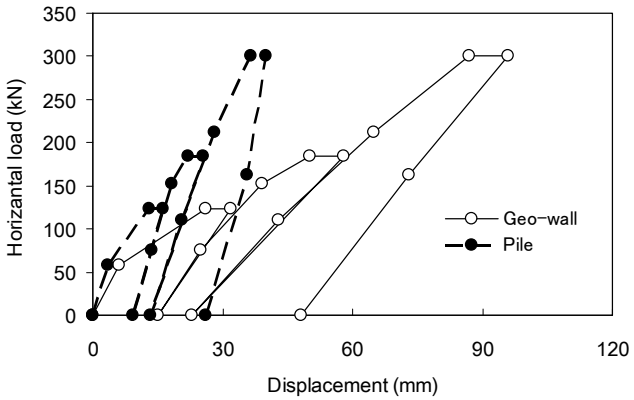

Fig. 16. Response of pile and Geo-wall body.

2.4 Impact Loading Test

An impact loading test was carried out in order to confirm the practicability of Piled Geo-wall to rockfall protection walls. In this test, three actual scale models, the two models of the normal Geo-wall and PGW-1, which are adopted in the static loading test, and a new one (PGW-2) were adopted, as shown in Fig. 4. The piles of PGW-2 are installed at outside of Geo-wall as shown in Fig. 17, are adopted.

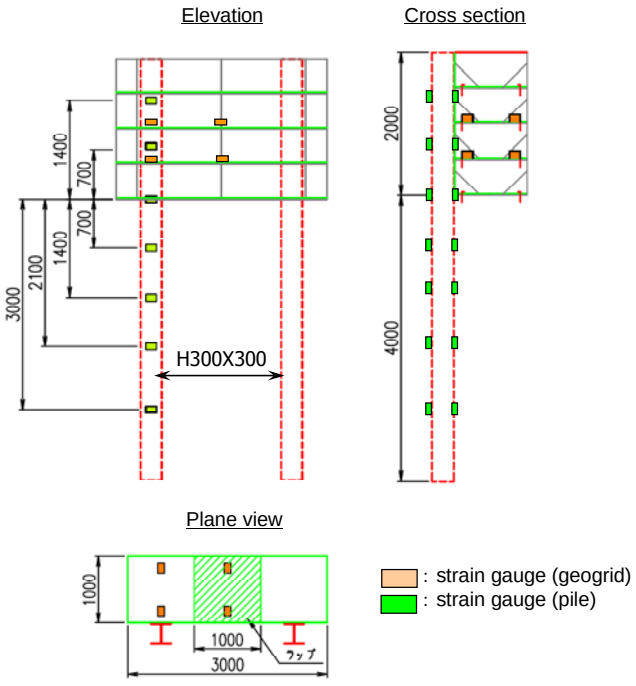

Fig. 17. Structural condition and measurements of PGW-2.

PGW-2 was adopted to confirm the best position of pile installing in case of impact loading, because there considered a possibility that keeping wide energy absorption extent is better than receive the rockfall energy at the center of Geo-wall body as PGW-1. In addition, the loading direction of static and loading tests are different, thus longitudinal additional geogrid of PGW-1 was installed on both sides of the Pile previously. In PGW-2, the additional geogrid was not installed. In this impact test, the impact of 100kJ was loaded to respective Geo-walls as shown in Fig. 18.

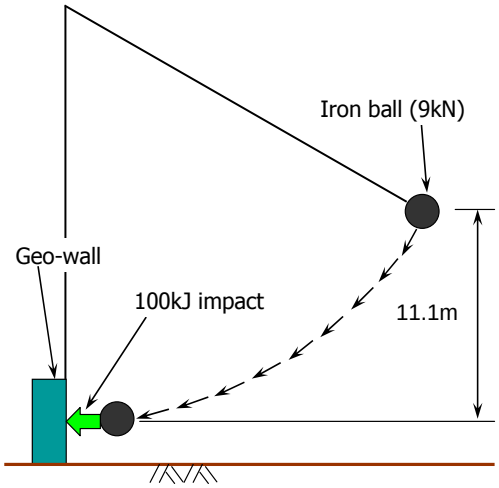

Fig. 18. Impact loading test.

Fig. 19 to 21 show the respective test results.
According to the results, against the collapse of normal Geo-wall, both Piled Geo-walls could receive the impact energy. Namely, the effectiveness of application of piles to improve lateral resistance of Geo-wall could be confirmed.
Note, however, that the deformation of the back side of the Geo-wall (protecting side, road side for instance), one of PGW-2 (piled installed at outside of the Geo-wall) is smaller than one of PGW-1 (piles installed at center of the Geo-wall). Since this result, the possibility that the best position of pile installing is outside of the Geo-wall in impact loading case can be considered. Meanwhile, from Fig. 22 showing responses of piles of the PGW-1 and 2, it is also considered that the resistance of the piles of PGW-1 seems to be smaller than ones of PGW-2. With respect to the result, following reasons can be considered.
- There might be a void in front of resistance surface of the piles of PGW-1 before the impact loading test because of the static loading test implementation.
- In the foundation ground that the piles of PGW-2 were installed, the soft buried soil is comparatively thin, because the piles of PGW-2 were installed at the position closed to vicinity hill of 0.65m.
The best position of pile installing in case of impact loading has to be studied again with considering abovementioned phenomenon in the near future.


Fig. 19. Normal Geo-wall.

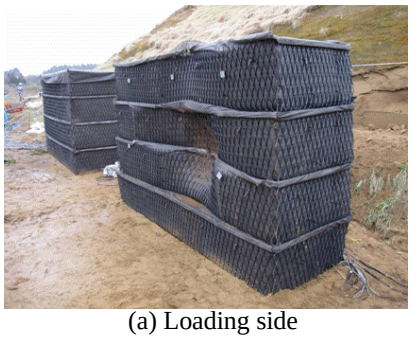
(a) Loading side


(b) Back side (protecting side)
Fig. 20. Piled Geo-wall-1 (PGW-1)


(a) Loading side


(b) Back side (protecting side)
Fig. 21. Piled Geo-wall-2 (PGW-2)

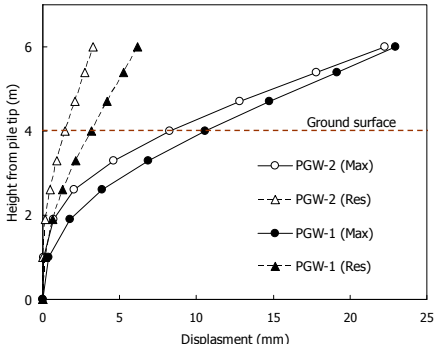

(a) Displacement

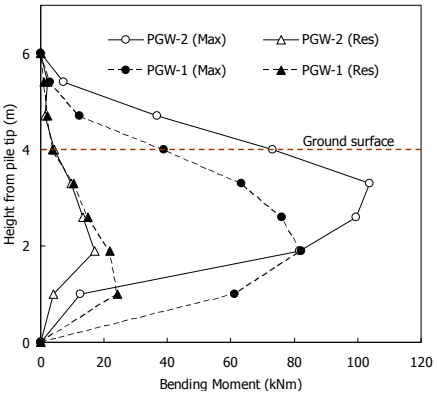

(b) Bending moment

Fig. 22. Response of piles of PGW-1 and 2.

Fig. 23 shows transition of strain occurring in the longitudinal additional geogrid and the pile of PGW-1. According to the results, from the view points of the strain occurring in the geogrid and the timing of occurrence of the strain between the geogrid and the pile, effect of the geogrid to transmit the lateral forces to the piles from Geo-wall could also be confirmed in the impact loading test.

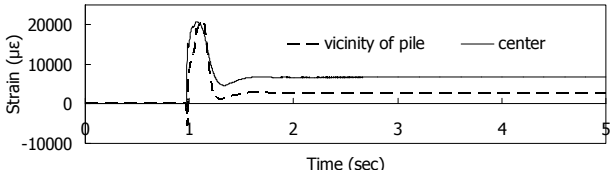

(a) Additional geogrid

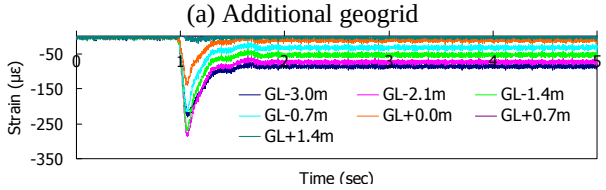

(b) Pile

Fig. 23. Strain of additional geogrid and pile of PGW-1.

3. CONCLUSION AND DISCUSSION ON PRACTICABILITY OF PILED GEO-WALL

Application of piles to Geo-wall: The effectiveness of application of piles to Geo-wall in order to improve lateral resistance of Geo-wall was confirmed from all the tests carried out in this study.

Unification of piles and Geo-wall body: Geo-wall with high ductility can transmit lateral forces to piles despite large relative displacement between the pile and Geo-wall. And adoption of longitudinal additional geogrid is effectiveness to achieve the unification of piles and Geo-wall body. Note, however, that the effect of the relative displacement to the internal quality of the Geo-wall body has to be studied.

Application to retaining walls: High resistance characteristics against static load and dynamic earth pressure could be confirmed from the static loading test as well as the previous carried out dynamic centrifuge model test [4]-[6]. Therefore, application of Piled Geo-wall to retaining walls is sufficiently possible for all ones depending on the tolerable deformation of the Piled Geo-wall and the embankment sustained by Piled Geo-wall.

Application to rockfall protection walls: High performance of Piled Geo-wall to receive rockfall could be confirmed from the impact loading test. Hence, application of Piled Geo-wall to rockfall protection walls would be possible if it is similar target rockfall with the experiment carried out in this study. Further experiments to determine the best position of the pile installing and to study the design for appropriate size of Piled Geo-wall depending on the intensity of rockfall energy are necessary before the widely application.

Design code for the application: Studies on the design method based on numerical simulations of the test results are conducting by authors. Although needed further experiments and studies to solve several issues are remained as abovementioned, a valuable design code for widely use of Piled Geo-wall would be published in the near future.

Expectation of Piled Geo-wall to sustainable development: Piled Geo-wall has possibility to be used as alternative structure of concrete ones with similar size. Therefore, if the development of Piled Geo-wall is achieved, it can be expected that the Piled Geo-wall contribute to sustainable development from the viewpoint of reducible structure of CO2.

4. REFFERENCES

[1] Yoshida, M., Tatsuta, N., Nishida, Y., Inoue, S., Yashima, A., Sawada, K. & Moriguchi, S., "Full-scale field test of reinforced embankment adjacent to steep-slope," Geosynthetics Engineering Journal, Vol.20, 2005, pp. 295-300.

[2] Itou, S., Yokota, Y., Kubo, T. & Arai, K., "Field loading test of the protection embankment retaining wall reinforced with geosynthetics," Geosynthetics Engineering Journal, Vol.15, 2000, pp. 340-349.

[3] Hara, T. & Tsuji, S., "A reinforced soil structure with pile foundation," Geosynthetics Engineering Journal, Vol.23, 2008, pp. 209-214.

[4] Hara, T., Tsuji, S., Yashima, A., Sawada, K., Tatta, N., "Dynamic interaction between pile and reinforcement soil structure – Piled Geo-wall –," in Proc. of Int. Conf. on IS-KYOTO, 2009, pp. 457-463.

[5] Hara, T., Tsuji, S., Yashima, A., Tatta, N., "Dynamic centrifuge model test on Piled Geo-wall," Geosynthetics Engineering Journal, Vol.24, 2009, pp. 257-262.

[6] Hara, T., Tsuji, S., Yashima, A., Sawada, K., Tatta, N. & Otake, Y., "Independent reinforced soil structure with pile foundation," J. of SOILS AND FOUNDATIOS, Vol.50, No.5, 2010, pp. 565-571.